

ANALYSIS OF FLUID FLOW AROUND A ROTATING CIRCULAR
CYLINDER USING RBVMS AND IGA

C.C.L. FEIJ

to obtain the degree of
Master of Science in Ship Hydromechanics
at Delft University of Technology,
to be defended in public on December 17, 2019 at 15:00

Thesis committee	Prof. dr. ir. J. Westerweel	TU Delft	
	Dr. ir. I. Akkerman	TU Delft	Supervisor
	Ir. M.F.P. ten Eikelder	TU Delft	Co-supervisor

ABSTRACT

The case of the flow around a rotating circular cylinder is very complex. This thesis investigates the properties of a fluid flow for Reynolds numbers ranging from 50 to 400. Numerical simulations are performed using a combination of isogeometric analysis and the residual-based variational multiscale method, providing high accuracy. The results show how the lift and the drag generated by the cylinder are related to the spin rate and the Reynolds number. When comparing the lift and drag values to the required amount of torque which is needed to spin the cylinder, it is shown that at medium spin rates, a very high aerodynamic efficiency is obtained at a reasonable amount of torque. 3D simulations are performed and show at high spin rates strong vorticity and a wake that is dominated by vortex shedding. These results differ strongly from the 2D simulations, which leads to the question whether 2D simulations are still representative for real real at high spin rates, despite the low Reynolds number.

CONTENTS

1	INTRODUCTION	1
1.1	History of the Flettner rotor	2
1.2	Motivation for this thesis	3
1.3	Research questions	3
1.4	Scope of this thesis	4
1.5	Reading guide	4
2	PHYSICS OF THE FLOW AROUND A CYLINDER	5
2.1	The stationary cylinder	5
2.2	The rotating cylinder	5
2.3	Summary of previous work	7
2.3.1	Prandtl's limit	7
2.3.2	Simulations at high Reynolds numbers	7
2.3.3	Flow properties for low Reynolds numbers	8
2.3.4	3D simulations at high spin rate	10
3	NUMERICAL METHOD	11
3.1	Overview of the numerical method	11
3.2	NURBS	12
3.2.1	Introduction	12
3.2.2	From knotvectors to B-splines	13
3.2.3	From B-splines to NURBS	14
3.3	Residual-Based Variational Multiscale method	16
3.3.1	Introduction	16
3.3.2	Variational form of the Navier-Stokes equations	16
3.3.3	Residual-based multiscale method	18
3.4	Time integration method	21
3.5	Software overview and computational costs	23
3.5.1	Force and torque extraction	23
4	MESH AND FLOW PARAMETERS	25
4.1	Mesh Description	25
4.1.1	Mesh domain	25
4.1.2	Boundary Conditions	26
4.1.3	Initial Conditions	28
4.2	Mesh Optimisation	28
4.2.1	Workflow for Validation	28
4.2.2	Parameter Sensitivity	28
4.2.3	Sensitivity with respect to the timestep	29
4.3	Mesh Convergence Study	30
4.3.1	Validation of the set-up	34
4.4	Three-dimensional mesh	37
5	RESULTS AND ANALYSIS	39
5.1	2D results for Reynolds number 200	39
5.2	2D results for varying Reynolds number	43
5.2.1	Reynolds number 50	43
5.2.2	Reynolds numbers 100 to 400, $\alpha \leq 2.0$	43

5.2.3	Second region of vortex shedding	45
5.2.4	Reynolds-dependency of lift and drag	46
5.3	3D results	48
5.3.1	High spin rates	48
5.3.2	Low spin rates	50
5.3.3	Comparison between 2D and 3D	51
5.3.4	Aerodynamic efficiency and torque	54
6	CONCLUSIONS AND RECOMMANDATIONS	57
6.1	Second region of instability	57
6.2	Validity of 2D simulations	57
6.3	Negative drag	58
6.4	Efficiency of the system	58
6.5	Recommendations	59
6.5.1	Mesh optimisation	59
6.5.2	Scalability	59
	Appendices	61
A	FINITE ELEMENT METHOD	63
A.1	Variational form	63
B	INTEGRATION BY PARTS APPLIED TO TERMS OF THE NAVIER-STOKES EQUATIONS	65
B.1	Integration by parts and Gauss's divergence theorem	65
B.2	Applied to the diffusion term	66
B.3	Applied to the pressure term	66
C	MESH OPTIMISATION	69
D	LIFT AND DRAG PLOTS	71
D.1	Reynolds number 50, 2D	72
D.2	Reynolds number 100, 2D	73
D.3	Reynolds number 200, 2D	74
D.4	Reynolds number 200, 3D	75
D.5	Reynolds number 300, 2D	77
D.6	Reynolds number 400, 2D	78
D.7	Mean lift and drag, 2D	79
D.8	Mean lift and drag, 2D and 3D	80
D.9	Aerodynamic efficiency and torque	81
E	ADDITIONAL VISUALISATIONS IN 2D	83
F	ADDITIONAL VISUALISATIONS IN 3D	85
F.1	Reynolds number 200, spin rates up to 4.0	86
F.2	Reynolds number 200, spin rates above 4.0	88
	BIBLIOGRAPHY	89

LIST OF FIGURES

Figure 1	The flow around a clockwise rotating cylinder at spin rate $\alpha = 3.0$ for Reynolds number 200 shows the acceleration of the fluid on the suction side (upper part) and a reduction of the velocity at the pressure side (lower part). Alongside the drag force, D , a lift force, L , is generated.	1
Figure 2	A ship using Flettner rotors by means of propulsion.	2
Figure 3	Commercial "wind-hybrid" cargo ship E-Ship 1.	3
Figure 4	Flow regimes for a stationary cylinder for varying Reynolds numbers, retrieved from Fredsoe and Sumer [11].	6
Figure 5	Lift coefficients plotted against drag coefficients for simulations at Reynolds number 200 for several spin rates, retrieved from Mittal and Kumar [17].	9
Figure 6	Lift coefficients for 3D simulations at Reynolds number 200 for spin rate $\alpha = 5.0$, retrieved from Mittal [16].	10
Figure 7	An example of the quadratic basis functions for a knotvector consisting of seven knots, with multiplicity of 2 at the fifth knot. Retrieved from [6].	13
Figure 8	An arbitrary example of a geometric B-spline curve corresponding to the basis functions from figure 7. The red squares represent the control points. Retrieved from [6].	14
Figure 9	A 2D circle is constructed from a projection from \mathbb{R}^3 onto \mathbb{R}^2 . Retrieved from Cottrell, Hughes, and Bazilevs [6].	15
Figure 10	An example is given of the dampening of the high frequencies. In the top graph, the solution is given without filtering, in the bottom graph, the highest frequency is filtered out.	22
Figure 11	Visualisation of the 2D domain with the five patches	25
Figure 12	Visualisation of the 3D domain	26
Figure 13	Numbering of the boundaries in 2D	27
Figure 14	Visual representation of u for CFL numbers of respectively 0.37, 1.48, 3.69, 7.39 and 14.77 (from top to bottom)	31
Figure 15	C_L (upper curves) and C_D (lower curves) for several CFL numbers.	31

Figure 16	C_L and C_D for meshes M1, M2, M3, M5, M8	32
Figure 17	Visual representation of u for respectively M3, M4, M5 and M6 (from top to bottom)	33
Figure 18	Visualisations of the flow at $Re = 200$ and $\alpha = 1.0$. Above: real flow from Coutanceau and Ménard [7]. Below: present result with velocity vectors.	35
Figure 19	Two-dimensional mesh. An enlargement can be found in appendix C.	38
Figure 20	Close-up of the area around the cylinder showing the extra refinement to model the rotary boundary layer correctly. The inner part of this boundary layer contains ten elements.	38
Figure 21	Lift coefficient for $Re = 200$ for the 2D simulation for various spin rates.	39
Figure 22	Drag coefficient for $Re = 200$ for the 2D simulation for various spin rates.	40
Figure 23	Velocity magnitude for Reynolds number 200 at various spin rates, from top to bottom respectively $\alpha = 1.0$, $\alpha = 3.0$, $\alpha = 4.5$ and $\alpha = 5.0$. Note that the colour scales do not match between the figures and vary from zero (purple) to the maximum velocity (red) in each plot.	42
Figure 24	Lift coefficient for $Re = 50$ for the 2D simulation for various spin rates.	43
Figure 25	Lift coefficient for $Re = 100$ for the 2D simulation for various spin rates.	44
Figure 26	Lift coefficient for $Re = 300$ for the 2D simulation for various spin rates.	45
Figure 27	Lift coefficient for $Re = 400$ for the 2D simulation for various spin rates.	46
Figure 28	Mean lift coefficient for several Reynolds numbers plotted against the spin rate.	47
Figure 29	Mean drag coefficient for several Reynolds numbers plotted against the spin rate.	47
Figure 30	Visuals of the three-dimensional flow for $Re = 200$ and $\alpha = 4.50$ at $t = 60.0s$. The colours represent the magnitude of the local velocity vector.	49
Figure 31	Visuals of the three-dimensional flow for $Re = 200$ and $\alpha = 5.00$ at $t = 60.0s$. The colours represent the magnitude of the local velocity vector.	49
Figure 32	Visuals of the three-dimensional flow for $Re = 200$ at spin rates $\alpha = 1.0$ and $\alpha = 3.0$. The colours represent the magnitude of the local velocity vector.	50
Figure 33	Comparison of the lift and drag values for several spin rates at Reynolds number 200 for the 2D and the 3D simulations.	51

Figure 34	Development of the drag coefficient at Reynolds number 200 for varying spin rates in 2D and 3D.	52
Figure 35	Drag coefficient plotted over time for low spin rates ($\alpha \leq 3.0$).	52
Figure 36	Drag coefficient plotted over time for high spin rates ($\alpha > 3.0$).	53
Figure 37	Mean aerodynamic efficiency for several Reynolds numbers plotted against the spin rate.	55
Figure 38	Mean torque coefficient plotted against the spin rate for Reynolds number 200.	55
Figure 39	Lift and drag coefficients are plotted against the time for several meshes with varying domain widths.	69
Figure 40	Lift and drag coefficients are plotted against the time for several meshes with varying wake lengths.	69
Figure 41	Two-dimensional mesh.	70
Figure 42	Lift coefficient for $Re = 50$ for the 2D simulation for various spin rates.	72
Figure 43	Drag coefficient for $Re = 50$ for the 2D simulation for various spin rates.	72
Figure 44	Lift coefficient for $Re = 100$ for the 2D simulation for various spin rates.	73
Figure 45	Drag coefficient for $Re = 100$ for the 2D simulation for various spin rates.	73
Figure 46	Lift coefficient for $Re = 200$ for the 2D simulation for various spin rates.	74
Figure 47	Drag coefficient for $Re = 200$ for the 2D simulation for various spin rates.	74
Figure 48	Lift coefficient for $Re = 200$ for the 2D and 3D simulation for various spin rates.	75
Figure 49	Drag coefficient for $Re = 200$ for the 2D and 3D simulation for low spin rates.	75
Figure 50	Drag coefficient for $Re = 200$ for the 2D and 3D simulation for high spin rates.	76
Figure 51	Lift coefficient for $Re = 300$ for the 2D simulation for various spin rates.	77
Figure 52	Drag coefficient for $Re = 300$ for the 2D simulation for various spin rates.	77
Figure 53	Lift coefficient for $Re = 400$ for the 2D simulation for various spin rates.	78
Figure 54	Drag coefficient for $Re = 400$ for the 2D simulation for various spin rates.	78
Figure 55	Mean lift coefficient for several Reynolds numbers plotted against the spin rate.	79
Figure 56	Mean Drag coefficient for several Reynolds numbers plotted against the spin rate.	79
Figure 57	Mean lift coefficient for several Reynolds numbers plotted against the spin rate.	80

Figure 58	Mean Drag coefficient for several Reynolds numbers plotted against the spin rate.	80
Figure 59	Aerodynamic efficiency for Reynolds number 200 plotted against the spin rate.	81
Figure 60	Torque coefficient for Reynolds number 200 plotted against the spin rate.	81
Figure 61	Time evolution at $\alpha = 1.0$ at respectively $t = 100.0s$, $t = 101.5s$ and $t = 103.0s$ from top to bottom.	83
Figure 62	Time evolution at $\alpha = 4.5$ at respectively $t = 140.6s$, $t = 144.1s$ and $t = 149.1s$ from top to bottom.	84
Figure 63	Visualisation of the flow at $\alpha = 1.0$	86
Figure 64	Visualisation of the flow at $\alpha = 2.0$	86
Figure 65	Visualisation of the flow at $\alpha = 3.0$	87
Figure 66	Visualisation of the flow at $\alpha = 4.0$	87
Figure 67	Time evolution at $\alpha = 4.5$ at respectively $t = 50.0s$, $t = 55.0s$ and $t = 60.0s$ from top to bottom.	88

LIST OF TABLES

Table 1	Strouhal number and lift and drag characteristics for several domain widths. An additional plot can be found in appendix C.	29
Table 2	Relative differences between the values compared to the domain with width 50D.	29
Table 3	Strouhal number and lift and drag characteristics for several domain lengths. An additional plot can be found in appendix C.	30
Table 4	Table of the meshes sizes used for the mesh convergence study	32
Table 5	Overview of several parameters: Strouhal number, amplitude of lift and the mean drag. . . .	34
Table 6	Comparison between present results with the results from Mittal and Kumar [17] at Reynolds number 200 for various spin rates.	36

ACRONYMS

CAD	Computer Aided Design
CAE	Computer Aided Engineering
CFD	Computational Fluid Dynamics
CFL	Courant–Friedrichs–Lewy
CPU	Central Processing Unit
DNS	Direct Numerical Simulation
FEM	Finite Element Method
GSLCL	General Semi-Linear Conservation Law
IGA	Isogeometric Analysis
LES	Large Eddy Simulation
NURBS	Non-Uniform Rational B-Splines
RBVMS	Residual-Based Variational Multiscale Method
VMS	Variational Multiscale Method

LIST OF SYMBOLS

\underline{B}_i	Collection of control points
$\underline{C}(\xi)$	B-spline curve
C_D	Drag coefficient
C_L	Lift coefficient
D	Diameter
D	Drag force
d	Constant for a basis function
\underline{F}	Force vector $(F_x, F_y, F_z)^T$ acting on the cylinder
f	Arbitrary function
\underline{f}	Force vector
g	Arbitrary function
L	Lift force
L/D	Aerodynamic efficiency
N	Basis function
\underline{n}	Normal vector
p	Pressure
q	Weighting function for the continuity equation
Re	Reynolds number
r	Radius
S	Frontal surface area
St	Strouhal number
t	Time
U	Trial solution for the velocity vector and pressure
u	Velocity in x-direction
u_t	Tangential velocity at the cylinder surface
u_∞	Free stream velocity
\underline{u}	Velocity vector $(u, v, w)^T$
v	Velocity in y-direction
\mathcal{V}	Vector space
W	Weighting function for the Navier-Stokes equations
\underline{w}	Weighting function for the momentum equation
w	Velocity in z-direction

α	Spin rate
Γ	Edge or boundary
Δt	Timestep
ν	Kinematic viscosity
Ξ	Knotvector
ξ	Knot of a knotvector
π	Mathematical constant
ρ	Density of the fluid
ρ_∞	Input parameter for Generalized- α method
Φ	Arbitrary solution
Ω	Spatial fluid domain
∇	Gradient
$\nabla \cdot$	Divergence
Δ	Laplace operator

INTRODUCTION

The flow around a circular cylinder is a fundamental problem in Computational Fluid Dynamics. Much is known about the flow characteristics under many different circumstances. However, when the cylinder starts rotating, new challenges arise. The flow around a cylinder is dominated by the Reynolds number, but with adding a rotation to the cylinder, a new parameter has a major influence on the flow characteristics. This parameter is the spin rate, α , defined as the ratio between the tangential velocity at the surface of the cylinder to the free stream velocity:

$$\alpha = \frac{u_t}{u_\infty}. \quad (1)$$

As the spin rate increases, the streamlines are diverted. This results in an asymmetrical situation, where a lift is generated by the cylinder, the so-called "Magnus effect", shown in figure 1.

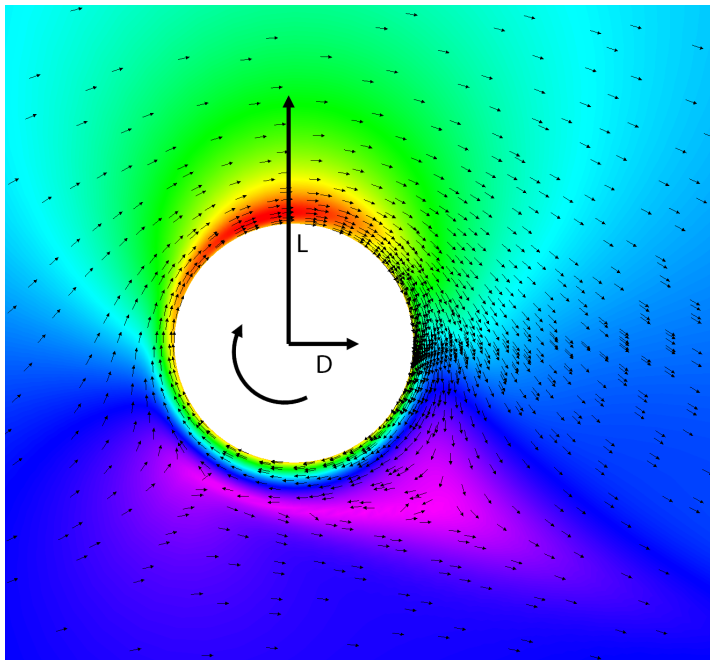


Figure 1: The flow around a clockwise rotating cylinder at spin rate $\alpha = 3.0$ for Reynolds number 200 shows the acceleration of the fluid on the suction side (upper part) and a reduction of the velocity at the pressure side (lower part). Alongside the drag force, D , a lift force, L , is generated.

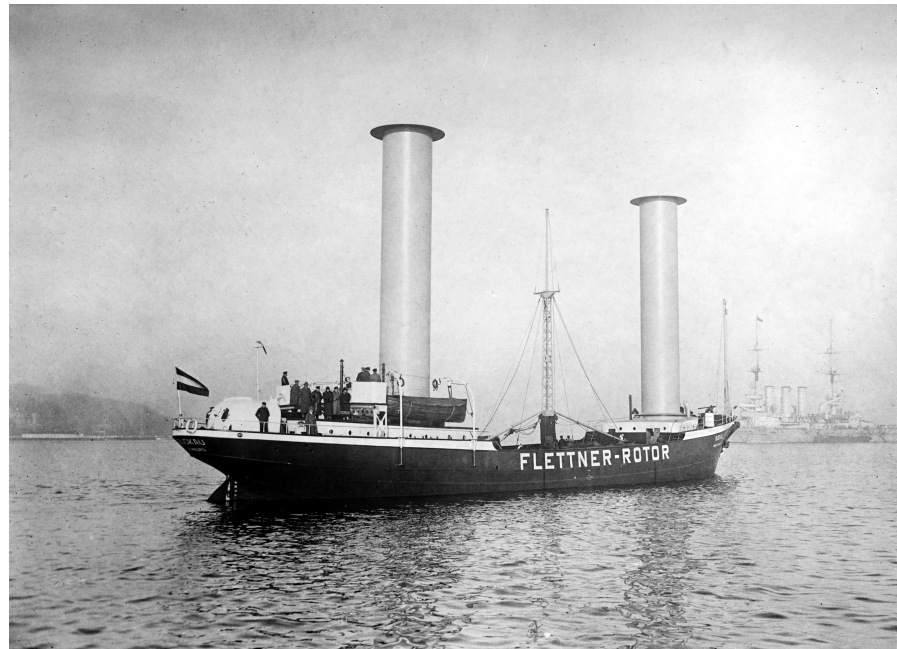


Figure 2: A ship using Flettner rotors by means of propulsion.

1.1 HISTORY OF THE FLETTNER ROTOR

From an engineering standpoint, an obvious question that arises is whether there are applications to rotating cylinders within the maritime industry. One answer was already given in 1925 by Anton Flettner. He designed a ship which uses rotating cylinders as a method of wind-assisted propulsion, illustrated by figure 2. An engine was used to rotate the giant cylinders when wind was blowing abeam. This rotating cylinder became then known as the "Flettner rotor".

Apart from this gimmicky feature back in 1925, it took a long time for the Flettner rotor to gain popularity again. Two major drawbacks are its size and its dependency on the wind, in the era of diesel engines and gas turbines. In the last decade, some interest in this topic has returned. The E-Ship 1, depicted in figure 3, from Enercon GmbH made its maiden voyage in 2010. This ship has four Flettner rotors used to assist the ship's propulsion which would provide 40% of the total delivered power under favourable conditions [9]. Pearson [21] notes the potential of fuel savings of wind-assisted propulsion. Furthermore, the reduction of carbon emission yields ecological advantages alongside the financial aspect.

But what is the main advantage of a Flettner rotor compared to a regular airfoil? The answer can be found in the amount of lift that can be generated. When airfoils are considered, typical maximum values for the lift coefficient, C_L , are in the range between 1 and 4. With Flettner rotors, lift coefficient values of 10 to 15 are not unusual and even higher numbers are not impossible. Comparisons between Flettner rotors and hydrofoils made clear that higher forces can be obtained with the Flettners [22].



Figure 3: Commercial "wind-hybrid" cargo ship E-Ship 1.

1.2 MOTIVATION FOR THIS THESIS

It is a hefty challenge to setup a physical experiment due to the rotation of the cylinder. As such, not much experimental data is available about the subject. One thing that is clear though, is that the flow is very complex. Examples for this are the occurrence of the inverse Magnus-effect, observed from Reynolds number $0.8 \cdot 10^5$ (according to Kim et al. [15]) at very low spin rates, or the incidence of a negative drag at Reynolds number 200, from a numerical simulation from Mittal and Kumar [17]. Especially this last phenomenon caught the interest of the author. Where physical experimenting is challenging, CFD are a very valuable tool to answer many questions about the subject.

1.3 RESEARCH QUESTIONS

Few studies focus on low Reynolds numbers and not much experimental data is available. This thesis will use the work done by Mittal and Kumar [17] as a basis to continue to investigate the flow properties at low Reynolds numbers. The following research questions are posed:

- How are the lift and drag generated by the cylinder related to both the spin rate and the Reynolds number?
- For which spin rates do 2D simulations give a realistic reflection of the actual flow? Furthermore, if 2D simulations are incapable of doing this, to what end are lift and drag values still usable?
- When using isogeometric analysis in combination with the residual based variational multi-scale method, can the negative drag observed by Mittal and Kumar [17] be reproduced?

1.4 SCOPE OF THIS THESIS

At first, the focus will be on 2D simulations for several spin rates up to $\alpha = 6.0$ for a large range of Reynolds numbers within the laminar flow regime. It is well known that at around the Reynolds number of 800, three-dimensional effects are starting to kick in. As such, the particular range of interest lies between Reynolds numbers 50 and 400. For the 3D simulations, only Reynolds number 200 will be used due to limitations on the available computational power.

1.5 READING GUIDE

In chapter 2, the fundamentals of the flow around a cylinder are given using the currently available literature. This should provide a sufficient background for the physics that are involved. Chapters 3 and 4 cover the setup of the numerical experiment: chapter 3 addresses the numerical method by explaining the concepts of isogeometric analysis and the residual-based variational multiscale method. Chapter 4 encompasses a description the geometry of the mesh, initial conditions and boundary conditions and provides justifications for choices that had to be made to provide sufficient accuracy with balanced computational effort. At the end of this chapter, the validation of the numerical setup is performed by comparing the initial results to existing data. The results from the experiments are presented in chapter 5 and an analysis is performed. Due to the vast amount of data, only relevant observations are given and discussed in this chapter. For an overview of all results, the reader is forwarded to appendix D. This thesis wraps up with chapter 6, where conclusions are drawn and recommendations are proposed for future work.

PHYSICS OF THE FLOW AROUND A CYLINDER

In this chapter, the physics of the flow around a cylinder are discussed. Firstly, a brief overview is given of the case of the stationary cylinder. Hereafter, the reader is introduced to the characteristics when adding a rotation, explaining the basic concepts, and providing a summary of previous work. This chapter should provide sufficient background information to the reader with regard to rotating cylinders.

2.1 THE STATIONARY CYLINDER

The flow around a stationary is one of the most investigated problems within fluid mechanics and is often used as a benchmark for several numerical problems. The flow properties depend highly on the Reynolds numbers, which is defined here as:

$$\text{Re} = \frac{u_\infty D}{\nu}. \quad (2)$$

Here, u_∞ represents the free stream velocity, far away from the cylinder. ν is the kinematic viscosity of the fluid and the diameter of the cylinder, D is used for the length scale.

At very low Reynolds numbers (approximately $\text{Re} < 5$), a creeping flow is observed. This is the only regime where vortices or vortex shedding are not observed. As the Reynolds number increases, vortices can be observed in the wake. From $\text{Re} = 40$, periodic vortex shedding starts to occur and ends up in the well known Von Karman vortex street. At $\text{Re} = 100$, the flow has barely any three-dimensional effects and this setting is often used as a benchmark test for numerical simulations. Where it is generally known that a laminar flow can be modelled well by 2D simulations, the same cannot be said about turbulent flow. Already at $\text{Re} = 800$, 3D effects dominate the flow and the behaviour of the boundary layer changes with increasing Reynolds number, as can be seen in figure 4.

2.2 THE ROTATING CYLINDER

The physics of the rotating cylinder are known to be very complex. In many studies, explanations are given for several anomalies, without irrefutable arguments. A first source for these difficulties lies in the fact that the flow is highly dependant on the Reynolds number






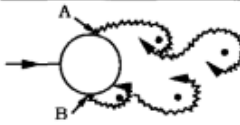
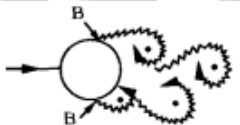
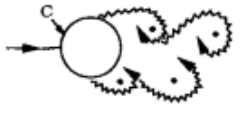

a)		No separation. Creeping flow	$Re < 5$
b)		A fixed pair of symmetric vortices	$5 < Re < 40$
c)		Laminar vortex street	$40 < Re < 200$
d)		Transition to turbulence in the wake	$200 < Re < 300$
e)		Wake completely turbulent. A: Laminar boundary layer separation	$300 < Re < 3 \times 10^5$ Subcritical
f)		A: Laminar boundary layer separation B: Turbulent boundary layer separation; but boundary layer laminar	$3 \times 10^5 < Re < 3.5 \times 10^5$ Critical (Lower transition)
g)		B: Turbulent boundary layer separation; the boundary layer partly laminar partly turbulent	$3.5 \times 10^5 < Re < 1.5 \times 10^6$ Supercritical
h)		C: Boundary layer com- pletely turbulent at one side	$1.5 \times 10^6 < Re < 4 \times 10^6$ Upper transition
i)		C: Boundary layer com- pletely turbulent at two sides	$4 \times 10^6 < Re$ Transcritical

Figure 4: Flow regimes for a stationary cylinder for varying Reynolds numbers, retrieved from Fredsoe and Sumer [11].

and the spin rate α . As u_∞ is present in the definitions of both the Reynolds number as the spin rate, a presumption that a correlation between these parameters can be established, seems logical.

2.3 SUMMARY OF PREVIOUS WORK

2.3.1 Prandtl's limit

One of the first studies on the phenomenon of the Magnus effect came from Prandtl [23]. In his experiments, large lift forces from the rotating cylinder were measured, compared to regular airfoils. A maximum lift coefficient of $C_L = 4\pi$ was proposed from a theoretical point of view. This value became known as Prandtl's limit and was considered as the maximum obtainable lift for a very long time. Later studies show that this limit could be exceeded with high spin rates.

2.3.2 Simulations at high Reynolds numbers

Breuer [3] performed a study on the validity of several LES methods for high Reynolds number for a subcritical flow past a stationary cylinder. This test case was to be considered very challenging for LES at that time. The simulations were performed at Reynolds number $1.4 \cdot 10^5$ for several grid sizes and sub-grid scale models, and are compared with experimental results. From his simulations, it became clear that the modelling of the sub-grid scales is crucial for an accurate representation of the real flow. As for the grid: refinement of the grid did not necessarily led to improved results for all quantities, which Breuer called "an astonishing outcome". However, the coarse grids gave larger deviations in the wake.

A study about a LES of the flow past a rotating cylinder for high Reynolds numbers was published by Karabelas in 2010 [14]. His objective was to resolve the physics of the flow for several spin ratios at Reynolds number $1.4 \cdot 10^5$. The validation was performed by comparing the results with other numerical results and experimental data. Karabelas' results prove the importance of the so-called "rotary boundary layer". This is the boundary layer of the cylinder in which the direction of the velocity vector is parallel to the flow on the suction side and opposite on the pressure side. On the suction side, the rotary boundary layer energises the fluid flow. The consequence is that the main flow stays attached longer to the cylinder. This is especially clear at higher spin ratios: at spin ratio $\alpha = 2.0$, the rotary boundary layer is significantly stronger than the mean magnitude of the free-stream velocity, inducing a collapse of the vortex on the suction side which is observed at lower spin ratios. Another observation is that the stagnation point at the upstream side of the cylinder moves azimuthally towards the pressure side. The rotary boundary layer is visible at all Reynolds numbers and can be recognised back in figure 1.

The coefficients for lift and drag depend both on the spin ratio and the Reynolds number. Apparently, the lift coefficient is highly dependant on the spin ratio, which is to be expected, as the rotation of the cylinder is the main source of non-periodic lift. The drag however, is highly dependant on the Reynolds number, and is affected less by the spin ratio. Karabelas further states that two different regimes can be distinguished. At low spin ratio's, the lift coefficient is highly periodic as can be seen in a figure 5. For high spin ratio's, the lift coefficient becomes more or less constant, with only osculations which are very small compared to the average value. In between these two regimes, at "medium" spin ratio's, a transition can be observed. The drag coefficient also shows some fluctuations, but these are relatively small at all spin ratio's. As the spin ratio increases, the drag coefficient diminishes. This can be explained by the disappearing vortices directly downstream of the cylinder.

2.3.3 *Flow properties for low Reynolds numbers*

A study about rotating cylinders was performed by Mittal and Kumar [17] in 2003 for the two-dimensional flow physics around a spinning cylinder at Reynolds number 200 and for various spin ratio's for $\alpha \leq 5.0$. In their study, it became apparant that several types of flow regimes occur, depending on α . For low spin ratio's, $0.0 < \alpha < 1.90$, an asymmetric von Karman vortex street can be observed in the wake of cylinder. At about $\alpha = 1.90$, the vortex street fades. From this stage, a single vortex on the pressure side can be observed, but no vortices are shed until $\alpha = 4.34$. At this point, vortex shedding reappears but at a very low frequency. At the highest spin rates, $\alpha > 4.8$, the flow stabilises once more. A proposition is made to explain this behaviour: with increasing spin rates, the strength of the vorticity at the cylinder also builds, but the streamlines also narrow. The magnitude of the vorticity has to be very extensive to be carried to the outer flow. At spin rates of $\alpha \approx 4.5$, vorticity is allowed to build up until it is strong enough to escape to the outer region, explaining the low frequency vortex shedding.

For the varying spin ratio's, lift and drag values are also monitored, Mittal and Kumar [17]'s results are reprinted in figure 5 . As for the lift, average values for higher spin ratio's far exceed Prandtl's mathematical limit of 4π and keep increasing for higher spin ratio's. When vortex shedding occurs, the produced lift has a strong oscillatory character. The same holds for the values of the drag. However, a very curious result, which was noted but not further discussed, was the observance of a negative drag (which in fact can be called "thrust") in certain situations. For $\alpha \approx 3.0$, the drag value is very close to zero, and becomes slightly negative on average for $3.2 < \alpha < 4.75$. At the highest spin ratio's, when the second regime of vortex shedding diminishes, the drag is yet again positive.

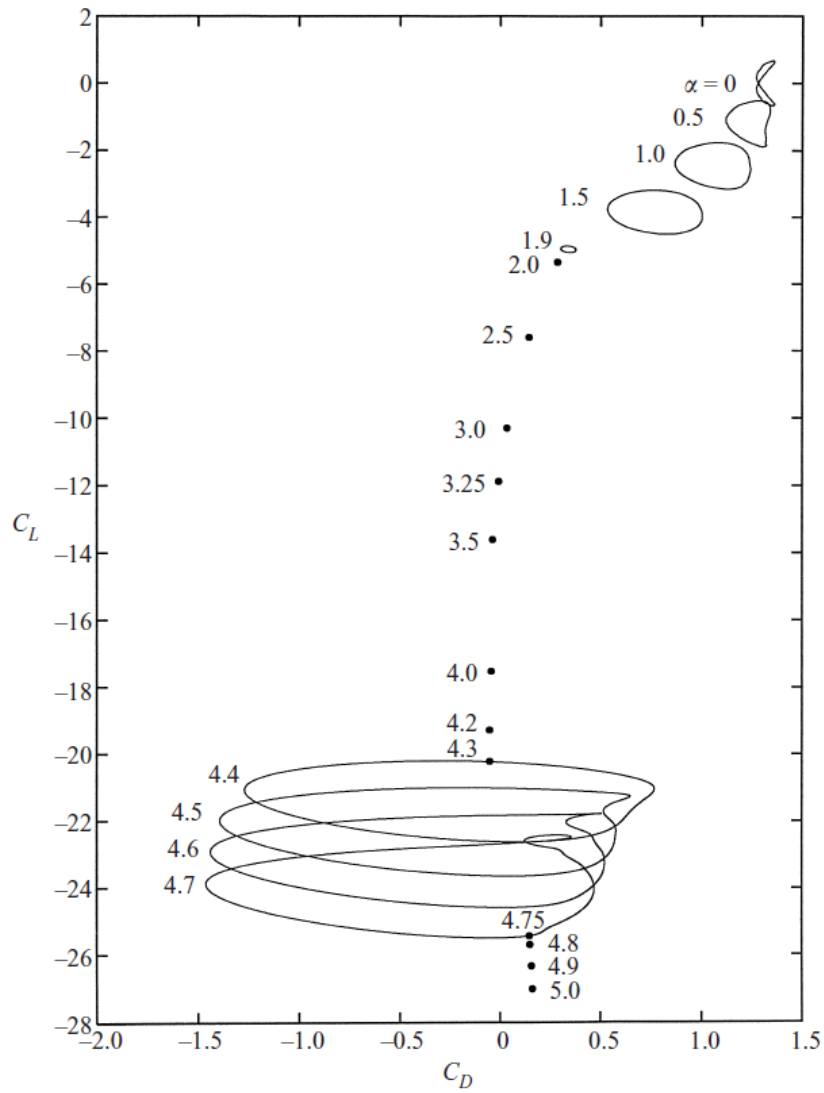


Figure 5: Lift coefficients plotted against drag coefficients for simulations at Reynolds number 200 for several spin rates, retrieved from Mittal and Kumar [17].

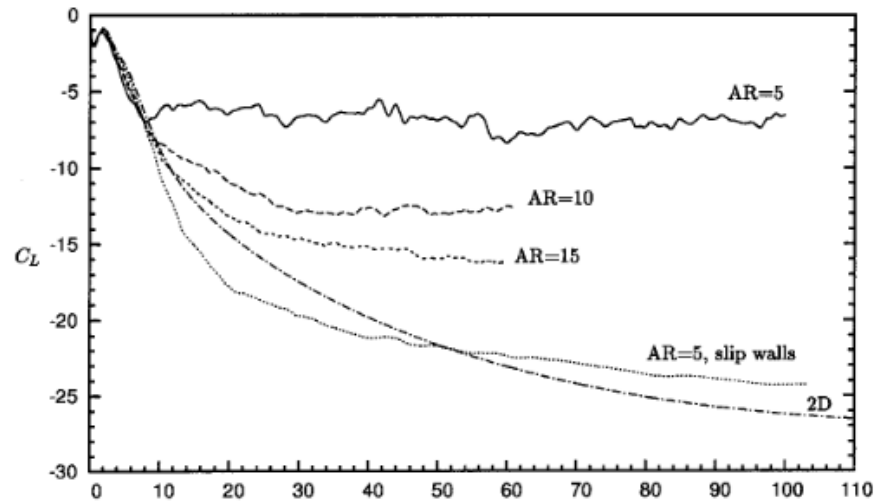


Figure 6: Lift coefficients for 3D simulations at Reynolds number 200 for spin rate $\alpha = 5.0$, retrieved from Mittal [16].

2.3.4 3D simulations at high spin rate

Continuing on this topic, a new simulation was performed by Mittal [16] a year later. Here, the flow properties, Reynolds number 200 and spin rate $\alpha = 5.0$, are kept constant, and several 3D simulations are performed on a cylinder of varying size. A major conclusion was that the flow is highly three-dimensional and unstable. The lift and drag values from the 2D simulation were not reached as depicted in figure 6, even for the most ideal case: an aspect ratio of 5.0 with infinite end plates. Furthermore, the importance of the aspect ratio becomes clear from this plot: low aspect ratio's do not even come close. As for the drag, in general higher values are obtained in the 3D simulation, there is no time frame in which the drag becomes negative, though at this spin rate, no negative drag was neither present in the 2D case.

NUMERICAL METHOD

In this chapter, the numerical method for the present work is discussed. First, an global overview is given of the numerical method and the basic concepts of IGA and RBVMS are explained. In the following two sections, a more in-depth description, containing the mathematical basis, is given. As for the IGA part, it is assumed that the reader is familiar with the basic concepts of the Finite Element Method. An introduction to FEM is included in appendix A. In the last three sections of this chapter, the time integration method, the used software to implement the code and the extraction of the forces are covered.

3.1 OVERVIEW OF THE NUMERICAL METHOD

Confidence in the numerical method is one of the most important things with the topic at hand. As the number of previous experiments, both physically and numeric, is low, options for validation are scarce. As such, validation will be done using benchmark results from a stationary cylinder and a comparison with numeric results from Mittal and Kumar [17]. To expand the method to other Reynolds numbers and spin rates, accuracy of the numerical method is of upmost importance. This accuracy is provided by combining the RBVMS method with IGA. A global description will be given of both.

The concept of the VMS was introduced in 1995 by “Multiscale phenomena: Green’s functions, the Dirichlet to Neumann formulation, subgrid scale models, bubbles and the origins of stabilized methods” [18] and has a very close resemblance to classic LES techniques. As with LES, coarse scales are differentiated from small scales, where as the coarse scales are resolved. The biggest difference to LES is that variational projections are used instead of the use of filtered equations. However, eddy viscosities were only included in the small scales and the effects were not applied into the coarse scales. RBVMS was introduced in 2005 by Hughes, Calo, and Scovazzi [12] and resolved this issue to improve accuracy and stability: an extra connection is added between the coarse and the small scales. Coarse scales are still resolved, but do incorporate the effect of the small scales.

IGA can be seen as an extension to the finite elements method and was introduced by T.J.R. Hughes in 2007. Classic finite elements use a mesh of straight lines to model objects; boundaries etc. Creating a cylinder, or in general any curved object, proves to be difficult: even if the grid size is very small, a cylinder can never be modelled exactly

and can only be approached. A study by Catalano, Wang, Iaccarino, and Moin [4] showed that for LES, although at high Reynolds numbers in their case, a fine mesh near the cylinder wall is crucial to model the near-wall effects correctly. It even showed that meshes that were not refined enough, would cause smooth cylinders to behave like rough cylinders. To represent curves as good as possible, a high level of refinement is mandatory.

The use of straight lines stands in great contrast to the usage of CAD. In CAD, curves can be represented exactly using mathematical formulations, NURBS specifically. IGA combines the worlds of CAD and CAE, as NURBS meshes are incorporated into FEM. The result is the application of all the tools that FEM provides on meshes which represent the exact geometry of an object, resulting in less computational power to achieve the same result, higher accuracy, or both.

Combining RBVMS and IGA gives a numerical method which provides high accuracy at acceptable computational costs. As the case at hand involves a rotating cylinder, a perfect example of a curved object that creates a strong centrifugal motion of the fluid at the back, the mix of these two numerical tools would provide a solid base for several simulations with varying conditions. An example of the use of this combination is demonstrated by Bazilevs and Akkerman [1]. As a test case, a Taylor-Couette flow was modelled using RBVMS and IGA. The results converged swiftly to DNS results and even gave good solutions on coarser grids.

3.2 NURBS

3.2.1 Introduction

NURBS can be used to exactly represent curvature in a geometrical space using mathematical expressions. This means that curved figures, such as circles, can be constructed exactly without discontinuities. In comparison with classic finite element meshes, NURBS meshes do not have "nodes", but do have "knots", which share more or less the same functionality. The main difference is that the geometry is defined by straight lines between the nodes in classic finite elements, whereas NURBS curves are used in IGA. So called "control points" can be found in between knots and define the curvature of the line between the two knots. B-spline curves are built from a linear combination of basis functions, polynomials. The polynomial order of these basis functions determine which curves are possible. For example, first-order NURBS can only represent straight lines, whereas second-order NURBS can be used to create a perfect round circle.

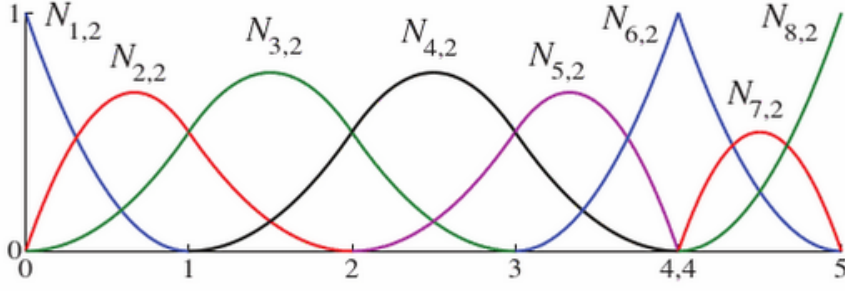


Figure 7: An example of the quadratic basis functions for a knotvector consisting of seven knots, with multiplicity of 2 at the fifth knot. Retrieved from [6].

3.2.2 From knotvectors to B-splines

NURBS curves are obtained from B-splines. A B-spline has a corresponding knot vector, a set of coordinates in a parametric space. An example of a knot vector for second order NURBS is $\{0, 0, 0.25, 0.25, 0.5, 1, 1\}$. Some characteristics are visible from this elemental example: the knots range from 0 to 1 and are also ordered from 0 to 1. Knots can be repeated, in this case, 0, 0.25 and 1 have a multiplicity of 2. In fact, the recurrence of 0 and 1 is dependant on the number of basis functions, n , which are used for the B-spline, and the polynomial order, p . A knot vector can be described by the following general expression:

$$\Xi = \{\xi_1, \xi_2, \dots, \xi_{n+p+1}\}. \quad (3)$$

The basis function for a zero order B-spline is given by the following expression:

$$N_{i,0}(\xi) = \begin{cases} 1 & \text{if } \xi_i \leq \xi < \xi_{i+1}, \\ 0 & \text{otherwise.} \end{cases} \quad (4)$$

Then, the p -th order basis function can be formulated recursively:

$$N_{i,p}(\xi) = \frac{\xi - \xi_i}{\xi_{i+p} - \xi_i} N_{i,p-1}(\xi) + \frac{\xi_{i+p+1} - \xi}{\xi_{i+p+1} - \xi_{i+1}} N_{i+1,p-1}(\xi). \quad (5)$$

A visualisation of the basis functions is presented in figure 7.

B-spline curves can then be created from a linear combination of B-spline basis functions:

$$\underline{C}(\xi) = \sum_{i=1}^n N_{i,p}(\xi) \underline{B}_i. \quad (6)$$

Here, \underline{B} is the collection of all the control points corresponding to the basis functions. When looking at the geometrical space, the location of the control points define the curvature of the B-spline curve. When knots are repeated, the control points are located on the curve itself. An example of a B-spline is given in figure 8.

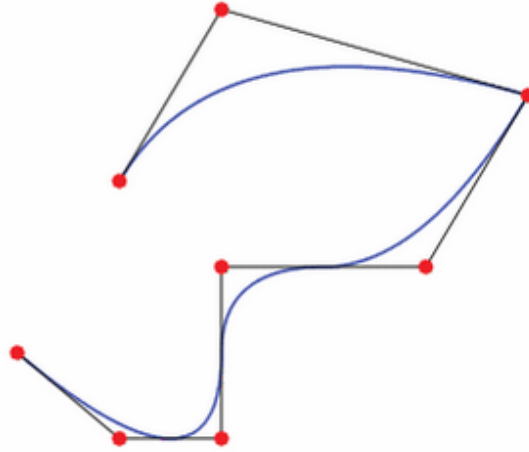
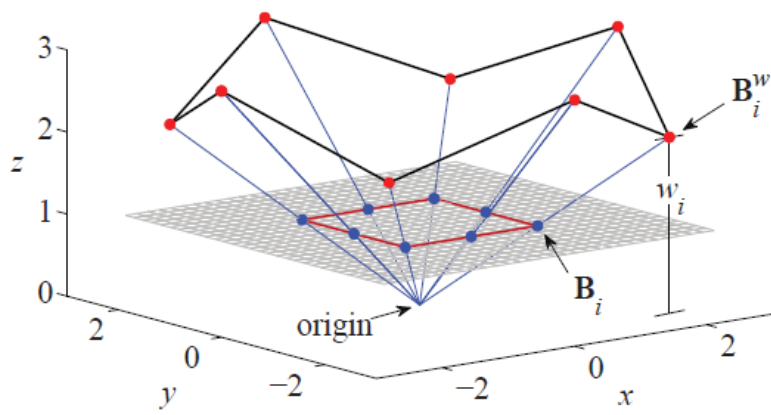


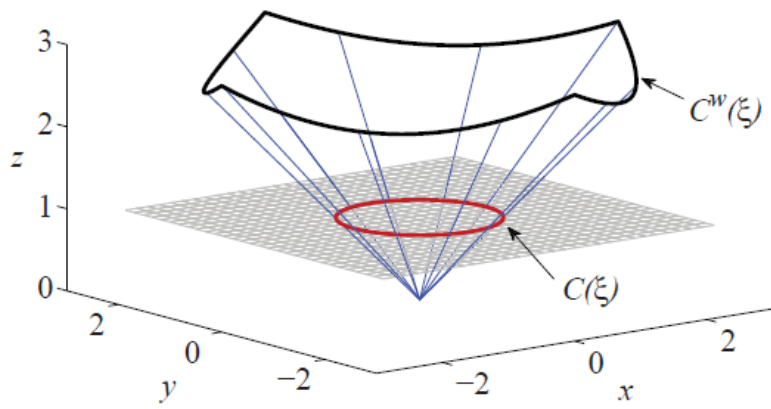
Figure 8: An arbitrary example of a geometric B-spline curve corresponding to the basis functions from figure 7. The red squares represent the control points. Retrieved from [6].

3.2.3 From B-splines to NURBS

More complex geometrical curves can be obtained by using a projection. A good example for this, is the description of a circle. This mathematical figure can be constructed by projecting a quadratic B-spline curve in \mathbb{R}^3 onto \mathbb{R}^2 . The result is a NURBS curve as shown in figure 9.



(a) Control polygons



(b) Curves

Figure 9: A 2D circle is constructed from a projection from \mathbb{R}^3 onto \mathbb{R}^2 . Retrieved from Cottrell, Hughes, and Bazilevs [6].

3.3 RESIDUAL-BASED VARIATIONAL MULTISCALE METHOD

3.3.1 Introduction

RBVMS resolves the Navier-Stokes equations and uses a model for the smaller scales of the turbulence cascade. For RBVMS, the incompressible Navier-Stokes equations are decomposed into coarse-scale and fine-scale terms. Here, the coarse-scale terms are computed exactly, whereas the fine-scale terms are approximated using the coarse-scale terms.

In this paragraph, the theory behind RBVMS modeling of incompressible flows is explained concisely. First, the variational form of the incompressible Navier-Stokes equations is derived from the strong form using Galerkin's method. Secondly, this variational form is separated into a coarse scale and a fine scale. Finally, a residual is introduced to replace the fine scale terms as an expression of the coarse scale. The result is a semi-discretised variational formulation of the Navier-Stokes equations.

3.3.2 Variational form of the Navier-Stokes equations

Continuity equation

The incompressible Navier-Stokes equations assume the conservation of mass and incompressibility of a fluid, implying a constant density ρ . Conservation of mass implies that:

$$\frac{\partial \rho}{\partial t} + \nabla \cdot (\underline{u}\rho) = 0. \quad (7)$$

Using the chain rule, equation (7) can be rewritten to:

$$\frac{\partial \rho}{\partial t} + \underline{u} \cdot \nabla \rho + \rho(\nabla \cdot \underline{u}) = 0. \quad (8)$$

When assuming incompressibility, both the time and spacial derivatives of the density vanish from the equation, resulting in the continuity equation for incompressible fluids which states that the divergence of the velocity equals zero:

$$\nabla \cdot \underline{u} = 0. \quad (9)$$

Strong form of the incompressible Navier-Stokes equations

The Navier-Stokes equations describe the motion of homogenous viscous fluids. These balance equations are derived by applying Newton's second law to fluid motion. The following equation represents

the momentum balance for an incompressible fluid in its differential strong form:

$$\frac{\partial \underline{u}}{\partial t} + \nabla \cdot (\underline{u} \otimes \underline{u}) + \nabla p = \nu \Delta \underline{u} + \underline{f}. \quad (10)$$

Here, \underline{u} is the velocity-vector, p is the pressure divided by the fluid density ρ , ν is the kinematic viscosity and \underline{f} is a force-vector. The terms respectively depict the change of velocity with time, convection, pressure, diffusion¹ and external body forces. The latter term only contains the gravitational acceleration.

Variational form

First, a variational form of the Navier-Stokes equations is derived using Galerkin's method. Consider the space domain $\Omega \subset \mathbb{R}$ with lateral boundary Γ . Let \mathcal{V} be a vector space which contains both the trial solution $\mathbf{U} = \{\underline{u}, p\}$ and the weighting function $W = \{\underline{w}, q\}$. The bilinear form $(\cdot, \cdot)_{\Omega}$ represents the L^2 inner product with respect to the domain Ω . A variational form can be then stated by multiplying every term in equation (10) by the weighting function \underline{w} and every term in equation (9) by the weighing function q and integrating both equations over the domain Ω :

$$\begin{cases} \left(\underline{w}, \frac{\partial \underline{u}}{\partial t} \right)_{\Omega} + (\underline{w}, (\underline{u} \cdot \nabla) \underline{u})_{\Omega} + (\underline{w}, \nabla p)_{\Omega} = (\underline{w}, \nu \Delta \underline{u})_{\Omega} + (\underline{w}, \underline{f})_{\Omega} \\ (q, \nabla \cdot \underline{u})_{\Omega} = 0. \end{cases} \quad (11)$$

Integration by parts is used on the pressure term and the diffusion term. Two of the resulting terms contain an integral over the boundary, which are obtained after applying Gauss' divergence theorem. Both terms vanish from the equation due to the boundary conditions. A detailed derivation can be found in appendix B. Equation (11) is rewritten to:

$$\begin{aligned} & \left(\underline{w}, \frac{\partial \underline{u}}{\partial t} \right)_{\Omega} + (\underline{w}, (\underline{u} \cdot \nabla) \underline{u})_{\Omega} - (\nabla \cdot \underline{w}, p)_{\Omega} + (q, \nabla \cdot \underline{u})_{\Omega} \\ & = -(\nabla \underline{w}, \nu \nabla \underline{u})_{\Omega} + (\underline{w}, \underline{f})_{\Omega}. \end{aligned} \quad (12)$$

¹ The divergence term actually equals $\nabla \cdot (2\nu(\nabla^s \underline{u}))$. Due to the continuity equation, this expression is simplified to $\nu \Delta \underline{u}$.

Now, define the form $L(W)$ comprising the forcing term from equation (12), $B_1(W, \mathbf{u})$ the bilinear terms containing \mathbf{u} and $B_2(W, \mathbf{u}, \mathbf{u})$ the trilinear term:

$$\begin{cases} L(W) = (\mathbf{w}, \mathbf{f})_{\Omega} \\ B_1(W, \mathbf{u}) = \left(\mathbf{w}, \frac{\partial \mathbf{u}}{\partial t} \right)_{\Omega} + (\nabla \mathbf{w}, \nu \nabla \mathbf{u})_{\Omega} - (\nabla \cdot \mathbf{w}, p)_{\Omega} + (\mathbf{q}, \nabla \cdot \mathbf{u})_{\Omega} \\ B_2(W, \mathbf{u}, \mathbf{u}) = (\mathbf{w}, (\mathbf{u} \cdot \nabla) \mathbf{u})_{\Omega}. \end{cases} \quad (13)$$

Equation (12) can then be rewritten to the so called variational formulation of the Navier-Stokes equations:

$$\text{Find } \mathbf{u} \in \mathcal{V} \text{ such that } \forall W: \quad (14)$$

$$B(W, \mathbf{u}) = B_1(W, \mathbf{u}) + B_2(W, \mathbf{u}, \mathbf{u}) = L(W).$$

3.3.3 Residual-based multiscale method

Scale separation

The vector space \mathcal{V} is decomposed into a coarse-scale and a fine-scale subspace, respectively $\bar{\mathcal{V}}$ and \mathcal{V}' :

$$\mathcal{V} = \bar{\mathcal{V}} \oplus \mathcal{V}'. \quad (15)$$

Corresponding to these vector spaces, the trial solution and the weighting functions are also decomposed:

$$\begin{cases} W = \bar{W} + W' \\ \mathbf{u} = \bar{\mathbf{u}} + \mathbf{u}'. \end{cases} \quad (16)$$

The scale separation is applied to the equation (14). The original equation is split into two separate equations, one containing the coarse-scale weighting function and the other one containing the fine-scale weighting function. This yields:

$$\begin{cases} B(\bar{W}, \bar{\mathbf{u}} + \mathbf{u}') = L(\bar{W}) \\ B(W', \bar{\mathbf{u}} + \mathbf{u}') = L(W'). \end{cases} \quad (17)$$

Equation (17) can be expanded to:

$$\begin{cases} B_1(\bar{W}, \bar{U}) + B_1(\bar{W}, \underline{u}') + B_2(\bar{W}, \bar{U}, \bar{U}) \\ \quad + B_2(\bar{W}, \bar{U}, \underline{u}') + B_2(\bar{W}, \underline{u}', \bar{U}) + B_2(\bar{W}, \underline{u}', \underline{u}') = L(\bar{W}) \\ B_1(W', \bar{U}) + B_1(W', \underline{u}') + B_2(W', \bar{U}, \bar{U}) \\ \quad + B_2(W', \bar{U}, \underline{u}') + B_2(W', \underline{u}', \bar{U}) + B_2(W', \underline{u}', \underline{u}') = L(W'). \end{cases} \quad (18)$$

Here, the purple terms containing a combination of \bar{U} and \underline{u}' correspond to the cross-stress terms, where as the orange terms correspond to the Reynolds stress term.

Writing the first equation of (18) using the terms from equation (13) yields:

$$\begin{aligned} & \left(\bar{w}, \frac{\partial \bar{u}}{\partial t} \right)_{\Omega} + (\nabla \bar{w}, \nu \nabla \bar{u})_{\Omega} - (\nabla \cdot \bar{w}, \bar{p})_{\Omega} + (\bar{q}, \nabla \cdot \bar{u})_{\Omega} \\ & \left(\bar{w}, \frac{\partial \underline{u}'}{\partial t} \right)_{\Omega} + (\nabla \bar{w}, \nu \nabla \underline{u}')_{\Omega} - (\nabla \cdot \bar{w}, p')_{\Omega} + (\bar{q}, \nabla \cdot \underline{u}')_{\Omega} \\ & + (\bar{w}, (\bar{u} \cdot \nabla) \bar{u})_{\Omega} + (\bar{w}, (\bar{u} \cdot \nabla) \underline{u}')_{\Omega} + (\bar{w}, (\underline{u}' \cdot \nabla) \bar{u})_{\Omega} \\ & + (\bar{w}, (\underline{u}' \cdot \nabla) \underline{u}')_{\Omega} = (\bar{w}, f)_{\Omega}. \end{aligned} \quad (19)$$

The incompressible Navier-Stokes equations are now written in their variational multiscale form. During this derivation, no approximations are made: equations (18) and (19) are still equivalent to equation (10). The goal of RBVMS is to solve these equations on the coarse scale and to model the fine scales to encapsulate the turbulence. To do this, the effects of the fine scales are substituted by a function which depends on the coarse scale:

$$\bar{u}' \approx \tilde{u}' = \tilde{F}' \left(\tilde{u}, \text{Res} \left(\tilde{u} \right) \right). \quad (20)$$

Here, the tilde denotes that an approximation is made. This approximation for \bar{U} is substituted back in equation (17):

$$B(\bar{W}, \tilde{u}' + \tilde{F}' \left(\tilde{u}, \text{Res} \left(\tilde{u} \right) \right)) = L(\bar{W}). \quad (21)$$

It should be noted that an error is constituted this way.

Implementation

Equation (19) is rewritten, while the coarse scale weighting function (\bar{w}, \bar{q}) and trial solution (\underline{u}, \bar{p}) are respectively discretised by (w^h, q^h) and (\underline{u}^h, p^h) . Here, the h -superscript denotes the mesh parameter. Furthermore, the following assumption is invoked: both $\left(\frac{\partial w^h}{\partial t}, \underline{u}'\right)_\Omega$ and $(\nabla w^h, \nu \nabla \underline{u}')_\Omega$ are equal to zero, as well as derivatives of \underline{u}' are neglected:

$$\begin{aligned}
& \left(\bar{w}, \frac{\partial \bar{u}}{\partial t}\right)_\Omega + (\nabla \bar{w}, \nu \nabla \bar{u})_\Omega - (\nabla \cdot \bar{w}, \bar{p})_\Omega + (\bar{q}, \nabla \cdot \bar{u})_\Omega \\
& \left(\bar{w}, \frac{\partial \underline{u}'}{\partial t}\right)_\Omega + (\nabla \bar{w}^h, \nu \nabla \underline{u}')_\Omega - (\nabla \cdot w^h, p')_\Omega + (q^h, \nabla \cdot \underline{u}')_\Omega \\
& + (w^h, (\underline{u}^h \cdot \nabla) \underline{u}^h)_\Omega + (w^h, (\underline{u}^h \cdot \nabla) \underline{u}')_\Omega + (w^h, (\underline{u}' \cdot \nabla) \underline{u}^h)_\Omega \\
& + (w^h, (\underline{u}' \cdot \nabla) \underline{u}')_\Omega = (w^h, f)_\Omega.
\end{aligned} \tag{22}$$

The next step is to approximate the fine-scale terms (i.e. the terms containing a prime) by using residuals. This is done by stating that \underline{u}' and p' are equal to the product of a constant (respectively τ_M and τ_C) and a function (respectively r_M and r_C) of the coarse-scale trial solution:

$$\begin{cases} \underline{u}' \approx -\tau_M \cdot R_M(\underline{u}^h, p^h) \\ p' \approx -\tau_C \cdot R_C(\underline{u}^h), \end{cases} \tag{23}$$

$$\text{where: } \begin{cases} R_M(\underline{u}^h, p^h) = \frac{\partial \underline{u}^h}{\partial t} + \underline{u}^h \cdot \nabla \underline{u}^h + \nabla p^h - \nu \Delta \underline{u}^h - \underline{f} \\ R_C(\underline{u}^h) = \nabla \cdot \underline{u}^h. \end{cases} \tag{24}$$

The functions R_M and R_C are derived from fine-scale equation for the weighting function, i.e. the second equation of (17).

By substituting (23) into (22) and doing some rearranging, the following semi-discretised variational formulation of the incompressible Navier-Stokes equations remains (to improve the readability of the

equation, $R_M(\underline{u}^h, p^h)$ and $R_C(\underline{u}^h)$ are replaced by respectively R_M and R_C):

Find \underline{U}^h such that $\forall W^h$:

$$\begin{aligned}
& \left(\bar{w}, \frac{\partial \bar{u}}{\partial t} \right)_{\Omega} + (\nabla w^h, \nu \nabla \underline{u}^h)_{\Omega} - (\nabla \cdot w^h, p^h)_{\Omega} \\
& + (w^h, (\underline{u}^h \cdot \nabla) \underline{u}^h)_{\Omega} + (\nabla \cdot q^h, \underline{u}^h)_{\Omega} \\
& + (\nabla \cdot w^h, \tau_C R_C)_{\Omega} - (q^h, \nabla \cdot (\tau_M R_M))_{\Omega} \\
& + (\tau_M R_M \cdot \nabla) \underline{u}^h \\
& = (w^h, \underline{f})_{\Omega}
\end{aligned} \tag{25}$$

In this formulation, the first line contains the Galerkin method applied to \underline{u}^h and p^h . The second and third line contain all the terms with residuals which can be seen as stabilising terms.

3.4 TIME INTEGRATION METHOD

Time integration is done using the Generalised- α method, developed by Chung and Hulbert [5], applied to the Navier-Stokes equations as implemented by Jansen, Whiting, and Hulbert [13]. Generalized- α is an implicit method that damps out the highest frequencies, thus allowing energy dissipation and yielding second order accuracy. The method is unconditionally stable for a certain range of its input parameter.

The method uses one parameter which can vary between zero and one: ρ_{∞} (not to be confused with density). If ρ_{∞} is set to 1, all frequencies, including the high frequencies, are preserved, resulting effectively in a midpoint integration scheme. If ρ_{∞} is chosen to be zero, the highest frequencies are damped aggressively. An example of the principle of this dampening is provided in figure 10.

Jansen, Whiting, and Hulbert [13] performed a simulation to validate the Generalised- α method on the flow past a circular cylinder at Reynolds number 100, which is very much comparable to the current numerical setup. From their results, an intermediate ρ_{∞} is desirable: setting this parameter to one pollutes the entire solution, where as a value of zero yields a very damped solution. Furthermore, they stated that "the period and amplitude of both the lift and the drag are very weak functions ρ_{∞} ". As for the current numerical setup, a compromised ρ_{∞} of 0.5 is chosen.

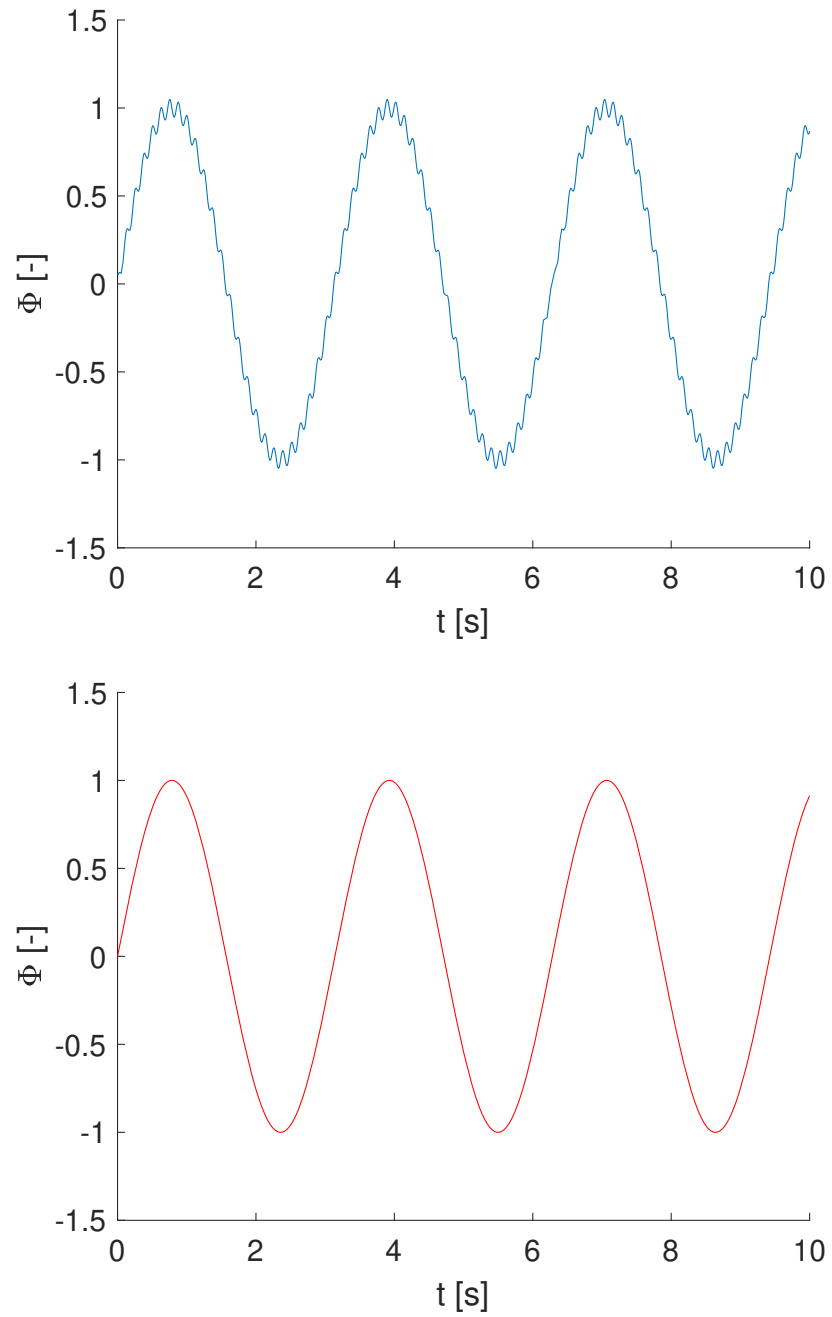


Figure 10: An example is given of the dampening of the high frequencies. In the top graph, the solution is given without filtering, in the bottom graph, the highest frequency is filtered out.

3.5 SOFTWARE OVERVIEW AND COMPUTATIONAL COSTS

The numerical method is implemented using a C++ software package GSLCL (General Semi-Linear Conservation Law) developed by I. Akkerman. Simulations are executed on the Reynolds cluster at TU Delft using Intel Xeon E5-2680 v4 CPU's. 2D calculations are performed using two CPU's (28 cores) with an average calculation time of three hours for a single run at a certain Reynolds number and spin rate. For all 3D calculations, eight CPU's (112 cores) are used for a period of seven consecutive days. To generate the visualisations of the flow, VisIt software from Lawrence Livermore National Laboratory is used.

3.5.1 Force and torque extraction

The total force \underline{F} acting on the cylinder is obtained by integrating the pressure over the cylinder edge:

$$\underline{F} = \oint_{\Gamma_5} p \cdot \underline{n} \, d\Gamma. \quad (26)$$

Here, p denotes the pressure, Γ_5 the cylinder edge and \underline{n} the normal vector on the edge. The magnitude of \underline{F} in streamwise and normal direction, respectively F_x and F_y , are used to calculate the lift and drag coefficients:

$$C_L = \frac{F_y}{0.5\rho u_\infty^2 S}, \quad C_D = \frac{F_x}{0.5\rho u_\infty^2 S}. \quad (27)$$

Here, S is the frontal surface area and equals the diameter D (in the 3D case, the surface area is obtained by multiplying the diameter with the aspect ratio). As D , ρ and u_∞ are normalised in this case, these formulas can be simplified to:

$$C_L = \frac{2F_y}{S}, \quad C_D = \frac{2F_x}{S}. \quad (28)$$

In a similar way, the coefficient for the required torque C_M is calculated from this expression for the angular momentum:

$$C_M = \frac{1}{0.5\rho u_\infty^2 SD} \int_{\Gamma_5} (p \cdot \underline{n}) \times \underline{r} \, d\Gamma. \quad (29)$$

Here, \underline{r} denotes the position vector. When omitting the normalised parameters, the following formula remains:

$$C_M = \frac{2}{S} \int_{\Gamma_5} (p \cdot \underline{n}) \times \underline{r} \, d\Gamma. \quad (30)$$

MESH AND FLOW PARAMETERS

In this chapter, the numerical set-up is discussed. In the first section, a description of the geometrical mesh is given and which boundary conditions are applied for both the two-dimensional as the three-dimensional mesh. In the second section, the influence of several parameters, such as the timestep and the wake length, are assessed and the choices with respect to the mesh are set out. The last section covers the validation of the mesh, this is done by performing a mesh convergence study, as well as a comparison with other physical and numerical experiments.

4.1 MESH DESCRIPTION

4.1.1 Mesh domain

The cylinder is set in the middle of four patches as can be seen in figure 11. The inflow is located at the outer edge of patch 1, where as the outer edges of patches 2 and 4 represent the far field with the undisturbed flow. Patch 3 and 5 contain the wake of the cylinder. The size of the domain can be read from the axis from figure 11, the choices made with respect to the dimensions will be covered in 4.2. The centre of the cylinder is located at coordinate $(0,0)$ and the radius is 0.5, such that the diameter is normalised. The three-dimensional domain is built by extruding the two-dimensional domain along the vertical z -axis as can be seen figure 12.

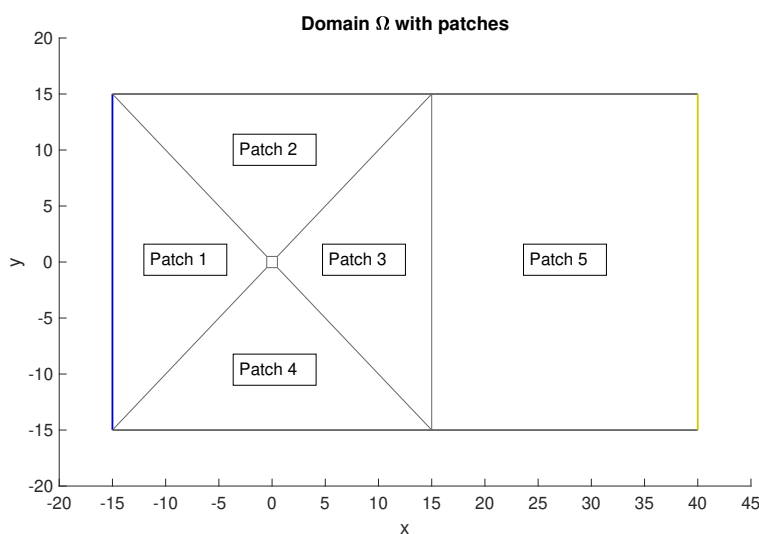


Figure 11: Visualisation of the 2D domain with the five patches

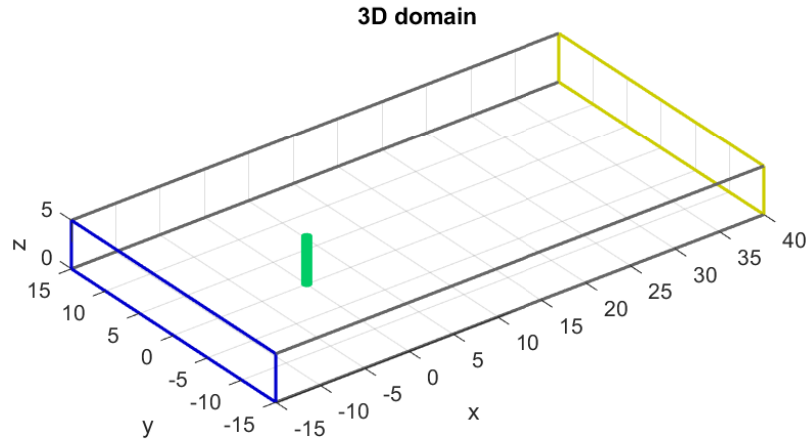


Figure 12: Visualisation of the 3D domain

4.1.2 Boundary Conditions

Dirichlet boundary conditions are imposed on the inflow, the far field boundary and the cylinder surface. At the inflow and the far field, the velocity vector is assumed to correspond to the free stream velocity vector, meaning that the u equals the free stream velocity, where as v is set to zero. In other words, at the inflow, no cross flow is allowed and at the far field, the free slip boundary condition is imposed so the boundary is not penetrable. The mathematical formulation can be written as follows for Γ_1 , Γ_2 and Γ_4 :

$$\begin{cases} \mathbf{u} = \mathbf{u}_\infty \\ v = 0. \end{cases} \quad (31)$$

The numbering of the boundaries is shown in figure 13. At the cylinder surface, a moving no-slip condition is imposed. When the cylinder is not rotating ($\alpha = 0.0$), the velocity at the cylinder surface equals zero. When the cylinder starts rotating clockwise ($\alpha > 0.0$), the u and v are chosen such that the velocity vector is tangential to the cylinder surface and the magnitude equals α times the free stream velocity:

$$\begin{cases} \mathbf{u} = \frac{y}{r} \cdot \alpha \\ v = \frac{x}{r} \cdot \alpha. \end{cases} \quad \text{with } \|\underline{\mathbf{u}}\| = \sqrt{u^2 + v^2} = \alpha \cdot u_\infty \quad (32)$$

r is the radius of the circle, being 0.5 in the current geometry.

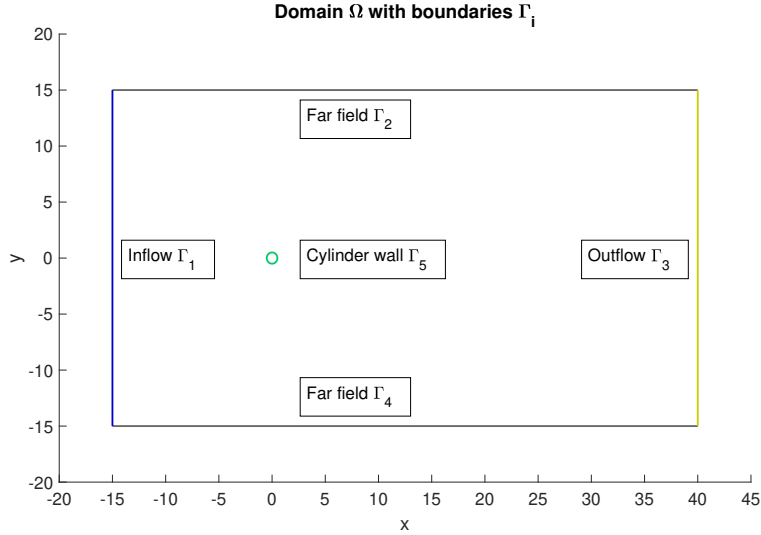


Figure 13: Numbering of the boundaries in 2D

Three-Dimensional Case

In 3D, the same boundary conditions are imposed in the same way as in the 2D case from figure 13, in this case on a surface instead of an edge. As such, the boundary conditions can be described similarly as for Γ_1 , Γ_2 and Γ_4 :

$$\begin{cases} \mathbf{u} = \mathbf{u}_\infty \\ v = 0 \\ w = 0. \end{cases} \quad (33)$$

For the cylinder surface, Γ_5 , this gives:

$$\begin{cases} \mathbf{u} = \frac{\mathbf{y}}{r} \cdot \alpha \\ v = \frac{x}{r} \cdot \alpha \\ w = 0. \end{cases} \quad \text{with } \|\underline{\mathbf{u}}\| = \sqrt{u^2 + v^2} = \alpha \cdot u_\infty \quad (34)$$

On the top and bottom surfaces of the domain (Γ_6 and Γ_7), a free slip condition is imposed. This is done by setting the vertical component of the velocity to zero:

$$w = 0. \quad (35)$$

No penetration of the top and bottom boundaries means that they act as an infinite end plate.

4.1.3 Initial Conditions

Throughout the domain, the velocity vector at all elements is equal to the free stream velocity vector:

$$\begin{cases} u = u_\infty \\ v = 0 \\ w = 0. \end{cases} \quad (36)$$

u_∞ is normalised and thus set to 1. The Reynolds number is varied using a viscosity parameter. The exception is at the boundaries: there, the initial conditions are equal to the boundary conditions.

4.2 MESH OPTIMISATION

4.2.1 Workflow for Validation

An initial mesh is chosen based on benchmarks. The simulation performed with this mesh is compared to both available experimental data at $Re = 100$, $\alpha = 0.0$ and other numerical results $Re = 200$, $\alpha = 1.0$. First, two parameters defining the geometry of the mesh are examined:

- Distance between cylinder and side boundary
- Length of the wake behind the cylinder

The initial mesh is updated, taking into account the results from the study of these two parameters. Next, the target CFL number is determined and a mesh convergence study is performed.

4.2.2 Parameter Sensitivity

Evaluating the far field boundary condition

To justify the boundary condition for a free slip wall at the far field of the cylinder, it has to be proven that the boundary does not influence the fluid flow at the cylinder. To verify this, several simulations are performed with varying domain widths, relative to the diameter of the cylinder. An initial guess for a realistic boundary distance is based on the work from Engelman and Jamnia [10]. With an similar set-up of the mesh and boundary conditions, they concluded that at a distance of fifteen times the cylinder diameter is sufficient for negligible interference. In table 1, the several meshes that were used are summed up with the values representing the flow characteristics. In all meshes, the grid size is more or less the same, enclosing more elements for the meshes with larger boundary distances. The difference relative to the mesh with the largest domain width is displayed in table 2. From these two tables, it can be seen that there is some influence of the boundary for the mesh with a domain width of 20D,

Domain width	20D	30D	40D	50D
St	0.198	0.196	0.195	0.195
$C_{D,mean}$	1.146	1.122	1.112	1.112
$C_{D,amplitude}$	0.222	0.217	0.216	0.216
$C_{L,mean}$	2.528	2.500	2.489	2.489
$C_{L,amplitude}$	0.743	0.714	0.710	0.710

Table 1: Strouhal number and lift and drag characteristics for several domain widths. An additional plot can be found in appendix C.

Domain width	20D	30D	40D
St	+1.54%	+0.51%	0.00%
$C_{D,mean}$	+3.06%	+0.90%	0.00%
$C_{D,amplitude}$	+2.78%	+0.46%	0.00%
$C_{L,mean}$	+1.57%	+0.44%	0.00%
$C_{L,amplitude}$	+4.65%	+0.57%	0.00%

Table 2: Relative differences between the values compared to the domain with width 50D.

with D being the diameter of the cylinder. The results of the other three meshes are nearly exactly the same. From this it is concluded that a domain width of $30D$ is sufficient to prevent any interference from the boundary.

Wake Length

In a similar way to the boundary distance, the influence of the length of the wake is assessed. A benchmark numerical simulation performed by Engelman and Jamnia [10] for a Von Karman vortex street showed that an insufficient wake length will greatly influence the characteristics of the flow, yielding, among other things, drag values and Stouhal numbers that deviate considerable from the values obtained from a fully developed wake. Table 3 shows the result for four meshes with different domain lengths. The distance from the inflow to the cylinder is kept constant, meaning only the length of the wake is varied. Apparently, even the shortest wake length has negligible differences with the longest. However, when comparing the visuals in figure 14, sufficient length is needed to see a fully developed wake, which will be the case when using a domain with a length of at least $55D$.

4.2.3 *Sensitivity with respect to the timestep*

The next numerical parameter that is discussed, is the preferred CFL number, which is used as a measure of the timestep with respect to the grid size. As numerical stability is not an issue, the CFL number is only indicative for the accuracy of the solution. To gain insight into this matter, the same mesh is used (thus retaining the Δx term) with

Domain length	35D	45D	55D	65D
St	0.196	0.196	0.196	0.196
$C_{D,mean}$	1.121	1.122	1.122	1.122
$C_{D,amplitude}$	0.217	0.217	0.217	0.217
$C_{L,mean}$	2.499	2.500	2.500	2.500
$C_{L,amplitude}$	0.717	0.718	0.718	0.718

Table 3: Strouhal number and lift and drag characteristics for several domain lengths. An additional plot can be found in appendix C.

varying time steps. The visual results can be observed in figure 14 for CFL numbers 0.37, 1.48, 3.69, 7.39 and 14.77.

Remarkably, even very high CFL numbers still yield acceptable results. Only the simulation with CFL number 14.77 leads to unreliable results. When comparing the lift and drag values and the Strouhal number in figure 15, the same trend can be observed as with the visuals.

From these results, a target CFL number of 3.5 is chosen, with a maximum at 4.0. This is deemed sufficient to provide accurate and precise results, while keeping the computational costs at a minimum. Through all simulations, the CFL number is kept more or less constant and the timestep is varied. This is needed because at higher spin rates, the maximum velocity increases, yielding higher CFL numbers if the timestep is not adjusted. The timestep has an inverse linear relation to the spin rate:

$$\Delta t \sim \frac{1}{\alpha} \quad (37)$$

For $\alpha < 1.0$, the timestep will be the same as $\alpha = 1.0$.

4.3 MESH CONVERGENCE STUDY

A mesh convergence study is performed to verify that the grid size of the mesh is sufficient for the problem at hand. The original mesh is both coarsened and refined, while the distributions of the knots of all knotvectors are kept the same. The time step is adjusted according to the grid size, yielding the same target CFL number of 0.90 for all simulations. 4 gives an overview of the different meshes that are used for this convergence study. The lift and drag values for the cylinder obtained from the simulations are plotted in 16. For the coarsest grids, M1 and M2, the results can easily be distinguished from the rest, indicating insufficient convergence when looking at the deviating lift and drag values and Strouhal numbers. From M3, the results are already nearly identical to the finest mesh, M8, with an error lower than 3%.

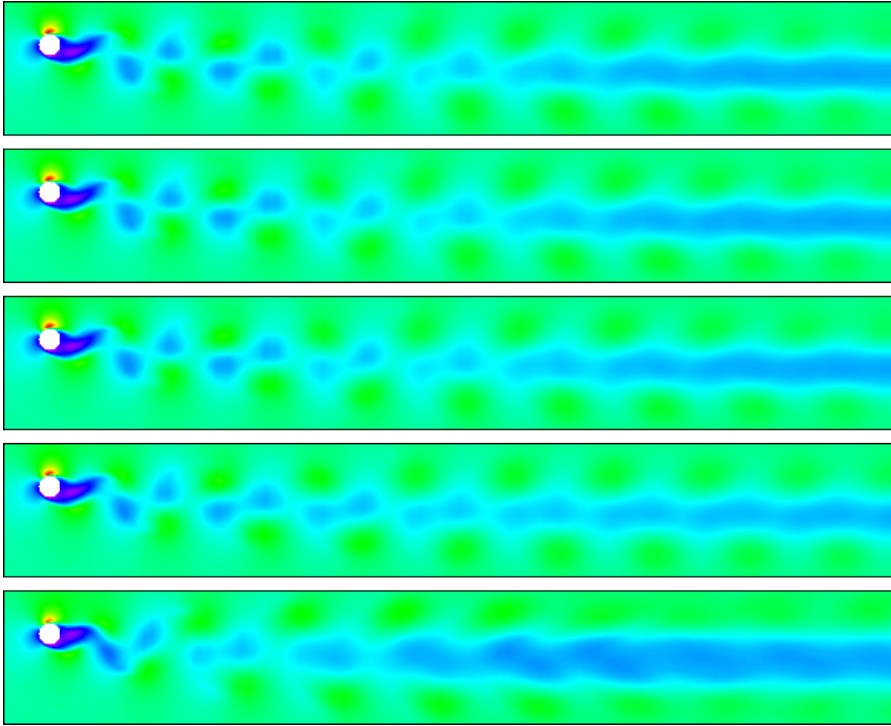


Figure 14: Visual representation of u for CFL numbers of respectively 0.37, 1.48, 3.69, 7.39 and 14.77 (from top to bottom)

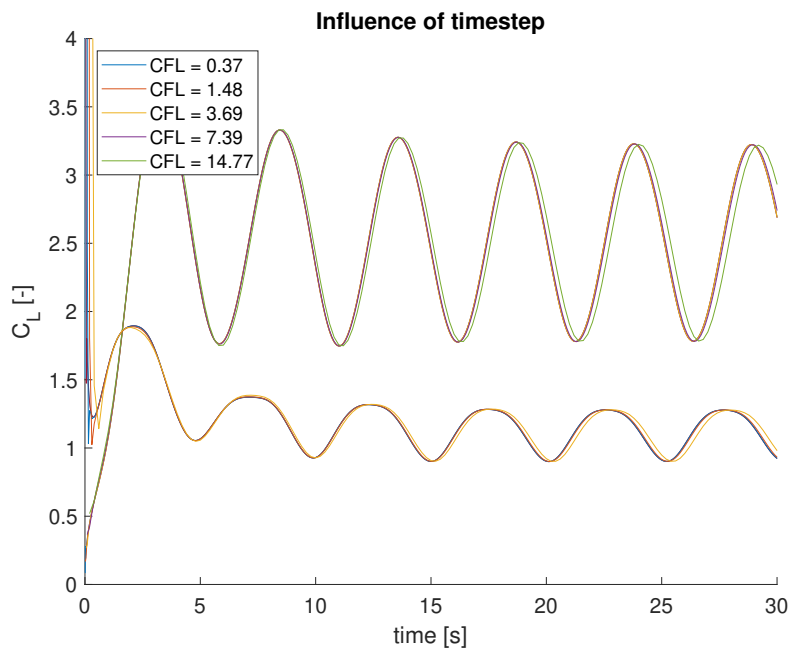


Figure 15: C_L (upper curves) and C_D (lower curves) for several CFL numbers.

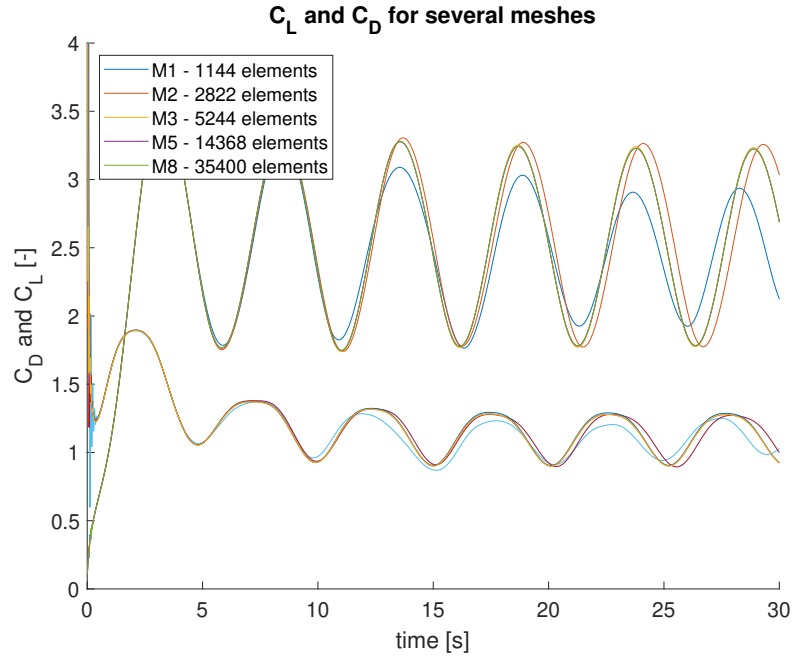


Figure 16: C_L and C_D for meshes M1, M2, M3, M5, M8

	# elements	Δt	CFL
M1	1144	0.04000	0.79
M2	2822	0.02667	0.84
M3	5244	0.02000	0.88
M4	8410	0.01600	0.90
M5	14368	0.01333	0.90
M6	16974	0.01143	0.90
M7	22372	0.01000	0.92
M8	35400	0.00800	0.93

Table 4: Table of the meshes sizes used for the mesh convergence study

Figure 17 shows a visualisation for velocity in x -direction, u . Meshes M3 and M4 are too coarse to represent the wake correctly. From M5, the wake seems to be converged as it cannot be visually distinguished from M6 and the two finest meshes. As such, M5 will be used further on. The final two-dimensional meshes are depicted in figures 19 and 20.

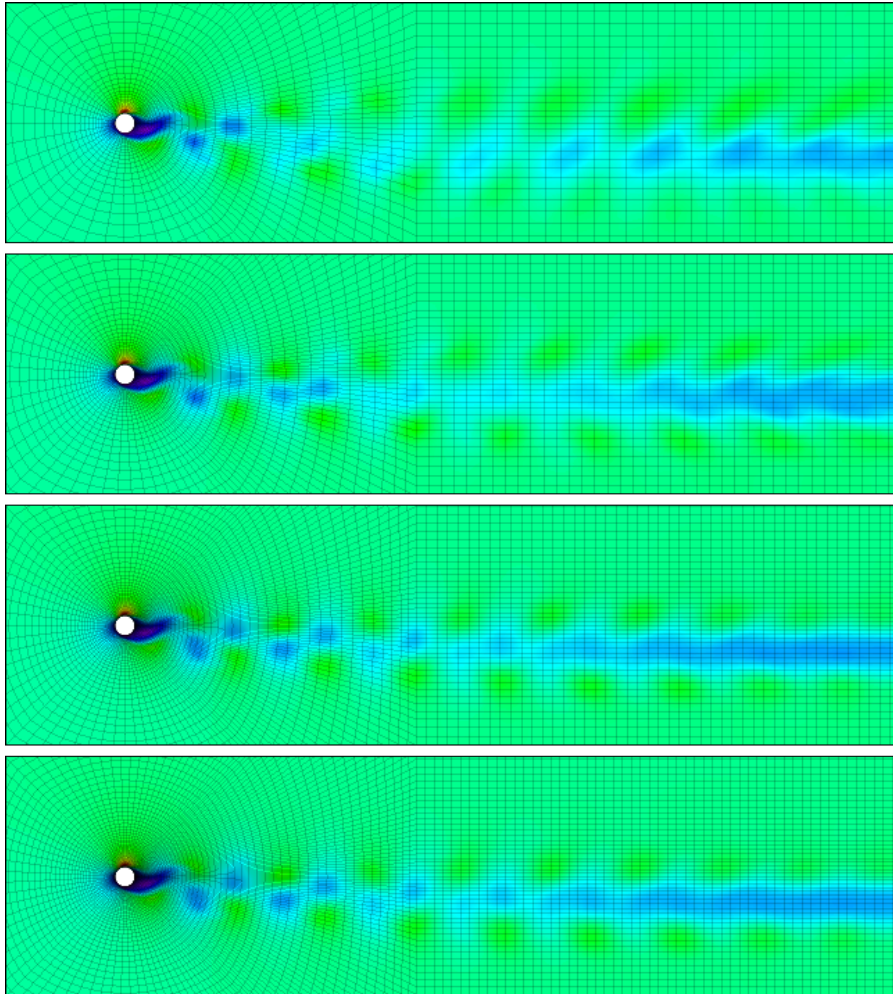


Figure 17: Visual representation of u for respectively M_3 , M_4 , M_5 and M_6 (from top to bottom)

4.3.1 Validation of the set-up

To validate the current numerical setup, results are compared with previous experiments. Physical data is retrieved from Norberg [19] and Tritton [25] and numerical data from Braza, Chassaing, and Minh [2], Park, Kwon, and Choi [20], Engelman and Jamnia [10], Singha and Sinhamahapatra [24] and Dennis and Chang [8]. An overview is given in table 5. Literature shows some variations for the different parameters, especially for the drag. A comparison shows that in general, all values from the current setup fall well within the range and are in good agreement with the available experimental data.

Source	Re	St	\hat{C}_L	\bar{C}_D	Type
Braza[2]	100	0.160			Numerical
Park[20]	100	0.166		1.33	Numerical
Engelman[10]	100	0.173	0.363	1.41	Numerical
Singha[24]	100	0.165		1.42	Numerical
Dennis[8]				1.06	Numerical
Tritton[25]	100			1.25	Experimental
Norberg[19]	100	0.168			Experimental
Current	100	0.167	0.325	1.36	Numerical
Mittal[17]	200		0.73	1.41	
Singha[24]	200	0.190		1.43	Numerical
Norberg[19]	200	0.182			Experimental
Current	200	0.198	0.71	1.36	Numerical
Park[20]	50			1.45	Numerical
Singha[24]	45			1.60	Numerical
Tritton[25]	50			1.42	Experimental
Current	50			1.43	Numerical

Table 5: Overview of several parameters: Strouhal number, amplitude of lift and the mean drag.

Next, visuals at Reynolds number 200 and $\alpha = 1.0$ are compared with experimental results from Coutanceau and M enard [7]. Figure 18 shows a snapshot from real flow set against a visualisation of the present work at approximately the same time slot. Both visualisations show a vortex that is shed behind the cylinder and the wake with deflected streamlines and a good agreement is seen.

Lastly, average values for the lift coefficient at Reynolds number 200 are compared with the results from Mittal and Kumar [17] for several Reynolds numbers, shown in table 6. Mittal and Kumar [17]'s results were furthermore in excellent agreement with 2D DNS. The differences with the current setup are very slight.

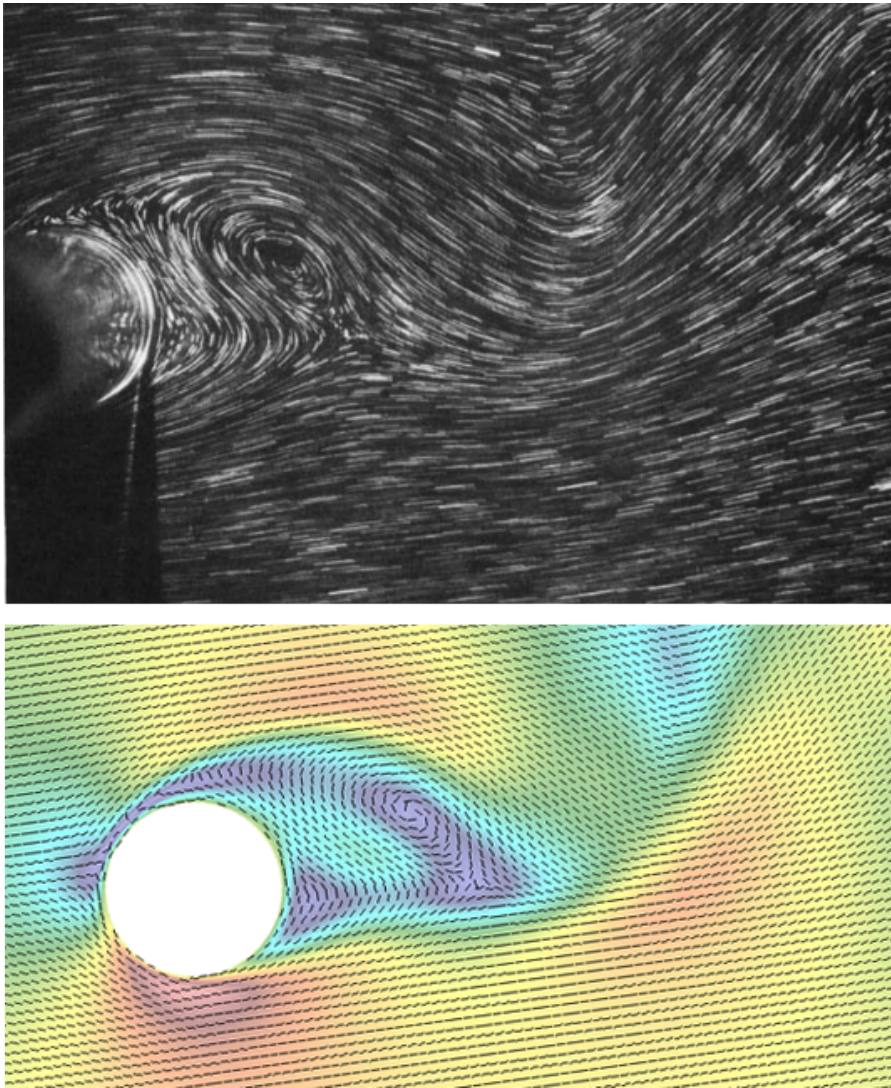


Figure 18: Visualisations of the flow at $Re = 200$ and $\alpha = 1.0$. Above: real flow from Coutanceau and Ménard [7]. Below: present result with velocity vectors.

α	Mittal and Kumar [17]	Current
0.0	0.00	0.00
0.5	1.20	1.23
1.0	2.53	2.52
1.5	3.90	3.92
2.0		5.40
2.5	7.65	7.65
3.0	10.30	10.36
3.5	13.55	13.68
4.0	17.60	17.59
4.5		22.45
5.0	27.40	27.28

Table 6: Comparison between present results with the results from Mittal and Kumar [17] at Reynolds number 200 for various spin rates.

4.4 THREE-DIMENSIONAL MESH

To obtain the three-dimensional mesh, a two-dimensional mesh is extruded alongside a vertical z -axis. Due to limits on the available computational power, extruding the M_5 -mesh was not an option; compromises had to be made. Firstly, the focus lies on the near-cylinder physics and the wake is seen as less important, as such patch #5 is severely reduced so the new domain length will be $35D$. Table 3 showed that the length of the wake is of negligible influence when considering the flow near the cylinder. It should be noted that the wake shown in the results might not be fully developed.

Next, a slightly coarsened 2D mesh between M_4 and M_5 , containing around 8000 elements, is used as the basis for the extrusion. Earlier on, it was noticed that between M_4 and M_5 , the difference could be spotted in the wake, at a long distance from the cylinder. The mesh is still very fine close to the cylinder, which will yield accurate results.

As for the height, an aspect ratio of 5 is chosen with respect to the diameter of the cylinder. This aspect ratio is sufficiently large to ensure that three-dimensional effects are encapsulated. The final mesh contains about 160000 elements. Results will be compared to those of Mittal [16].

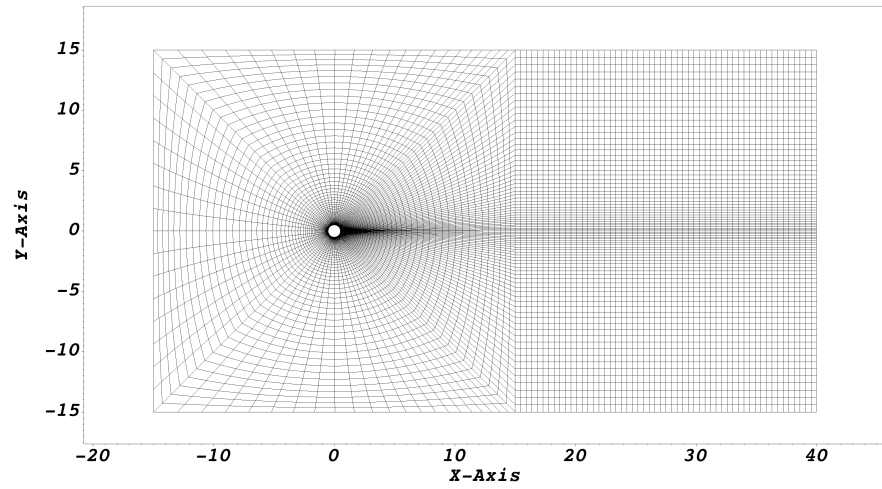


Figure 19: Two-dimensional mesh. An enlargement can be found in appendix C.

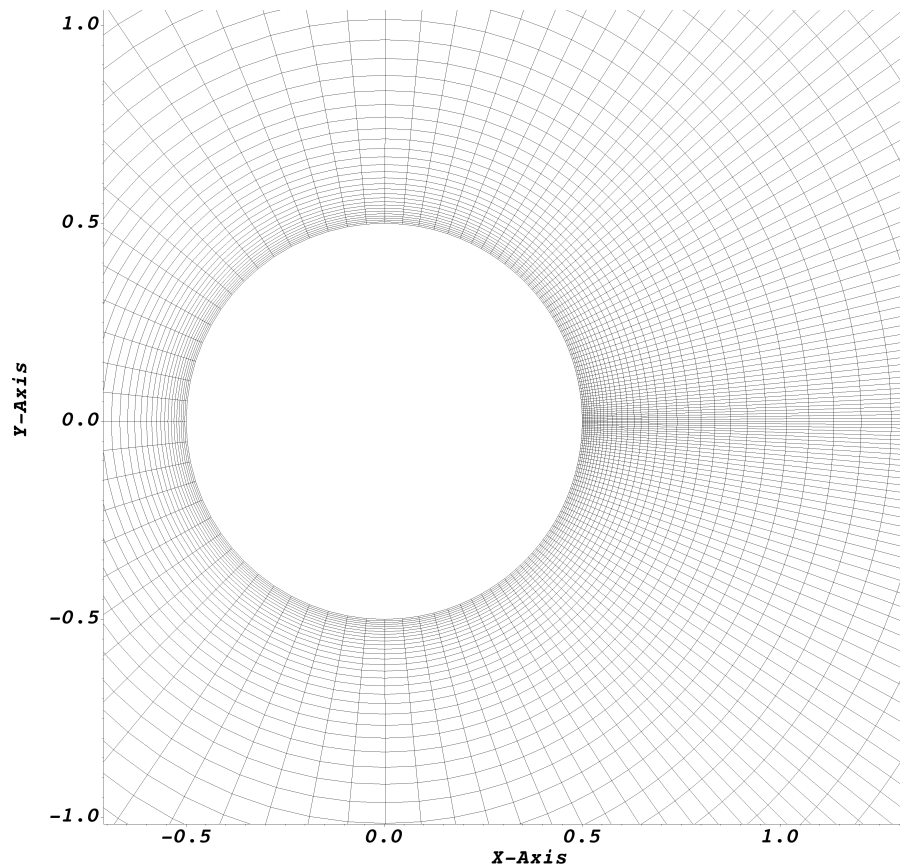


Figure 20: Close-up of the area around the cylinder showing the extra refinement to model the rotary boundary layer correctly. The inner part of this boundary layer contains ten elements.

RESULTS AND ANALYSIS

This chapter covers the results that are obtained from the numerical experiment using the methods from 3 and the set-up from chapter 4. Results are presented as concise as possible, several additional plots and figures are included in the appendix D. Outcomes that are not related to the research questions are not included.

5.1 2D RESULTS FOR REYNOLDS NUMBER 200

For the various spin rates, different flow regimes can be distinguished, plots for the lift and the drag coefficients are included in figures 21 and 22 to illustrate this. At $\alpha = 0.0$, a Von Karman vortex street is expected and is indeed observed from $t = 100$ s. It does take a lot of time until the steady-state is achieved due to the symmetrical mesh and initial conditions. When increasing the spin rate, the vortex street is deflected downward and lift increases gradually. The shedding frequency barely changes. The asymmetry in the flow created by the rotating cylinder results in a very swift convergence to a steady state, already achieved at $t = 20$ s.

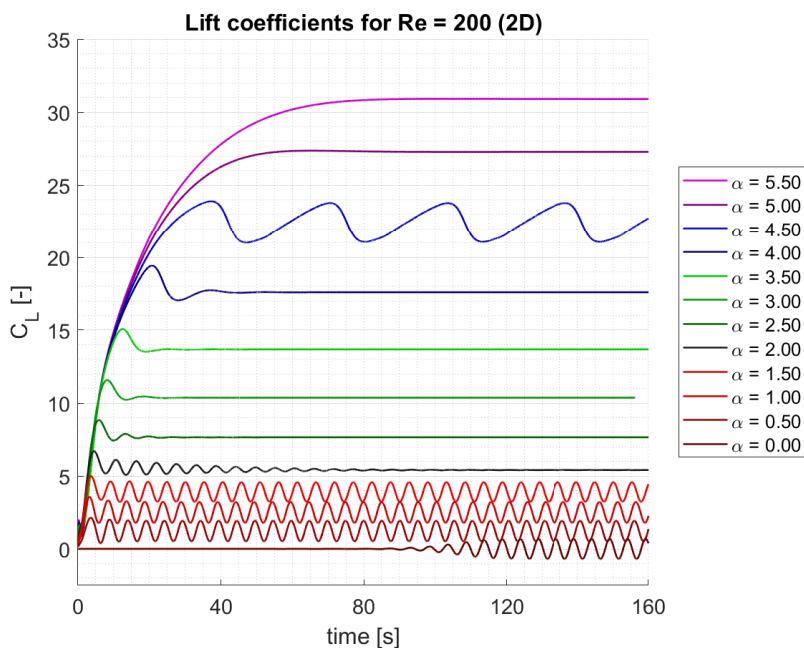


Figure 21: Lift coefficient for $Re = 200$ for the 2D simulation for various spin rates.

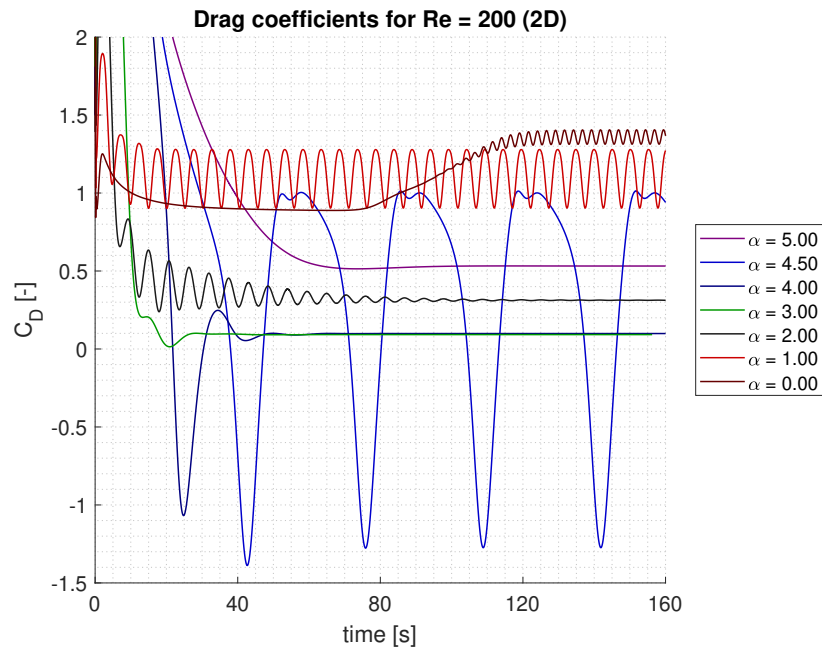


Figure 22: Drag coefficient for $Re = 200$ for the 2D simulation for various spin rates.

At $\alpha \approx 2.00$, vortex shedding starts to stop and the periodic behaviour comes to an end. As with the case of $\alpha = 0.0$, it takes a vast amount of time to reach the final steady state. At $t = 100s$, almost no periodic behaviour is seen. However, a slight periodic deviation from the mean value is still observed until the end time of the simulation at $t = 200s$. Clearly, the case of $\alpha = 2.00$ is on the borderline between two flow regimes. Mittal and Kumar [17] showed already with a linear stability analysis that the critical spin rate is at $\alpha = 1.91$.

At higher spin rates, for $\alpha > 2.0$ up until somewhere between $\alpha = 4.0$ and $\alpha = 4.5$, vortex shedding ceases and a stable solution is obtained. At $\alpha = 4.5$, one-sided vortex shedding re-envelops at the pressure side of the cylinder at a low frequency. Mittal and Kumar [17] proposed this is due to the build up of vorticity in the rotary boundary layer, becoming strong enough at a certain point to create a vortex that leaves the boundary layer and is shed. As for the drag, a remarkable result should be noticed. Where as the drag for all other cases is positive, the drag coefficient at $\alpha = 4.5$ oscillates with a very large amplitude and becomes highly negative, which can also be called thrust. However, opposed to the results from Mittal and Kumar, the net drag is negative, albeit slightly. Where as the results from Mittal and Kumar showed that a net negative drag was obtained for several high spin rates, the net drag in these simulations never drops below zero. As for the lift, results are nearly identical for the lift and drag coefficients, as well as the Strouhal number.

For spin rates for $\alpha \geq 5.0$, the periodic behaviour fades again and no vortex shedding is observed for higher spin rates. However, a 3D simulation from Mittal [16] showed that, contrary to the 2D simula-

tions, the flow is highly instable and strong three dimensional effects are observed. This raises some serious questions about the validity of 2D simulations. There are no further studies, known by the author, about the three dimensional effects at lower spin rates, meaning that there is a possibility that three dimensional effects kick in at lower spin rates, which will be covered later on.

When looking at the visuals in figure 23, four completely different regimes can easily be distinguished. At $\alpha = 1.0$, the deflected Von Karman vortex street is observed. At $\alpha = 3.0$, a stationary vortex on the pressure side of the cylinder is formed and the rotary boundary layer is clearly recognisable. The case of $\alpha = 4.5$ shows a rotation rate that is strong enough to reduce the speed of the fluid on the pressure side nearly to zero for several diameters away from the cylinder. The bottom part of this images shows a vortex that is shed at low frequency, which was already observed in the lift and drag plots. More visuals that show the development of this vortex shedding are included in figure 62 in appendix E. $\alpha = 5.0$ looks very similar to $\alpha = 4.5$, safe the vortex shedding.

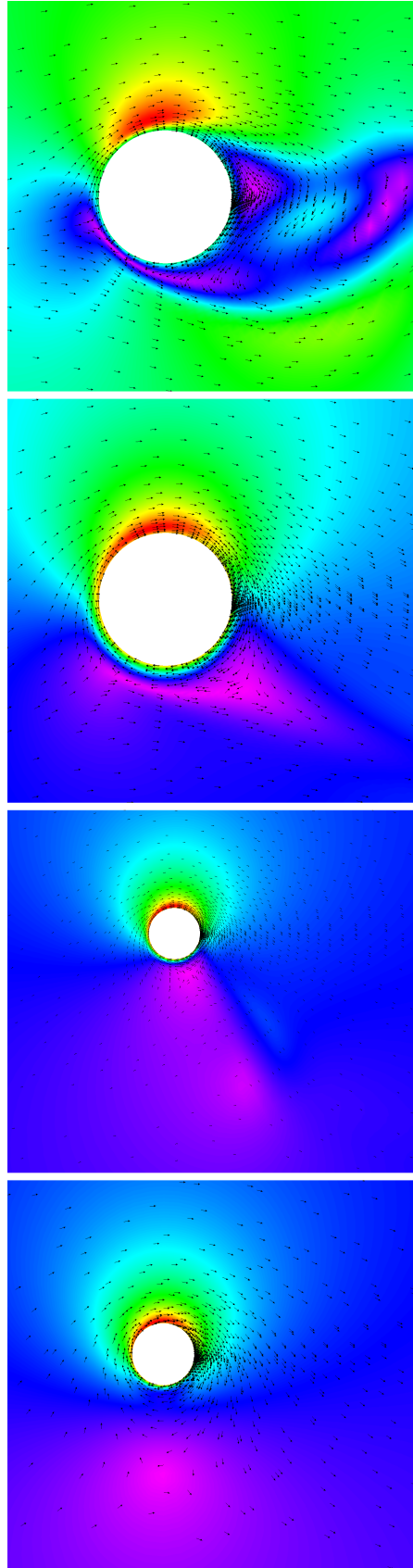


Figure 23: Velocity magnitude for Reynolds number 200 at various spin rates, from top to bottom respectively $\alpha = 1.0$, $\alpha = 3.0$, $\alpha = 4.5$ and $\alpha = 5.0$. Note that the colour scales do not match between the figures and vary from zero (purple) to the maximum velocity (red) in each plot.

5.2 2D RESULTS FOR VARYING REYNOLDS NUMBER

The simulations performed for Reynolds number 200 are expanded to several other Reynolds numbers: 50, 100, 300 and 400.

5.2.1 Reynolds number 50

Figure 24 shows the lift coefficients for a flow at Reynolds number 50. For a stationary cylinder at this stage, no vortex shedding takes place. At small spin rates of the cylinder, a Von Karman vortex street can be observed. A possible explanation can be given when considering the local Reynolds number, which is obtained when using the local velocity u instead of u_∞ . Local Reynolds numbers with about 80 as a maximum are present in the flow, which would make the flow fall within the range of Reynolds numbers where vortex shedding occurs.

The vortex shedding fades between $\alpha = 1.0$ and $\alpha = 1.5$. The conclusion from Coutanceau and M enard [7] that this critical spin rate is independent of the Reynolds number, based on experiments for Reynolds number from 200 to 1000, does not seem to hold for lower Reynolds numbers. At higher spin rates, the flow is stable, except for $\alpha = 5.5$: here, the same vortex shedding is observed as at Reynolds number 200 but occurs here at a much higher spin rate.

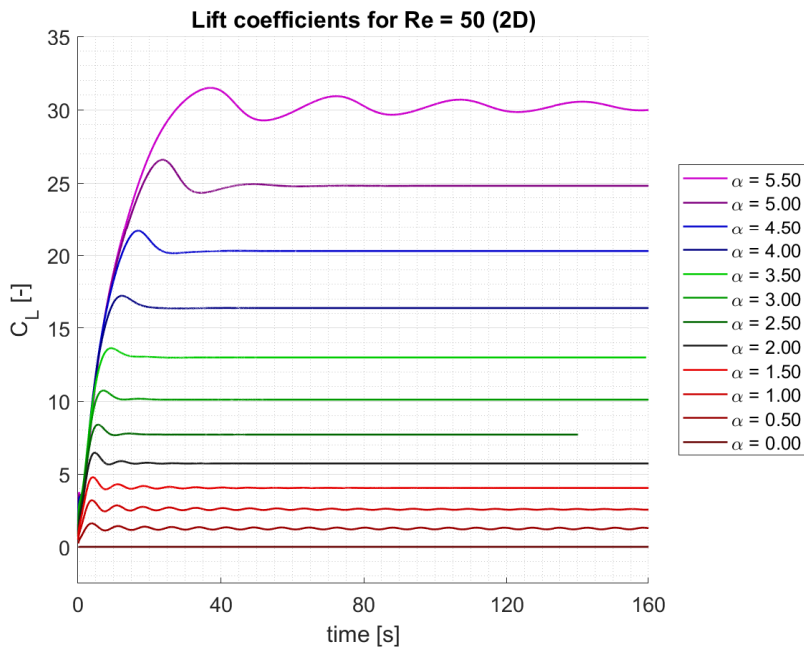


Figure 24: Lift coefficient for Re = 50 for the 2D simulation for various spin rates.

5.2.2 Reynolds numbers 100 to 400, $\alpha \leq 2.0$

The simulations for Reynolds number 100 show many similarities to those for Reynolds number 200. Lift coefficients for Reynolds num-

ber 100 are plotted in figure 25. At lower spin rates, the amplitude at Reynolds number is 50% lower and the Strouhal number is slightly smaller. For each spin rate, average lift values of the two Reynolds numbers do match up, which is to be expected as the Reynolds number has no direct influence on the calculation of the lift and coefficient.

When taking the results for Reynolds number 300 and 400 into account, it can be concluded that the Strouhal number, the amplitude of lift and drag are dependant on the Reynolds number: all values increase with the Reynolds number. The relation is non-linear and data from too few Reynolds numbers is available to propose a mathematical formulation for this relation.

For $\alpha = 2.0$, all simulations need a long simulation time to reach the steady state and for Reynolds number 400, this steady state is not even reached after 200 seconds. This confirms that this is indeed close to the critical spin rate at which the periodic vortex shedding is replaced by a steady one-sided vortex, being independent of the Reynolds number, which is also seen in the experiments from Coutanceau and M enard [7].

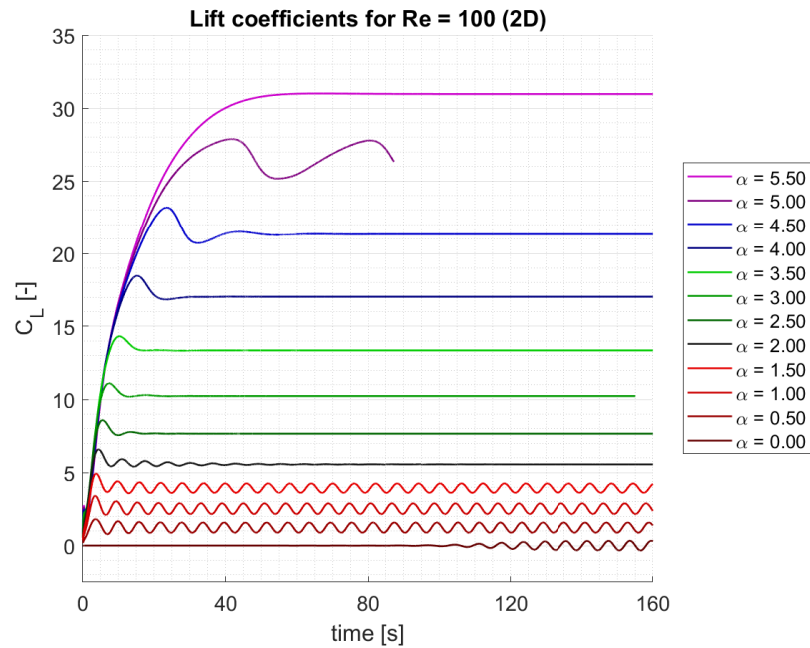


Figure 25: Lift coefficient for Re = 100 for the 2D simulation for various spin rates.

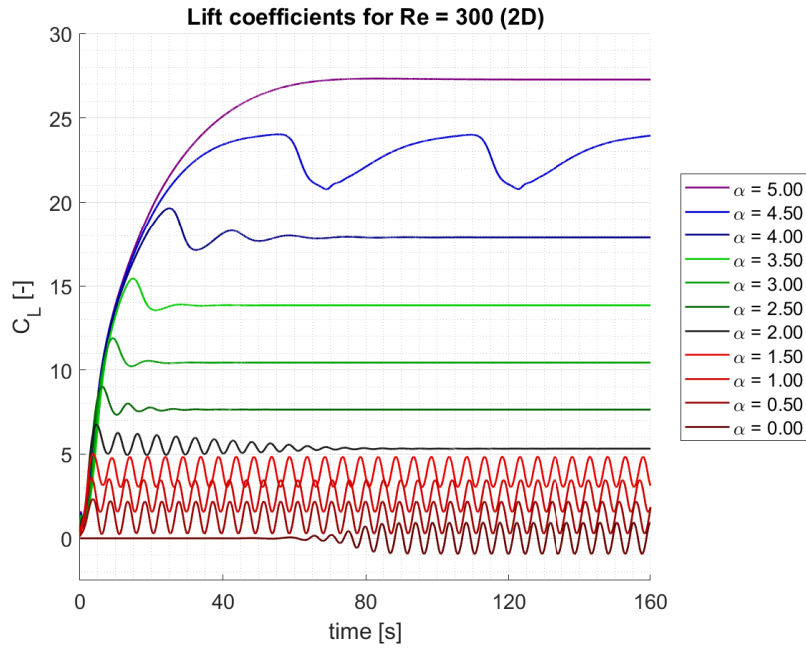


Figure 26: Lift coefficient for Re = 300 for the 2D simulation for various spin rates.

5.2.3 Second region of vortex shedding

For Reynolds number 200, in a range somewhere between $\alpha = 4.0$ and $\alpha = 5.0$, periodic vortex shedding reoccurs. The simulation for $\alpha = 4.5$ clearly shows this. The Reynolds-dependency of this second region of vortex shedding is investigated.

The shedding at $\alpha = 4.5$ is only observed at Reynolds 200 and 300 (see figure 26). At the simulated spin rates for Reynolds number 100, the second region of vortex shedding is observed at $\alpha = 5.0$. At Reynolds number 400 (see figure 27), this second region is not observed at first. However, at $\alpha = 4.0$, the steady state solution is only achieved after a very long simulation time and has the same characteristics as $\alpha = 2.0$. This could indicate that $\alpha = 4.0$ could be very close to the critical spin ratio for the second region of vortex shedding. As such, at this Reynolds number, two additional simulations were performed at $\alpha = 3.75$ and $\alpha = 4.25$. This indeed confirms that $\alpha = 4.0$ is a critical spin ratio: at $\alpha = 3.75$, no vortex shedding is observed, where as at $\alpha = 4.25$ the second region of vortex shedding emerges. Apparently, this second region of vortex shedding appears at lower spin ratio's as the Reynolds number increases for a Reynolds number of 50 up to 400.

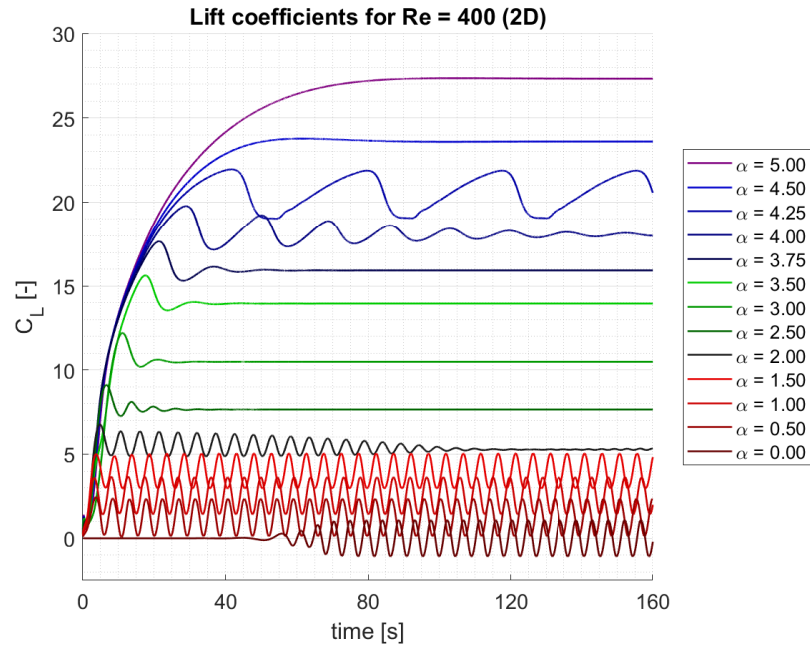


Figure 27: Lift coefficient for $Re = 400$ for the 2D simulation for various spin rates.

5.2.4 Reynolds-dependency of lift and drag

Figures 28 and 29 show respectively the lift and drag coefficient plotted over the Reynolds number. For lower spin rates ($\alpha < 3.0$), the Reynolds number has no meaningful influence on the lift coefficient and the lift increases linearly with increasing spin rate. For larger values of α , the lift seems to increase slightly faster with higher Reynolds numbers.

The drag coefficient varies more with the Reynolds number, but the same trend can be observed in all cases. Drag drastically decreases with increasing spin rate and the decrease is at it largest when approaching the first critical spin ratio for which period vortex shedding disappears. Drag is minimal for a range of $3.0 < \alpha < 3.5$, where it is very close to zero, except for the lowest Reynolds number. Thereafter, drag starts to increase once more.

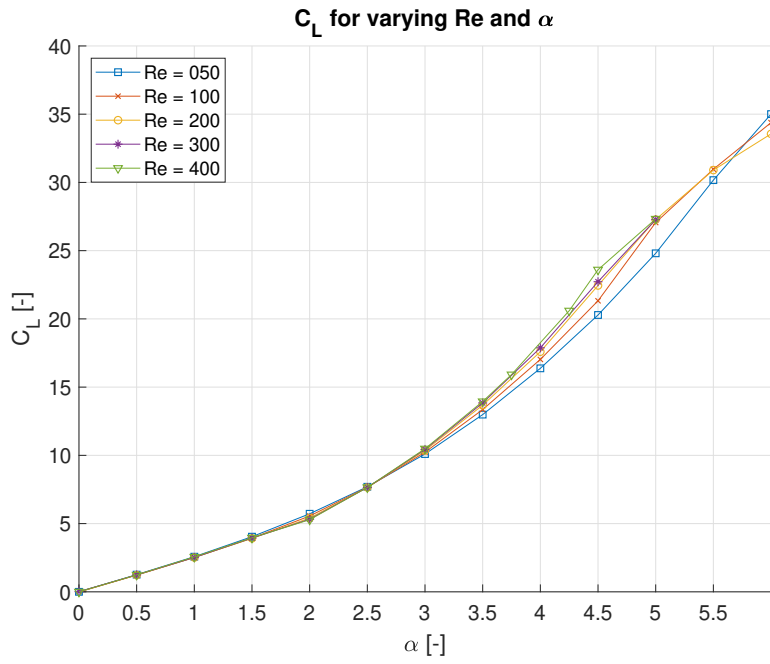


Figure 28: Mean lift coefficient for several Reynolds numbers plotted against the spin rate.

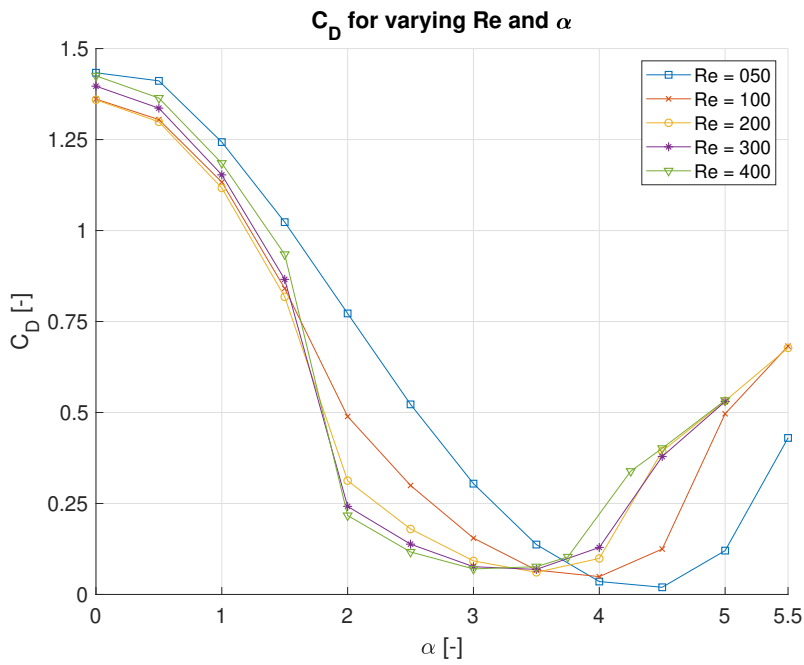


Figure 29: Mean drag coefficient for several Reynolds numbers plotted against the spin rate.

5.3 3D RESULTS

5.3.1 *High spin rates*

Three-dimensional simulations are carried out at for several spin rates at Reynolds number 200. Figures 30 and 31 give an impression for the flow (more visualisations can be found in appendix F), at spin rates $\alpha = 4.50$ and $\alpha = 5.00$, respectively. One can see clearly that the flow is highly three dimensional and that the wake on the pressure side of the cylinder is characterised by a highly instable flow. Strong vorticity is observed in both the wake as on the surface of the cylinder, where banding occurs. The difference between the two spin rates is visible: with increasing spin rates, vorticity also builds up.

A big difference is observed around $\alpha = 4.50$. The 2D simulations show a completely different characterisation of the flow compared to $\alpha = 4.00$ and $\alpha = 5.00$ due to the period vortex shedding. This phenomenon is not observed in 3D.

When compared the 3D simulations to those in 2D, poor agreement is observed. Although the vortex shedding for $\alpha = 4.50$ in the 2D case reappears in 3D, the shedding is much more irregular and of a different form.

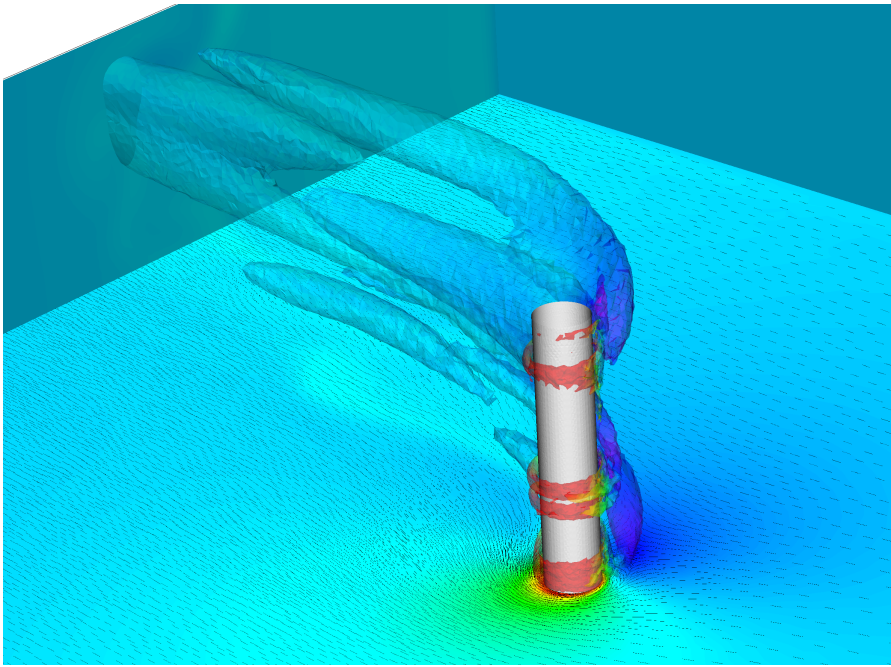


Figure 30: Visuals of the three-dimensional flow for $Re = 200$ and $\alpha = 4.50$ at $t = 60.0s$. The colours represent the magnitude of the local velocity vector.

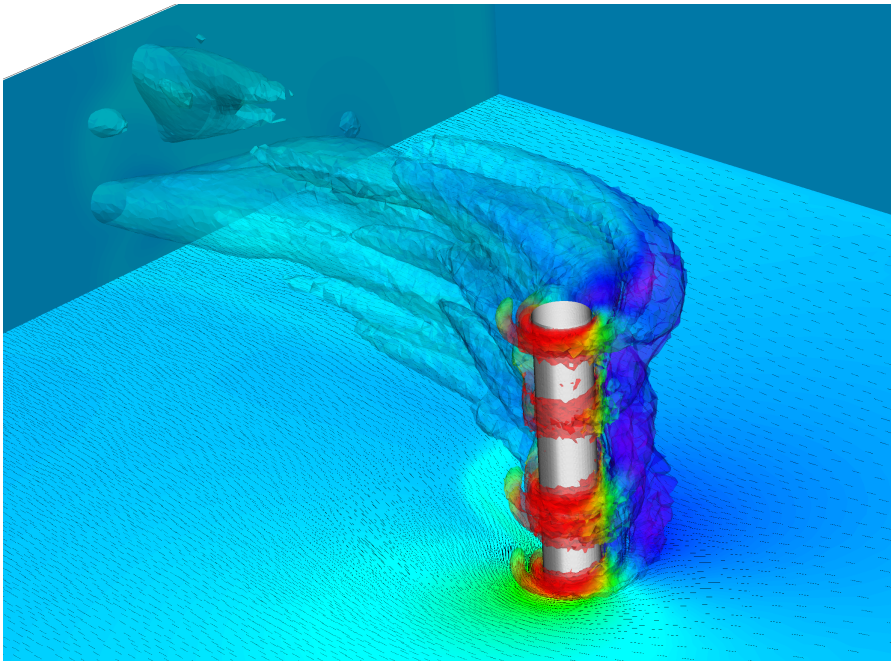


Figure 31: Visuals of the three-dimensional flow for $Re = 200$ and $\alpha = 5.00$ at $t = 60.0s$. The colours represent the magnitude of the local velocity vector.

5.3.2 *Low spin rates*

When also considering the lower spin rates, a transition between a fully two-dimensional flow to a three-dimensional can be observed with increasing spin rates. The upper image in figure 32 with $\alpha = 1.0$ does not contain any notable vertical velocities, where as some slight banding starts to become visible in the lower image at $\alpha = 3.0$.

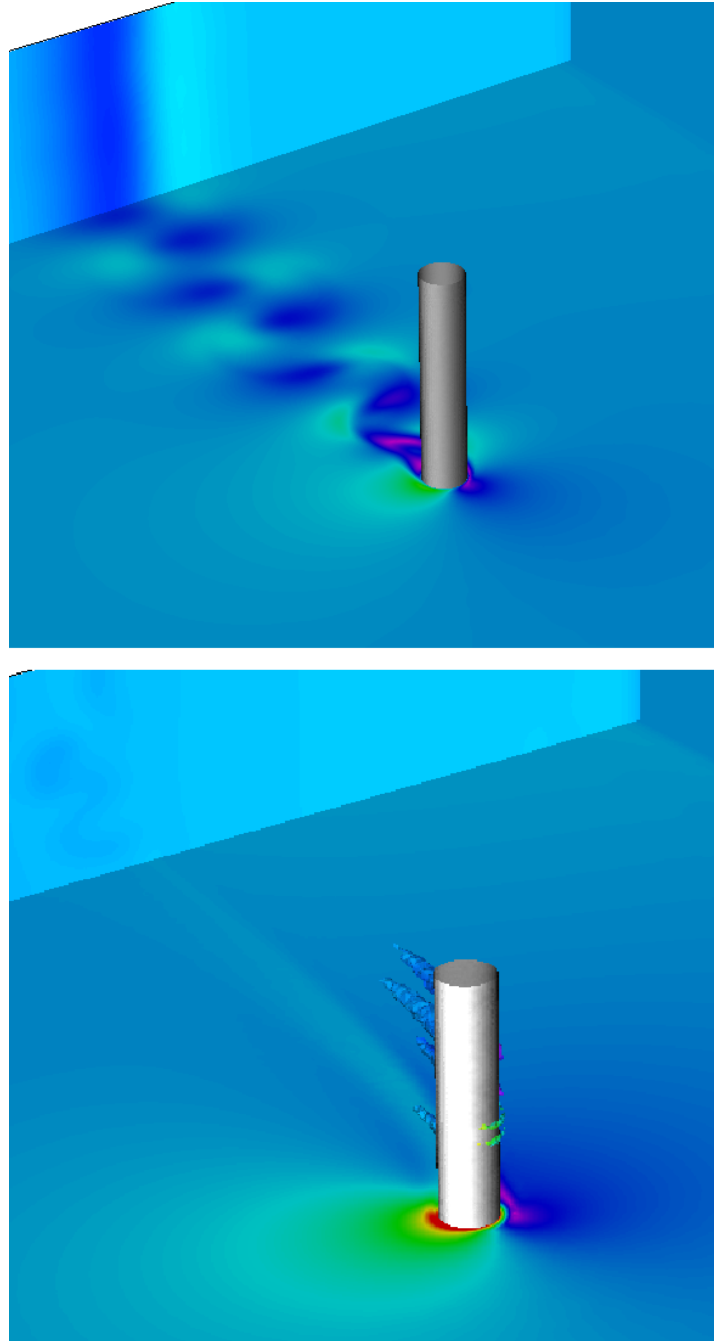


Figure 32: Visuals of the three-dimensional flow for $Re = 200$ at spin rates $\alpha = 1.0$ and $\alpha = 3.0$. The colours represent the magnitude of the local velocity vector.

5.3.3 Comparison between 2D and 3D

Coefficients for lift and drag are now compared between the 2D and the 3D simulations. For the lift, presented in figure 33, in all cases, the values from the 3D simulations tend to be lower than the 2D values. Where at $\alpha = 1.0$ the averages for the lift coefficient are in fair agreement with only a difference of 5%. At $\alpha = 2.0$, this difference is increased up to 10% and the relative gap between 2D and 3D becomes even bigger with increasing spin rates, maxing out at 25% at a spin rate of $\alpha = 5.0$.

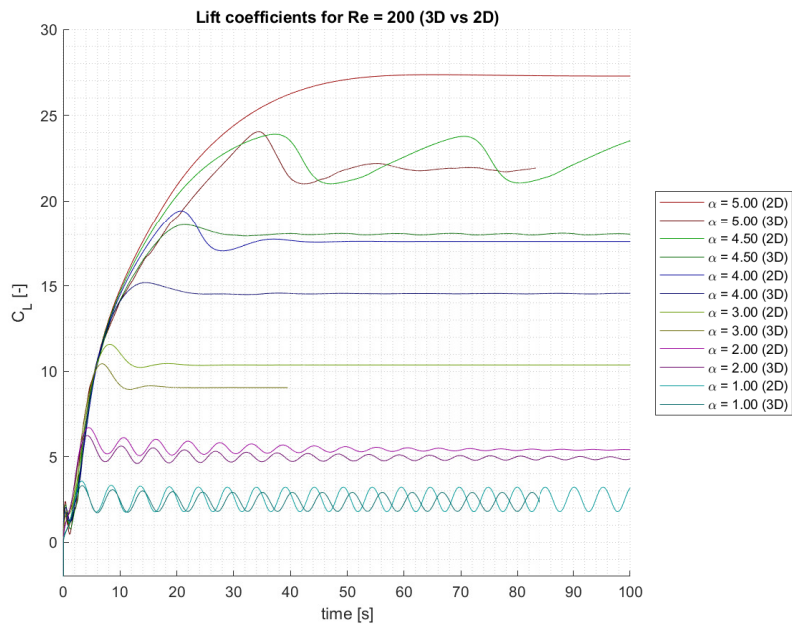


Figure 33: Comparison of the lift and drag values for several spin rates at Reynolds number 200 for the 2D and the 3D simulations.

As for the drag coefficient, figure 34 shows that the trend for the drag discussed in paragraph 5.2.4 comes back when looking at the 3D results. The rapid decrease with increasing spin rates up until $\alpha = 3.0$ remains and increases for the highest spin rates. This confirms that around $\alpha = 3.0$, the mean drag is minimal and the aerodynamic efficiency is at its peak.

When looking at the behaviour of the drag over time in figures 36 and 35, a difference has to be made by the lower spin rates, $\alpha \leq 3.0$ and the higher spin rates, $\alpha > 3.0$. For lower spin rates, the behaviour of the drag curve is quite similar in 2D and 3D. The same periodic characteristics are observed at $\alpha = 2.0$ and $\alpha = 1.0$, although not agreeing completely. For higher spin rates, the drag curves for 2D and 3D do not match. It should also be noted that in the 3D case, the drag never gets negative.

As the upper boundary essentially serves as an end plate, the values obtained for lift and drag should be seen as respectively maximum and minimum values for this aspect ratio. After all, removing the

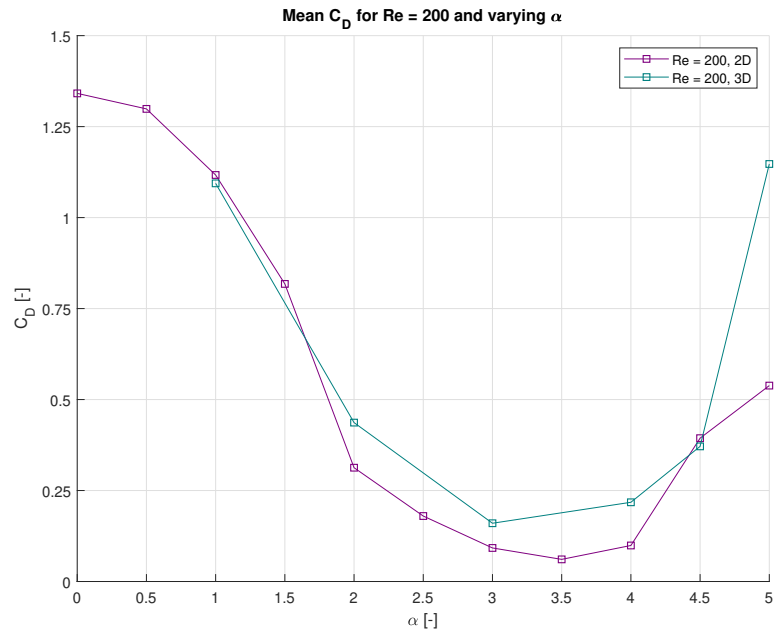


Figure 34: Development of the drag coefficient at Reynolds number 200 for varying spin rates in 2D and 3D.

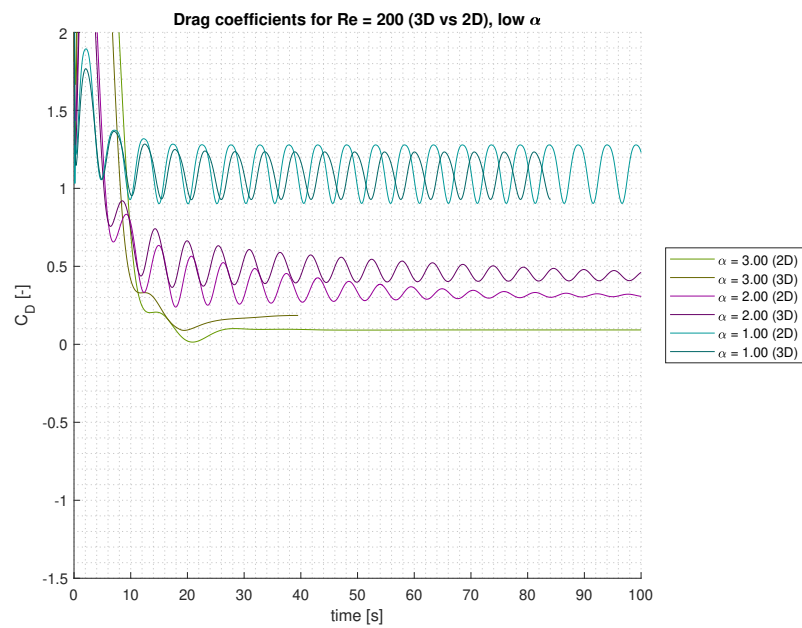


Figure 35: Drag coefficient plotted over time for low spin rates ($\alpha \leq 3.0$).

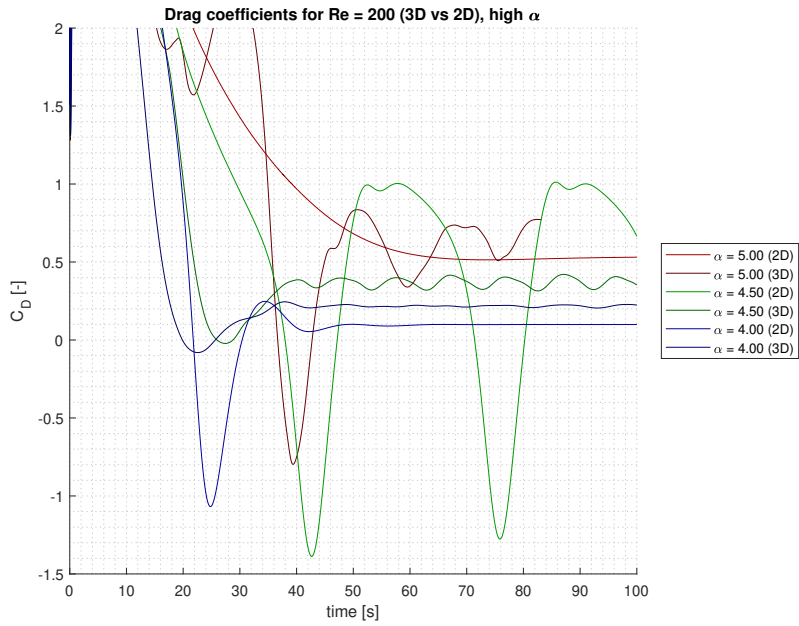


Figure 36: Drag coefficient plotted over time for high spin rates ($\alpha > 3.0$).

end plates would provide additional induced drag resulting in both a decreased lift and an increased drag.

5.3.4 *Aerodynamic efficiency and torque*

Figure 37 shows the aerodynamic efficiency, defined as the ratio between lift and drag, plotted for several Reynolds numbers in 2D and for Reynolds number 200 in 3D. All simulations give the same trend: the maximum efficiency is obtained around $\alpha = 3.0$ and $\alpha = 4.0$. The difference between the 2D and 3D simulations becomes clear again: due to the higher drag and lower lift values in 3D, the aerodynamic efficiency is significantly lower. Due to the drag coefficient being very close to zero for the 2D results, L/D is very sensitive to the drag. Also in 3D, highest efficiency is obtained at higher spin rates, declining after $\alpha = 4.0$. To relate the aerodynamic efficiency to the power that is required to spin the cylinder, the torque coefficient is calculated for several spin rates at Reynolds number 200. The mean torque is plotted in figure 38. As spin rate increases, so does the required amount of torque and the rate of the increment.

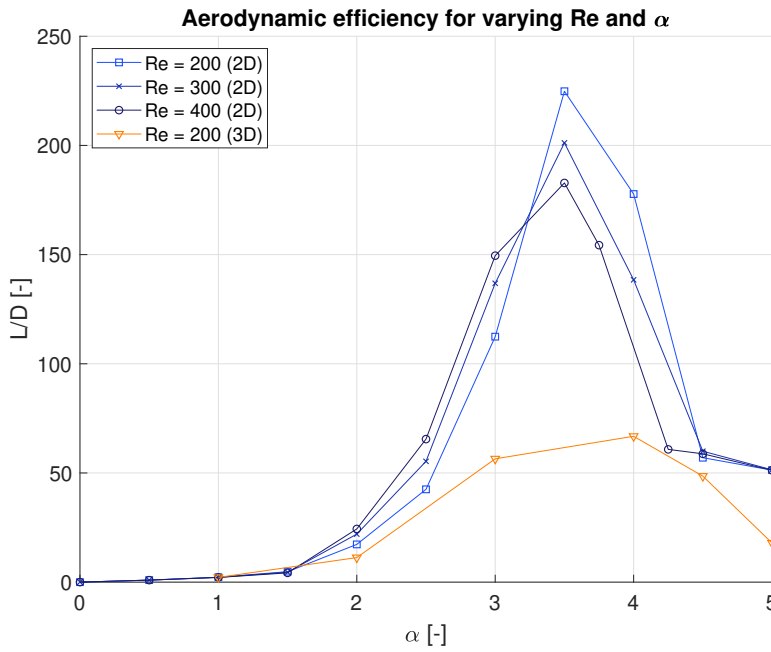


Figure 37: Mean aerodynamic efficiency for several Reynolds numbers plotted against the spin rate.

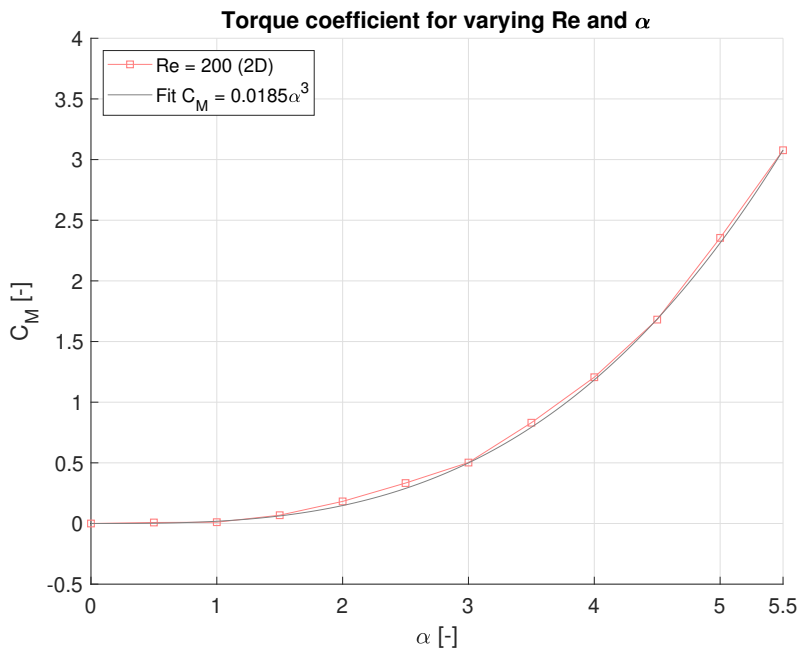


Figure 38: Mean torque coefficient plotted against the spin rate for Reynolds number 200.

CONCLUSIONS AND RECOMMENDATIONS

6.1 SECOND REGION OF INSTABILITY

At high spin rates, a second region of instability is observed. In this region, vortices are periodically shed from the cylinder. The spin rate at which this phenomenon occurs, varies with the Reynolds numbers, being lower for higher Reynolds number. The explanation given by Mittal and Kumar [17] that a strong enough build up of vorticity is needed to allow vortex shedding, is back-upped by these results: as the Reynolds numbers get lower, higher spin rates are required to compensate for this. The 3D simulation do show the second region of instability, but the transition is not as abrupt as in 2D. Instead, three-dimensional effects kick-in gradually as the spin rate increases.

6.2 VALIDITY OF 2D SIMULATIONS

Visuals show a fully two-dimensional flow at $\alpha = 1.0$ and a fully three-dimensional flow at $\alpha = 5.0$. The latter is characterised by strong, irregular vortex shedding. This transition is also seen when plotting the lift coefficient for the several spin rates. At the lower spin rates, 3D results show a good agreement with the 2D results. At higher spin rates, the curves divert strongly.

When comparing the results with Mittal [16], the mean lift at $\alpha = 5.0$ corresponds to the simulation with the same aspect ratio and slip walls. The lift calculated by Mittal has a more irregular shape, where as the current simulation provides a more regular pattern, this could be due to the dampening of the high frequencies with the Generalised- α time integration method.

For the stationary cylinder, it is known that the flow becomes more three-dimensional between Reynolds number 400 and 1000. The current numerical experiment shows that three-dimensionality of the flow also increases with the spin rate, which is logical, as a higher spin rate implies higher velocities in the flow, yielding higher local Reynolds numbers. At Reynolds number 200, the transition is around $\alpha = 3.0$. It is proposed that this transition-value lowers with increasing Reynolds number and increases with lower Reynolds number. Another indication that supports this proposition is the second region of instability observed in the 2D simulations: this phenomenon also occurs at lower spin rates as the Reynolds number increases.

As 2D simulations are always used as a representative of a three-dimensional, realistic fluid flow, it has to be concluded that 2D sim-

ulations fail to do this for spin rates (far) above the transition-value of $\alpha > 3.0$. Whereas the 3D simulations are much closer to reality, these results are deemed more accurate to real flow. Increasing the spin rate leads to major three-dimensional effects, both visually as when looking at the lift and drag coefficients. The second region of instability does not occur in the way it does in 2D simulations. At high spin rates, vortex shedding is stronger and more irregular. For approximately $\alpha < 3.0$, 2D simulations give reasonable results which are physically much closer to the 3D simulations. Coefficients for lift and drag are still off however: drag is generally higher and lift lower in the 3D case. It is observed that the three-dimensional instabilities cause the flow on the suction side to separate quicker from the cylinder than in the two-dimensional case. It is proposed that this early separation is the reason behind the higher drag and lower lift values, as the same trend is seen when considering flow separation on regular airfoils.

6.3 NEGATIVE DRAG

In the 2D simulations, the drag force becomes negative in the second region of vortex shedding for a portion of its period. The net drag never drops below zero at any spin rate, contrary to the results from Mittal and Kumar [17]. Drag approaches zero at high spin rates, opening the possibility that this parameter is highly sensitive for errors. As it is questionable whether the 2D simulations at these spin rates are representative at all for real flow, it is concluded that it is very unlikely that this phenomenon will occur with only a single cylinder. In general, drag values are higher in 3D simulations. As the current boundary conditions at the top and the bottom mimic an infinite end plate, induced drag is not taken into account and the obtained values for drag can be seen as minimum values.

6.4 EFFICIENCY OF THE SYSTEM

Both 2D and 3D simulations show the same trend with respect to the evolution of lift and drag coefficients. Lift increases linearly with the spin rate, although a slight discontinuity is observed around $\alpha = 3.0$. There is no mathematical expression available that relates the drag coefficient and the spin rate, however all simulations show that they are strongly correlated.

The highest aerodynamic efficiency is obtained in the range of $3.0 \leq \alpha \leq 4.0$, with the side note that the sensitivity to the drag coefficient is high. Above this range, the lift over drag ratio decreases and the required torque increases rapidly. From these results, it seems that a sweet spot can be found around $3.0 \leq \alpha \leq 4.0$. Higher spin rates are only interesting for maximising lift, but not in terms of the total efficiency of the system.

6.5 RECOMMENDATIONS

6.5.1 *Mesh optimisation*

Mesh optimisation was performed on the basis of $\alpha = 1.0$. The domain width was chosen such that the boundary conditions on the sides had negligible influence on the fluid flow. At $\alpha = 5.0$, a far greater area was affected by the high velocity of the cylinder than anticipated. This can be seen alongside the cylinder and in the wake in figure 31. Thus, it cannot be said that the boundaries at the sides have no interference with the fluid flow. $\frac{du}{dy}$ is still sufficiently small to conclude that any possible interference is minor or negligible. For future work, it is proposed to choose the domain width carefully to accommodate for the large area of influence for high spin rates.

6.5.2 *Scalability*

An interesting question from an engineering standpoint is whether conclusions based on low Reynolds numbers can be expanded or extrapolated to higher Reynolds numbers. As the current experiment is performed in a transition region, no clear conclusions can be drawn. The results from Reynolds number 50 seem slightly different compared to the other Reynolds numbers, which could indicate that, also in the case of the rotating cylinder, the flow is highly dependant on the flow regime. A similar numerical setup at several higher Reynolds numbers could provide a more definitive answer to this question.

Furthermore, it was proposed earlier on that the transition-value of $\alpha = 3.0$ at Reynolds number 200 lowers when the Reynolds number is increased. The rate of this trend is unknown and it would be interesting to investigate this behaviour as the flow becomes turbulent.

Appendices

In general, the Finite Element Method (FEM) can be considered as a tool to obtain a numerical solution for boundary-value problems, which is in this case the Navier-Stokes equations. The FEM is characterised by the following two steps:

1. Deriving a so-called weak formulation from the original partial differential equations.
2. Discretise the geometry into "finite elements".

To explain FEM, a very simplistic example is used throughout this chapter. Consider a spatial domain $\Omega \subset \mathbb{R}^3$ with boundary Γ . Within this domain, we want to solve the Laplace problem for u , for a given functional $f : \Omega \rightarrow \mathbb{R}$:

$$\begin{aligned} \text{Find } u \text{ such that:} \\ -\Delta u = f \text{ on } \Omega \text{ with given boundary conditions.} \end{aligned} \quad (38)$$

The form above is the so-called strong, or classical, differential formulation of the problem, opposed to the weak, or variational, formulation which is used in the FEM. This is covered in the next section.

A.1 VARIATIONAL FORM

To obtain the variational formulation of the problem, two classes of functions need to be defined. First, consider a collection of all trial solutions, u , which satisfy the boundary condition. The second collection contains weighting functions, w . A requirement for u and w is that their spacial derivative is square-integrable within the domain, in other words:

$$\int_{\Omega} \nabla u \cdot \nabla u \, d\Omega < \infty \text{ and } \int_{\Omega} \nabla w \cdot \nabla w \, d\Omega < \infty. \quad (39)$$

To obtain the variational form of the example problem, the trial solution is substituted into (38) and both sides are multiplied by the weighting function. Next, the whole equation is multiplied by the weighting function. This results into the following problem:

$$\begin{aligned} \text{Find } u \text{ such that } \forall w \text{ in :} \\ -\int_{\Omega} w \cdot \Delta u \, d\Omega = \int_{\Omega} w \cdot f \, d\Omega. \end{aligned} \quad (40)$$

To make the computation as simple as possible, the second (or higher) derivatives are eliminated from the equation, which resides in the Δ -operator in this case. Using integration by parts, equation (40) can be rewritten:

$$\int_{\Omega} \nabla w \cdot \nabla u \, d\Omega - \int_{\Omega} \nabla(w \cdot \nabla u) \, d\Omega = \int_{\Omega} w \cdot f \, d\Omega. \quad (41)$$

Using Gauss' divergence theorem, the second term with an integral over the domain can be reduced to a line-integral over the boundary, which yields:

$$\int_{\Omega} \nabla w \cdot \nabla u \, d\Omega - \int_{\Gamma} (w \cdot \nabla u) \cdot \underline{n} \, d\Gamma = \int_{\Omega} w \cdot f \, d\Omega. \quad (42)$$

It can be proven that this variational form is equivalent to the original strong form. The variational formulation is written as:

$$(\nabla w, \nabla u)_{\omega} - (w, \nabla u)_{\Gamma} = (w, f)_{\Omega}. \quad (43)$$

Here, $(\cdot, \cdot)_{\Omega}$ denotes a symmetric, bilinear form:

$$(\mathbf{u}, \mathbf{v})_{\Omega} = \int_{\Omega} (\mathbf{u} \cdot \mathbf{v}) \, d\Omega. \quad (44)$$

Some properties regarding the commutativity and distributivity:

$$(\mathbf{u}, \mathbf{v})_{\Omega} = (\mathbf{v}, \mathbf{u})_{\Omega}$$

$$(\mathbf{u}, \mathbf{v} + \mathbf{w})_{\Omega} = (\mathbf{u}, \mathbf{v})_{\Omega} + (\mathbf{u}, \mathbf{w})_{\omega} \quad (45)$$

$$(c\mathbf{u}, \mathbf{v})_{\Omega} = (\mathbf{u}, c\mathbf{v})_{\Omega} = c \cdot (\mathbf{u}, \mathbf{v})_{\Omega} \text{ for a scalar } c \in \mathbb{R}.$$

INTEGRATION BY PARTS APPLIED TO TERMS OF THE NAVIER-STOKES EQUATIONS

B.1 INTEGRATION BY PARTS AND GAUSS'S DIVERGENCE THEOREM

Integration by parts is done by using the product rule for derivatives and integrating the result over a domain Ω :

$$\int_{\Omega} \nabla \cdot (f \underline{g}) \, d\Omega = \int_{\Omega} \nabla f \cdot \underline{g} \, d\Omega + \int_{\Omega} f(\nabla \cdot \underline{g}) \, d\Omega. \quad (46)$$

Equation (46) can easily be rewritten to

$$\int_{\Omega} f(\nabla \cdot \underline{g}) \, d\Omega = \int_{\Omega} \nabla \cdot (f \underline{g}) \, d\Omega - \int_{\Omega} \nabla f \cdot \underline{g} \, d\Omega \quad (47)$$

and

$$\int_{\Omega} \nabla f \cdot \underline{g} \, d\Omega = \int_{\Omega} \nabla \cdot (f \underline{g}) \, d\Omega - \int_{\Omega} f(\nabla \cdot \underline{g}) \, d\Omega. \quad (48)$$

Next, Gauss's divergence theorem,

$$\int_{\Omega} \nabla \cdot \underline{h} \, d\Omega = \int_{\Gamma} (\underline{h} \cdot \underline{n}) \, d\Gamma, \quad (49)$$

with Γ representing the boundary of the domain Ω and \underline{n} the normal unit vector on the boundary, can be applied to the second term of equations (47) and (48), resulting in:

$$\int_{\Omega} f(\nabla \cdot \underline{g}) \, d\Omega = \int_{\Gamma} (f \underline{g}) \cdot \underline{n} \, d\Gamma - \int_{\Omega} \nabla f \cdot \underline{g} \, d\Omega \quad (50)$$

and

$$\int_{\Omega} \nabla f \cdot \underline{g} \, d\Omega = \int_{\Gamma} (f \underline{g}) \cdot \underline{n} \, d\Gamma - \int_{\Omega} f(\nabla \cdot \underline{g}) \, d\Omega. \quad (51)$$

B.2 APPLIED TO THE DIFFUSION TERM

The diffusion term in the incompressible Navier-Stokes equations (multiplied by a weighting function w and integrated over a domain Ω),

$$-\int_{\Omega} w \nu \Delta \underline{u} \, d\Omega = -\int_{\Omega} w \nu (\nabla \cdot \nabla \underline{u}) \, d\Omega, \quad (52)$$

contains a second derivative in \underline{u} . To simplify the equation, integration by parts can be used to eliminate the second derivative out of this term. Using (50), the diffusion term reduces to:

$$-\int_{\Omega} w \nu (\nabla \cdot \nabla \underline{u}) \, d\Omega = -\int_{\Gamma} (w \nu \nabla \underline{u}) \cdot \underline{n} \, d\Gamma + \int_{\Omega} \nabla w \cdot (\nu \nabla \underline{u}) \, d\Omega. \quad (53)$$

When assuming that there is no flow over the boundary, i.e. $\underline{u} = 0$ on Γ , $\nabla \underline{u}$ reduces to zero, which leaves

$$-\int_{\Omega} w \nu (\nabla \cdot \nabla \underline{u}) \, d\Omega = \int_{\Omega} \nabla w \cdot (\nu \nabla \underline{u}) \, d\Omega, \quad (54)$$

or

$$-(w, \nu \Delta \underline{u})_{\Omega} = (\nabla w, \nu \nabla \underline{u})_{\Omega}. \quad (55)$$

B.3 APPLIED TO THE PRESSURE TERM

To get rid of the gradient of the pressure in the incompressible Navier-Stokes equations (multiplied by a weighting function w and integrated over a domain Ω),

$$\int_{\Omega} w \nabla p \, d\Omega \quad (56)$$

integration by parts is applied using (51). This results in

$$\int_{\Omega} w \nabla p \, d\Omega = \int_{\Gamma} (w p) \cdot \underline{n} \, d\Gamma - \int_{\Omega} (\nabla \cdot w) p \, d\Omega \quad (57)$$

When assuming that there is a constant relative pressure at the boundary, i.e. $p = 0$ on Γ , equation (57) reduces to:

$$\int_{\Omega} w \nabla p \, d\Omega = -\int_{\Omega} (\nabla \cdot w) p \, d\Omega \quad (58)$$

or

$$(w, \nabla p)_\Omega = -(\nabla \cdot w, p)_\Omega. \quad (59)$$

MESH OPTIMISATION

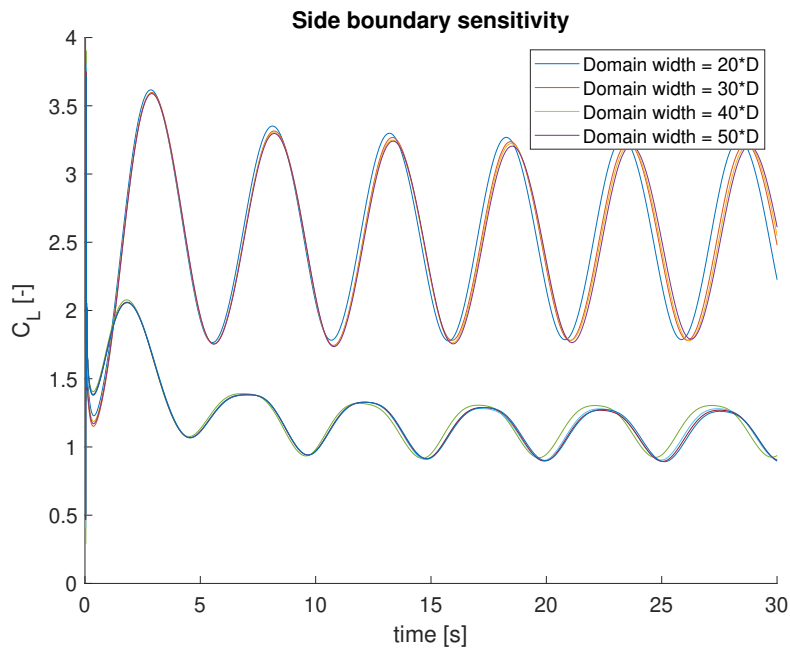


Figure 39: Lift and drag coefficients are plotted against the time for several meshes with varying domain widths.

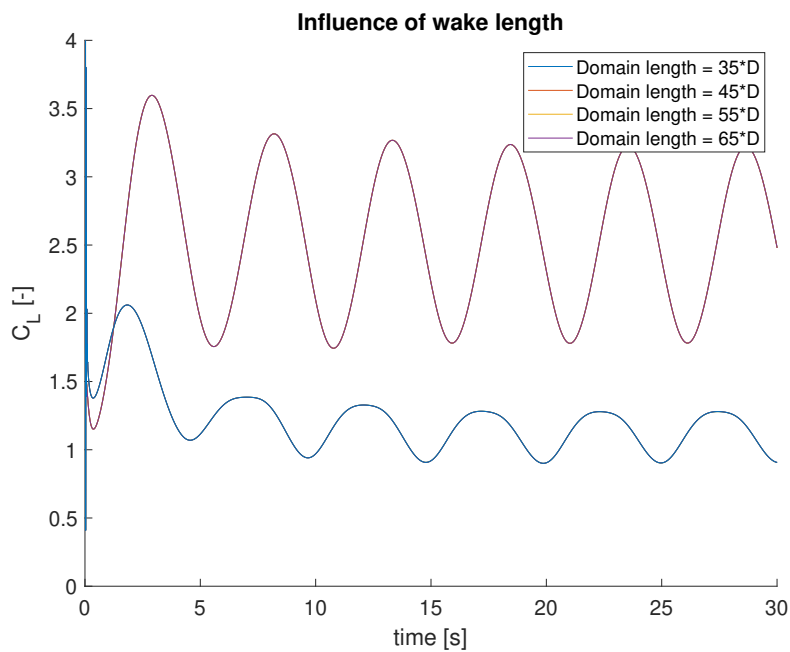


Figure 40: Lift and drag coefficients are plotted against the time for several meshes with varying wake lengths.

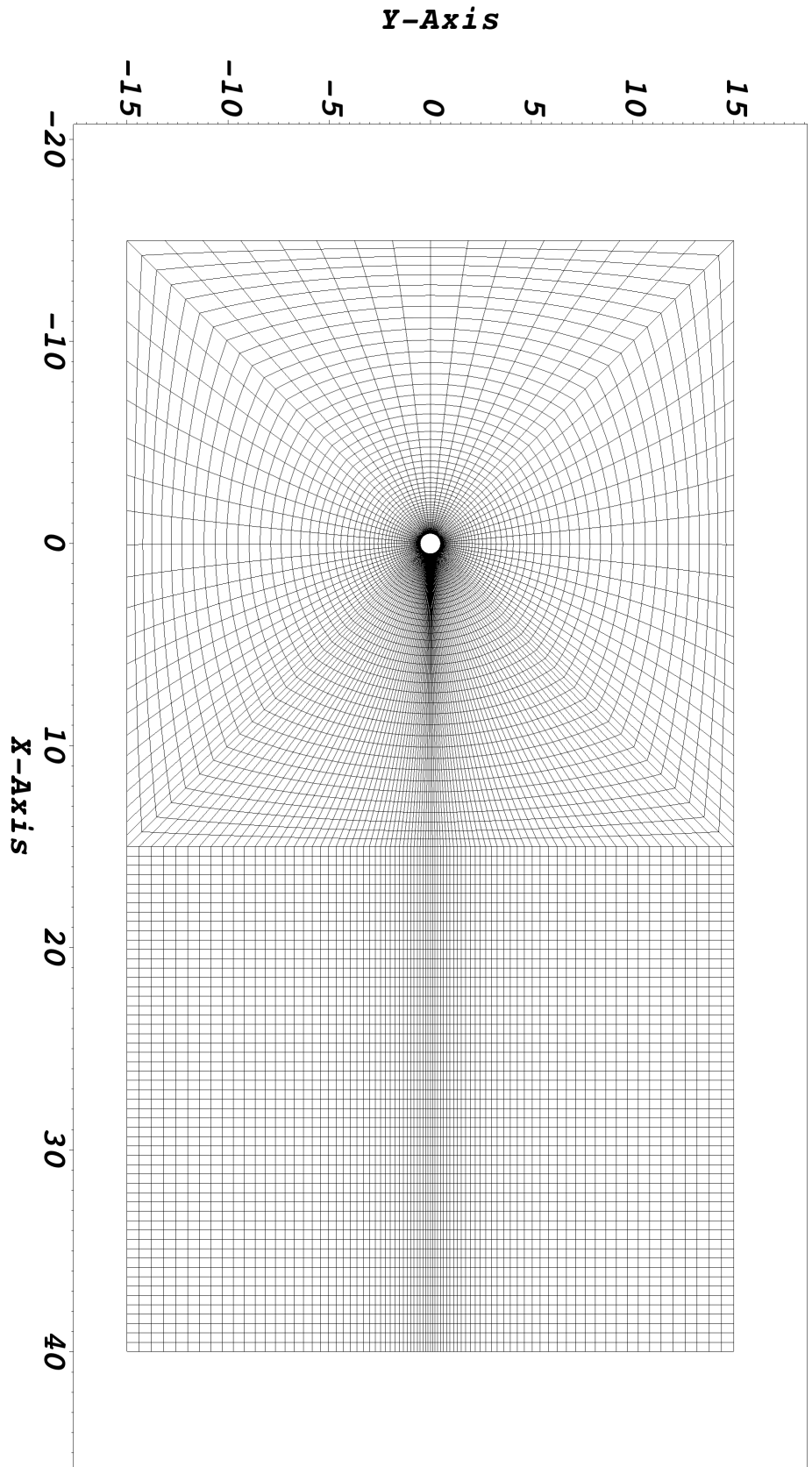


Figure 41: Two-dimensional mesh.

D

LIFT AND DRAG PLOTS

D.1 REYNOLDS NUMBER 50, 2D

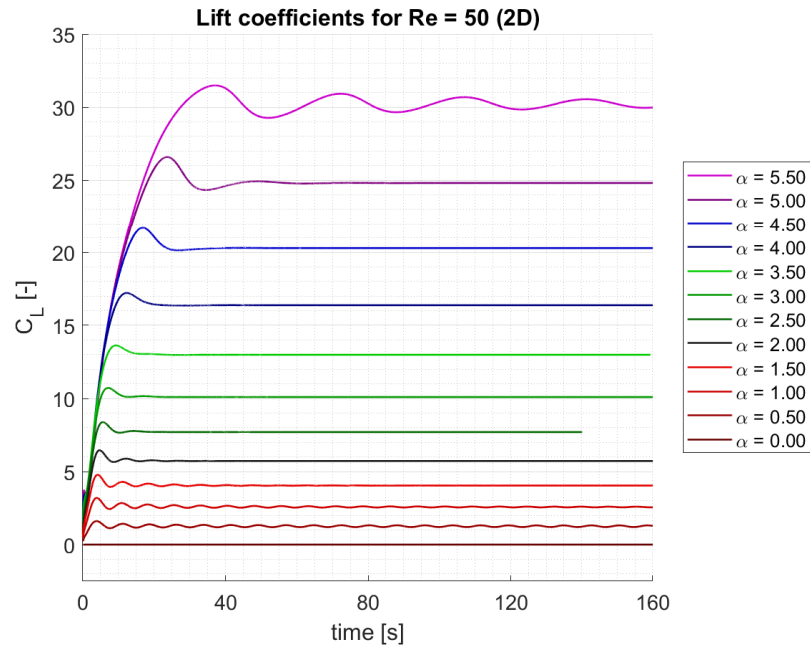


Figure 42: Lift coefficient for Re = 50 for the 2D simulation for various spin rates.

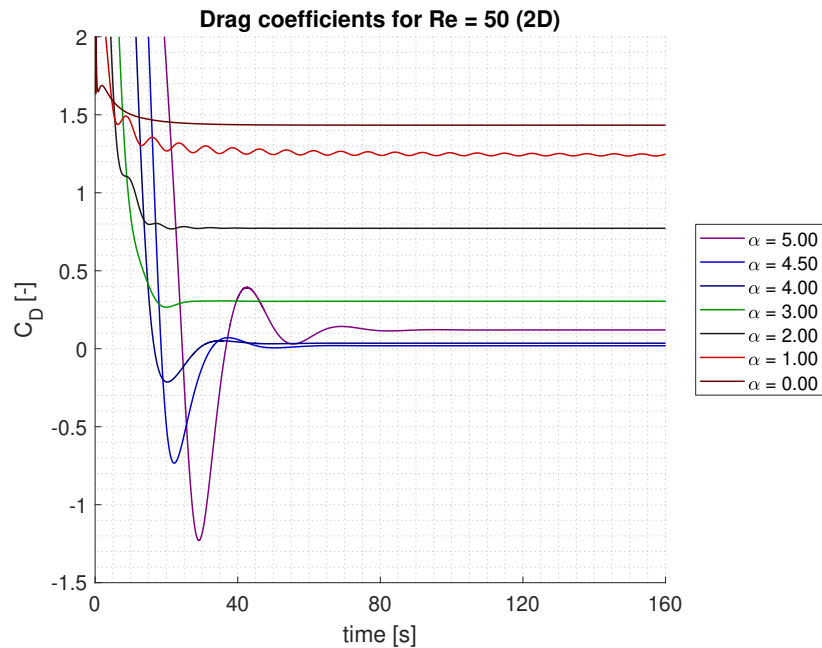


Figure 43: Drag coefficient for Re = 50 for the 2D simulation for various spin rates.

D.2 REYNOLDS NUMBER 100, 2D

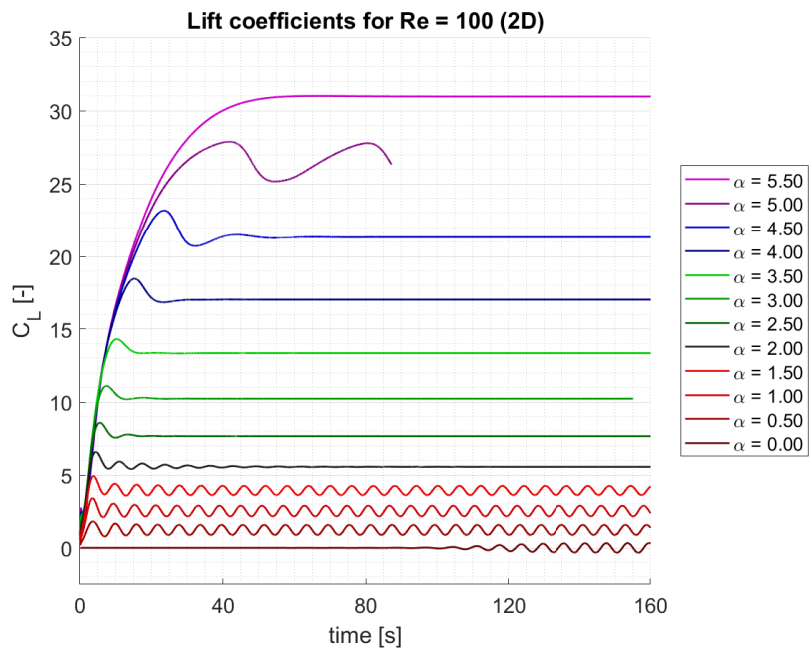


Figure 44: Lift coefficient for Re = 100 for the 2D simulation for various spin rates.

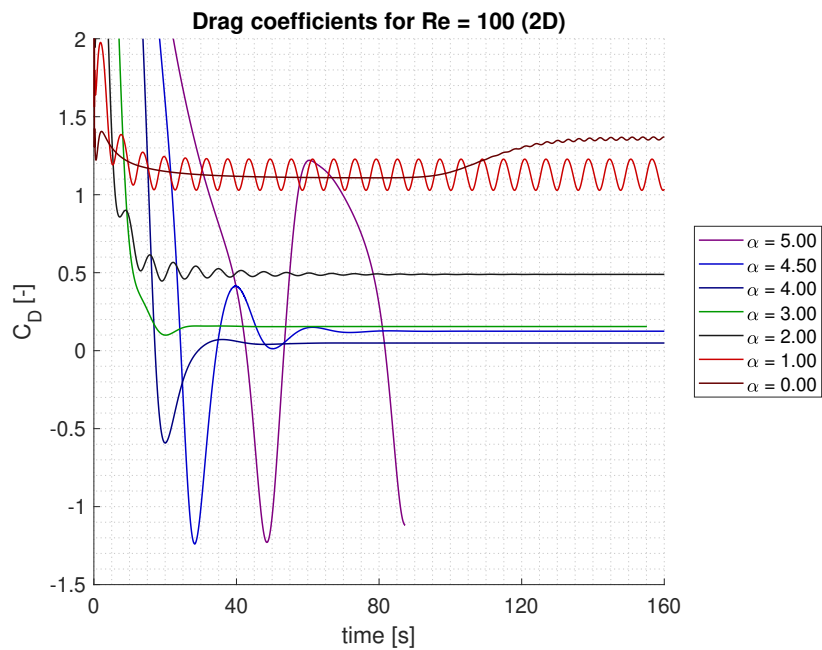


Figure 45: Drag coefficient for Re = 100 for the 2D simulation for various spin rates.

D.3 REYNOLDS NUMBER 200, 2D

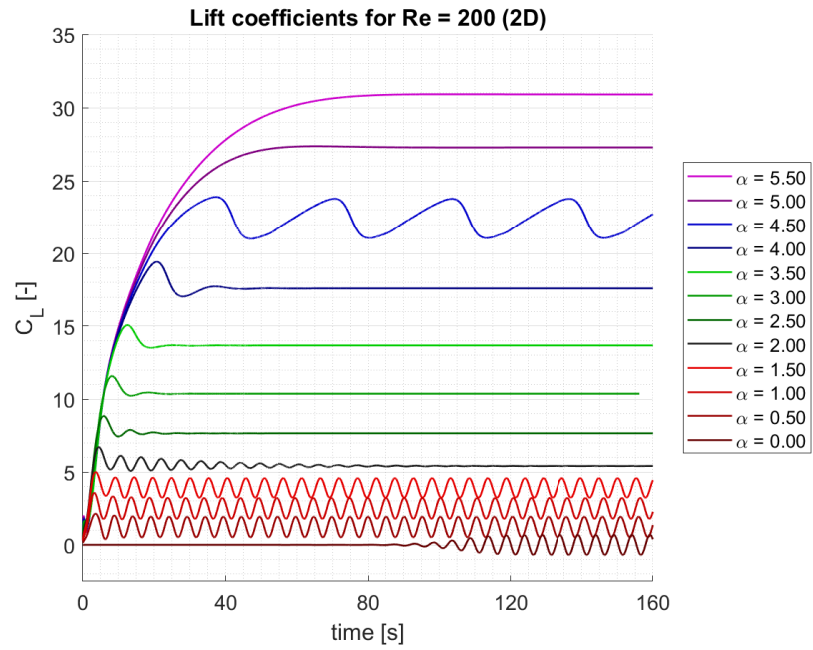


Figure 46: Lift coefficient for $Re = 200$ for the 2D simulation for various spin rates.

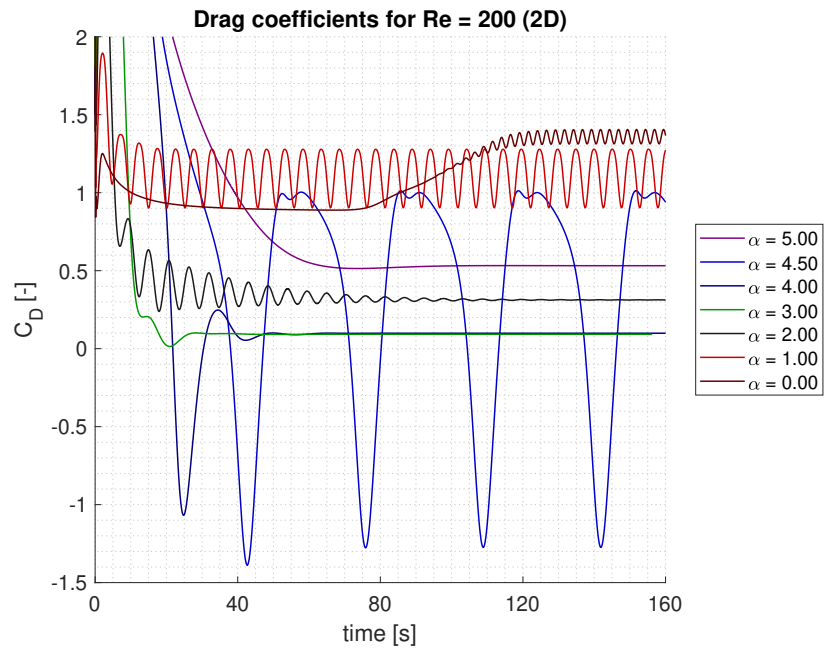


Figure 47: Drag coefficient for $Re = 200$ for the 2D simulation for various spin rates.

D.4 REYNOLDS NUMBER 200, 3D

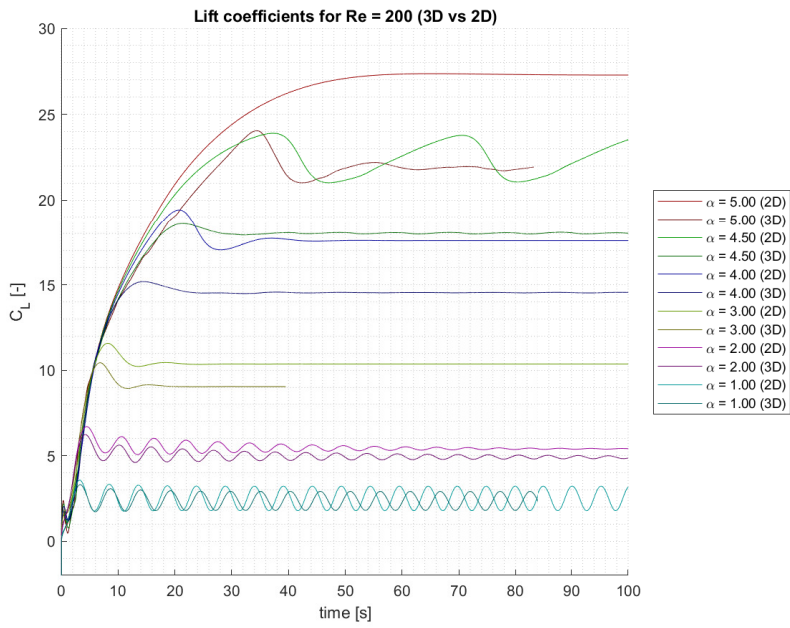


Figure 48: Lift coefficient for $Re = 200$ for the 2D and 3D simulation for various spin rates.

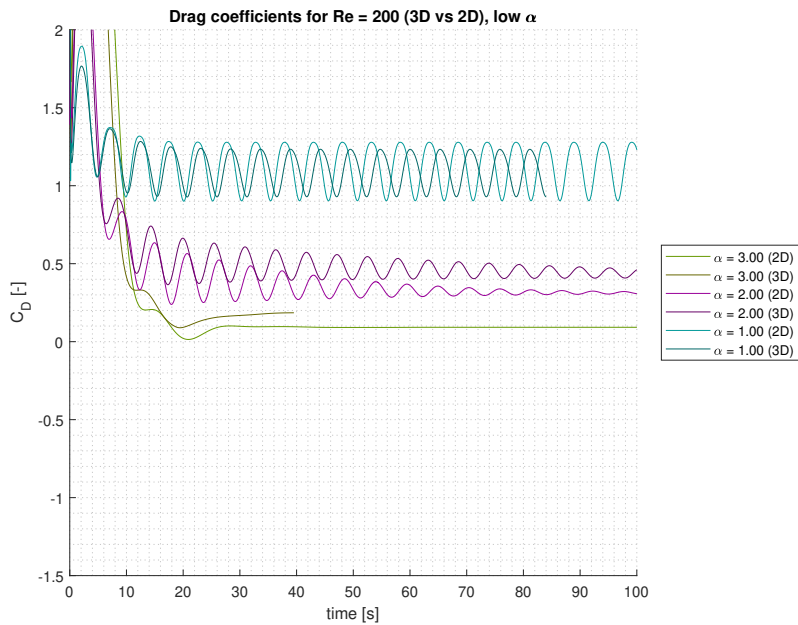


Figure 49: Drag coefficient for $Re = 200$ for the 2D and 3D simulation for low spin rates.

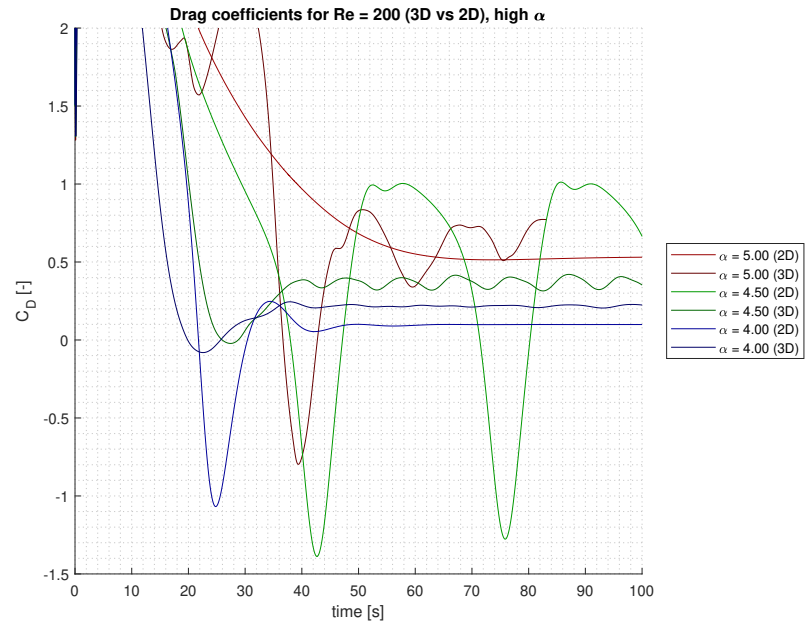


Figure 50: Drag coefficient for $Re = 200$ for the 2D and 3D simulation for high spin rates.

D.5 REYNOLDS NUMBER 300, 2D

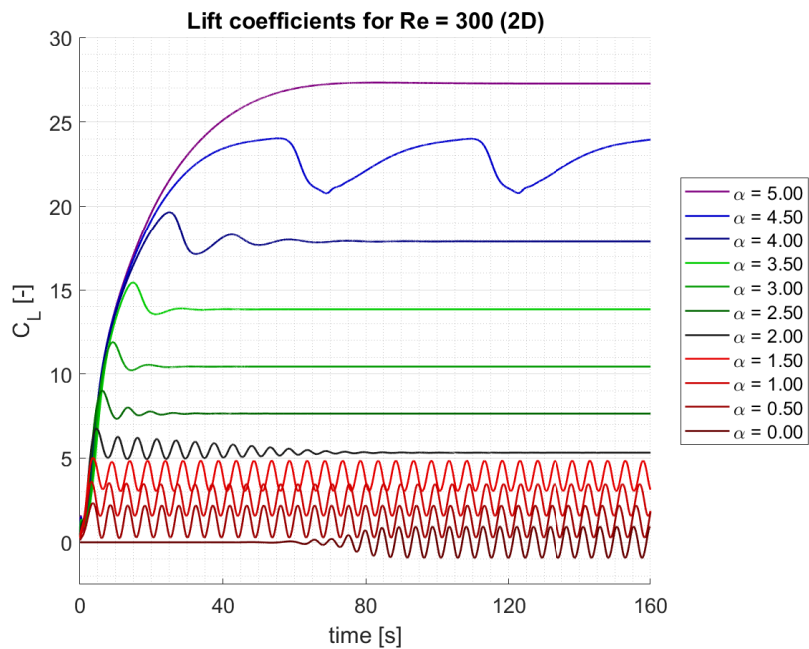


Figure 51: Lift coefficient for $Re = 300$ for the 2D simulation for various spin rates.

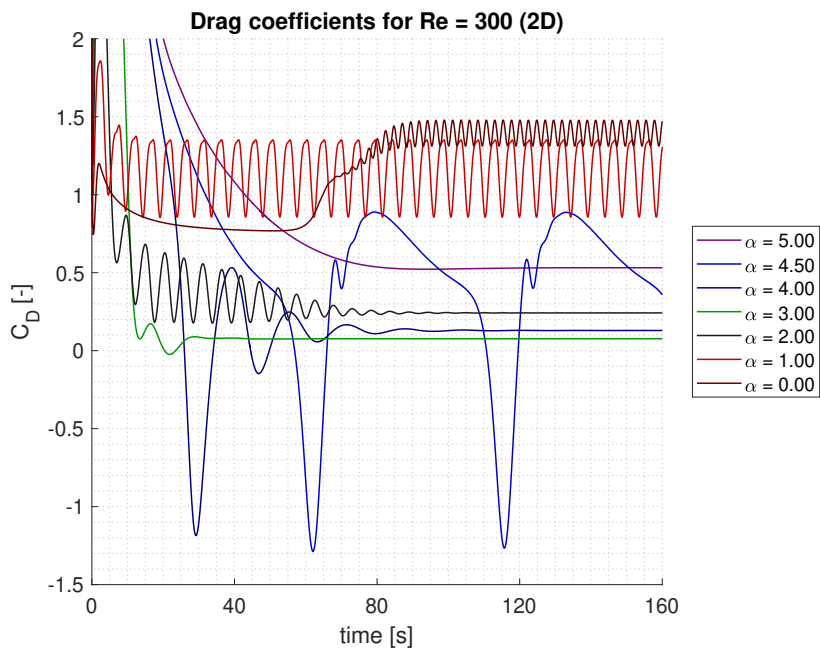


Figure 52: Drag coefficient for $Re = 300$ for the 2D simulation for various spin rates.

D.6 REYNOLDS NUMBER 400, 2D

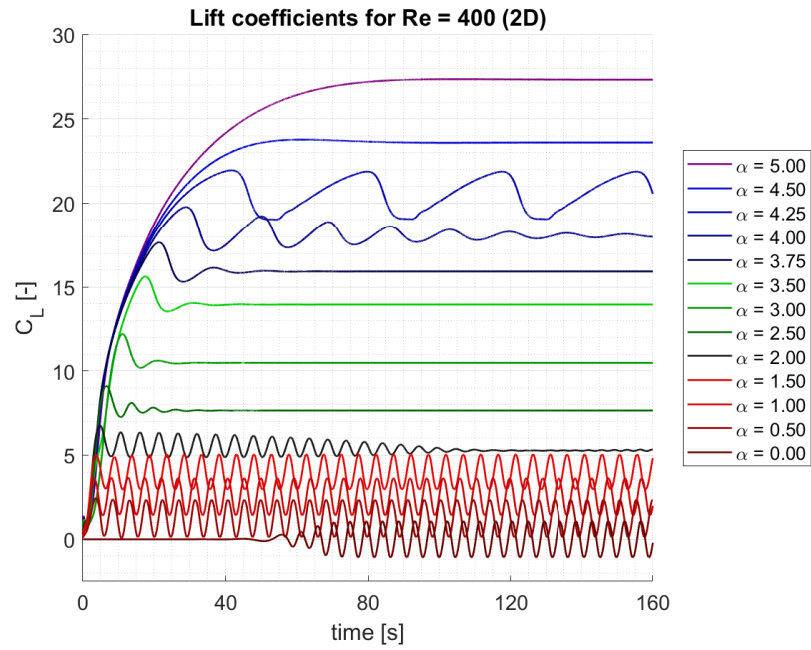


Figure 53: Lift coefficient for Re = 400 for the 2D simulation for various spin rates.

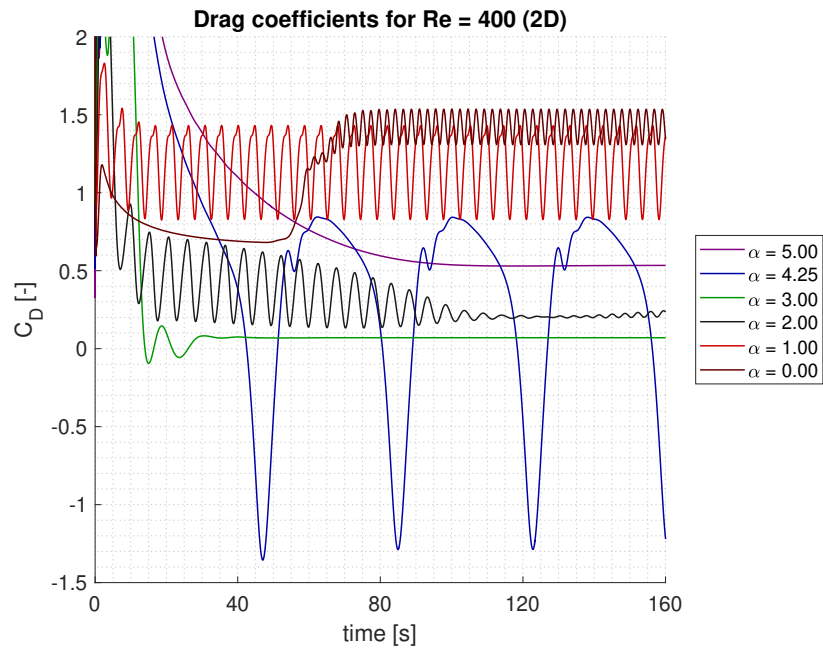


Figure 54: Drag coefficient for Re = 400 for the 2D simulation for various spin rates.

D.7 MEAN LIFT AND DRAG, 2D

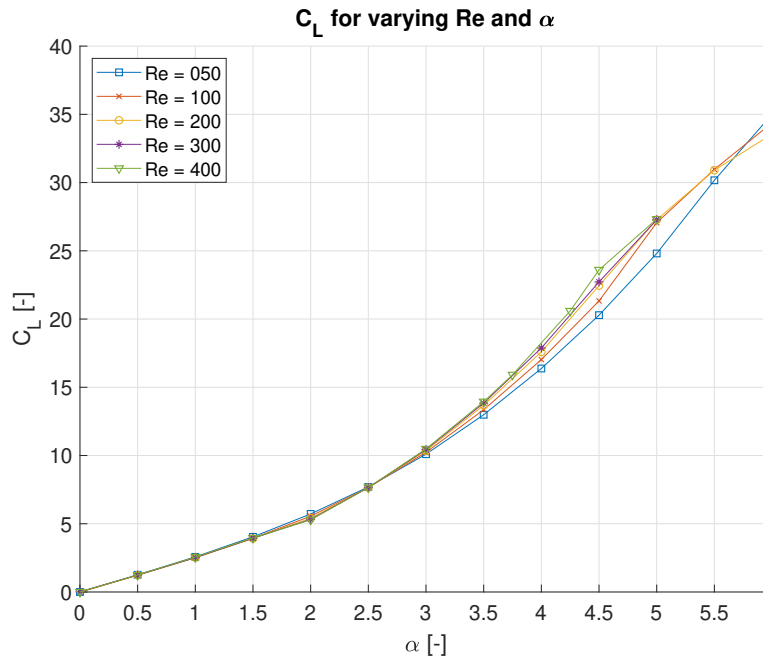


Figure 55: Mean lift coefficient for several Reynolds numbers plotted against the spin rate.

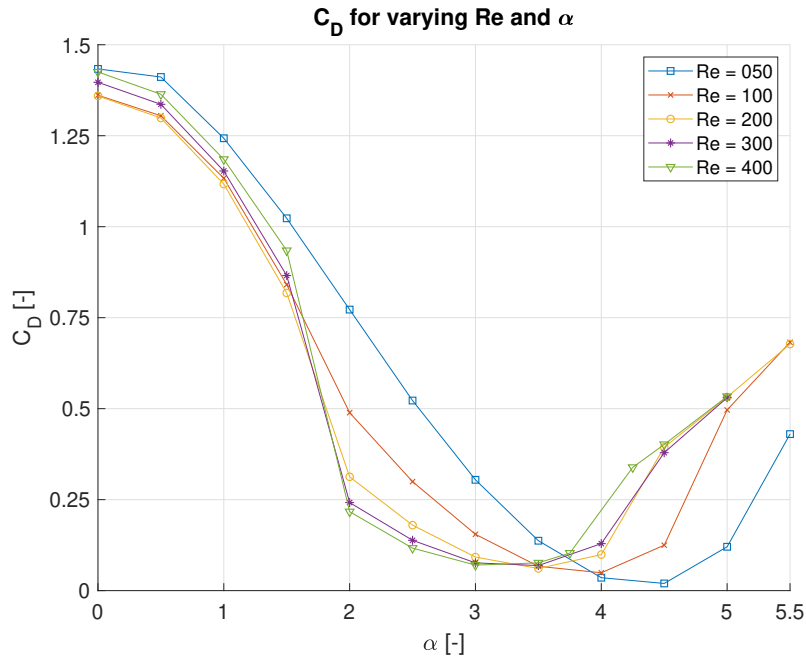


Figure 56: Mean Drag coefficient for several Reynolds numbers plotted against the spin rate.

D.8 MEAN LIFT AND DRAG, 2D AND 3D

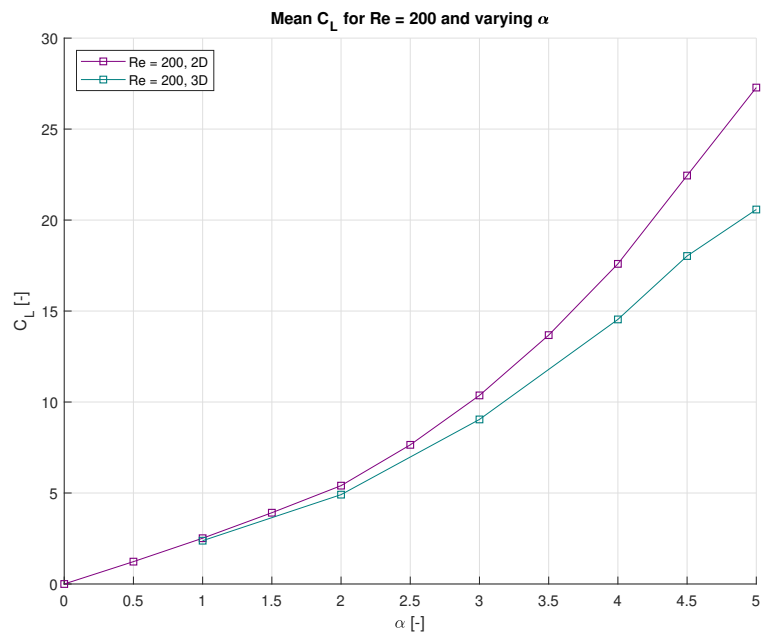


Figure 57: Mean lift coefficient for several Reynolds numbers plotted against the spin rate.

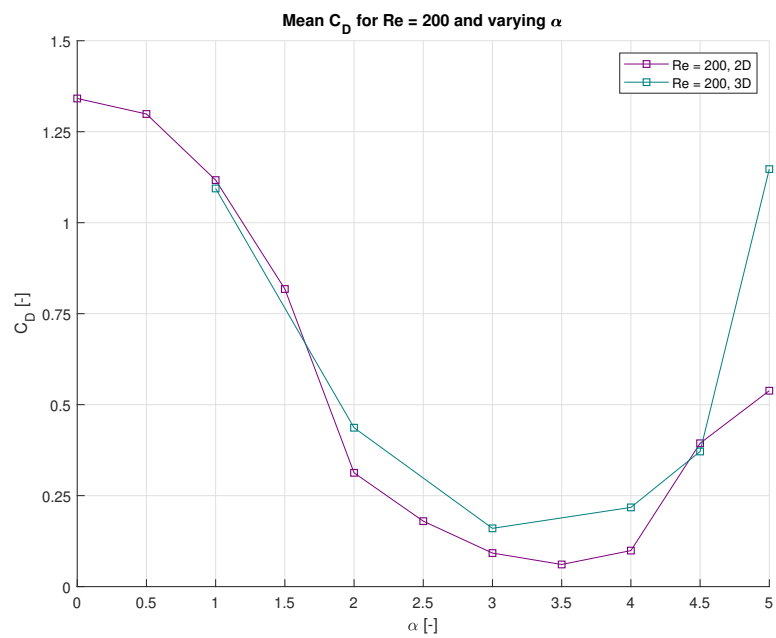


Figure 58: Mean Drag coefficient for several Reynolds numbers plotted against the spin rate.

D.9 AERODYNAMIC EFFICIENCY AND TORQUE

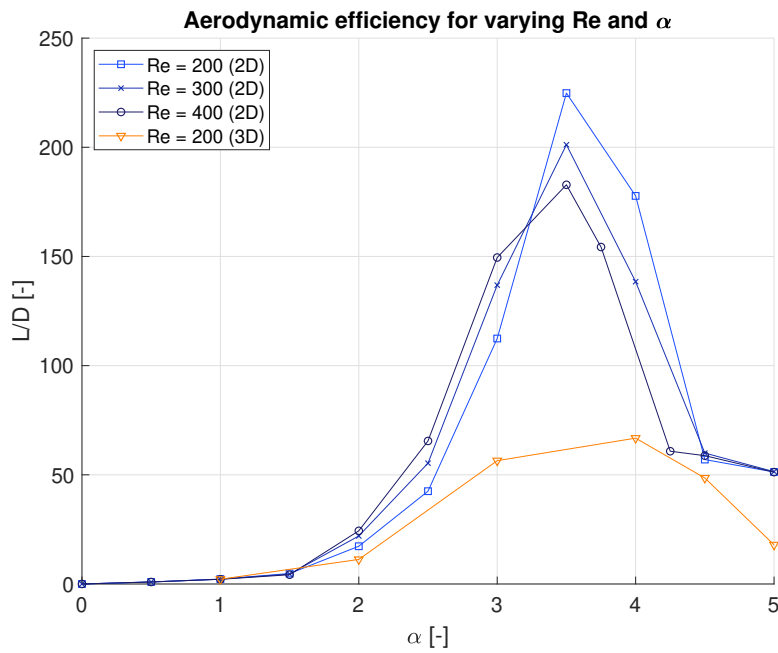


Figure 59: Aerodynamic efficiency for Reynolds number 200 plotted against the spin rate.

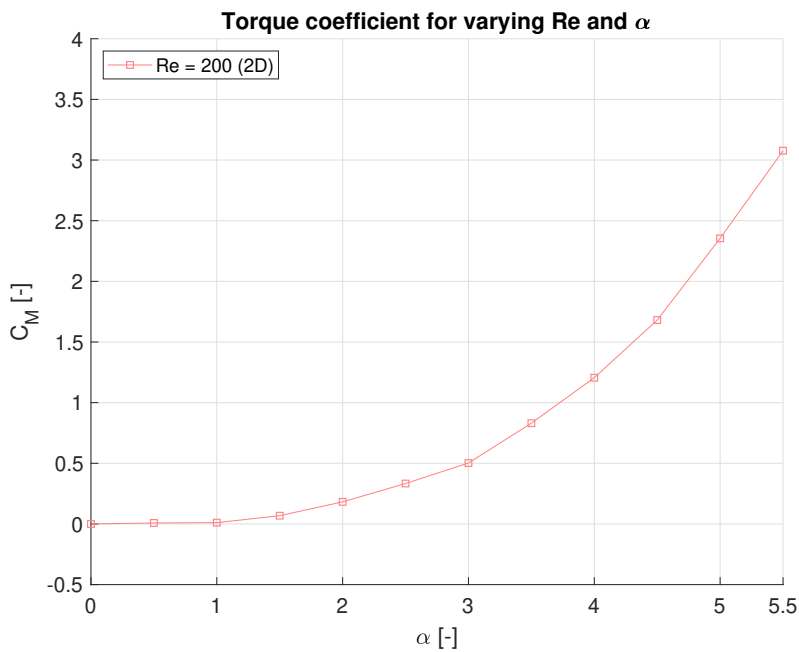


Figure 60: Torque coefficient for Reynolds number 200 plotted against the spin rate.

ADDITIONAL VISUALISATIONS IN 2D

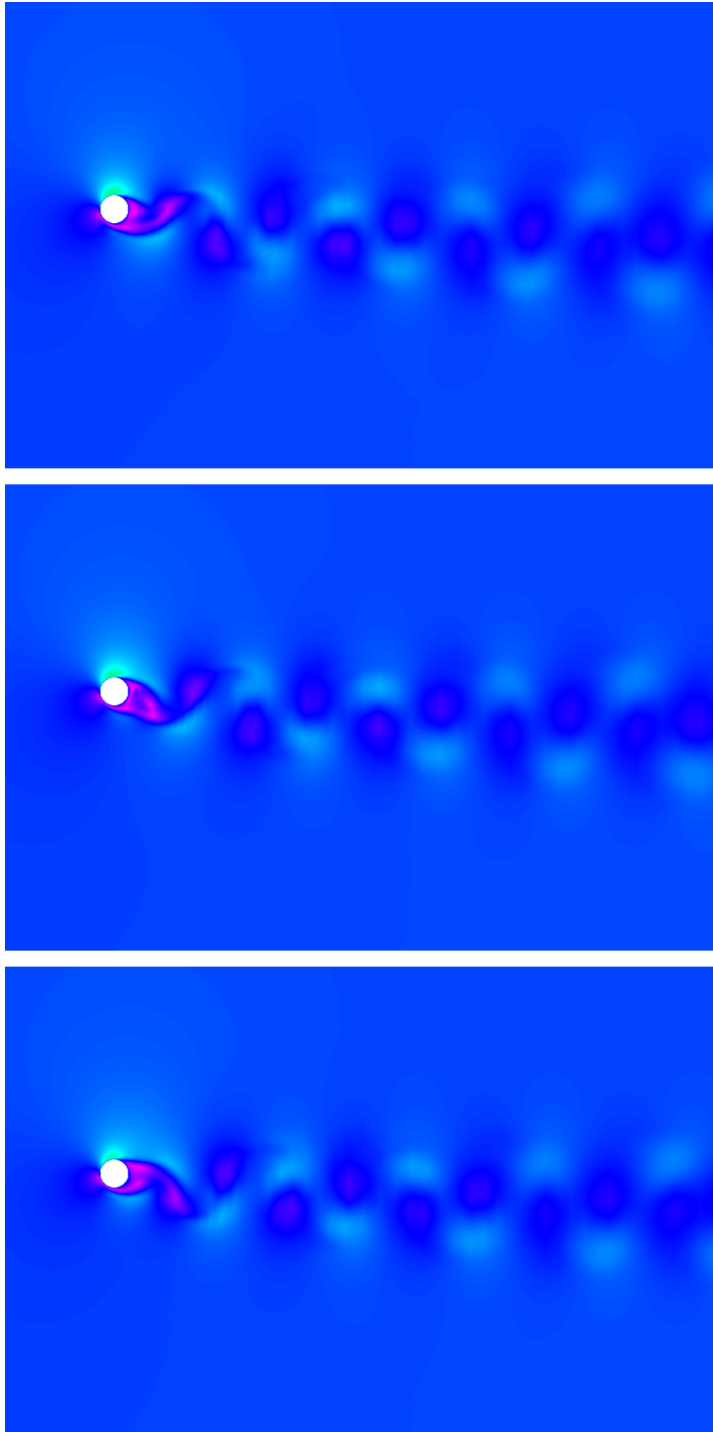


Figure 61: Time evolution at $\alpha = 1.0$ at respectively $t = 100.0s$, $t = 101.5s$ and $t = 103.0s$ from top to bottom.

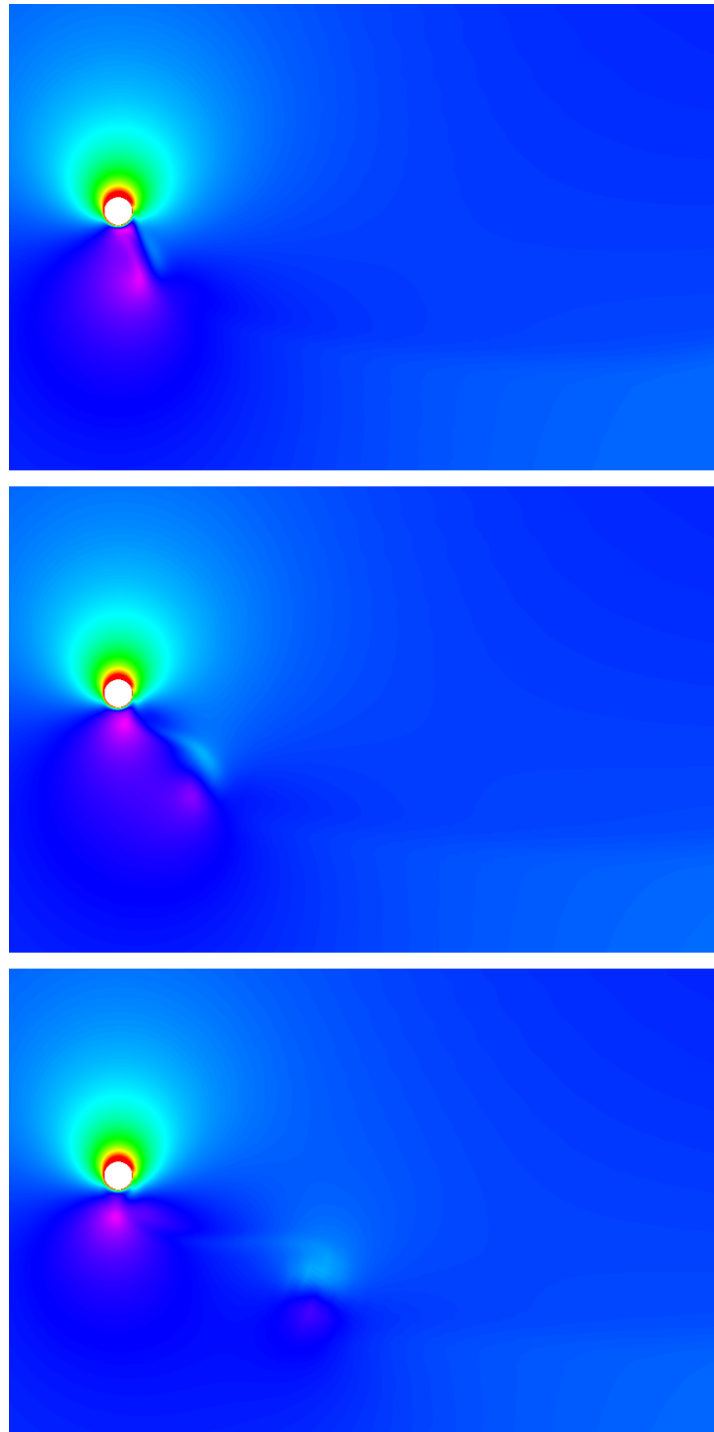
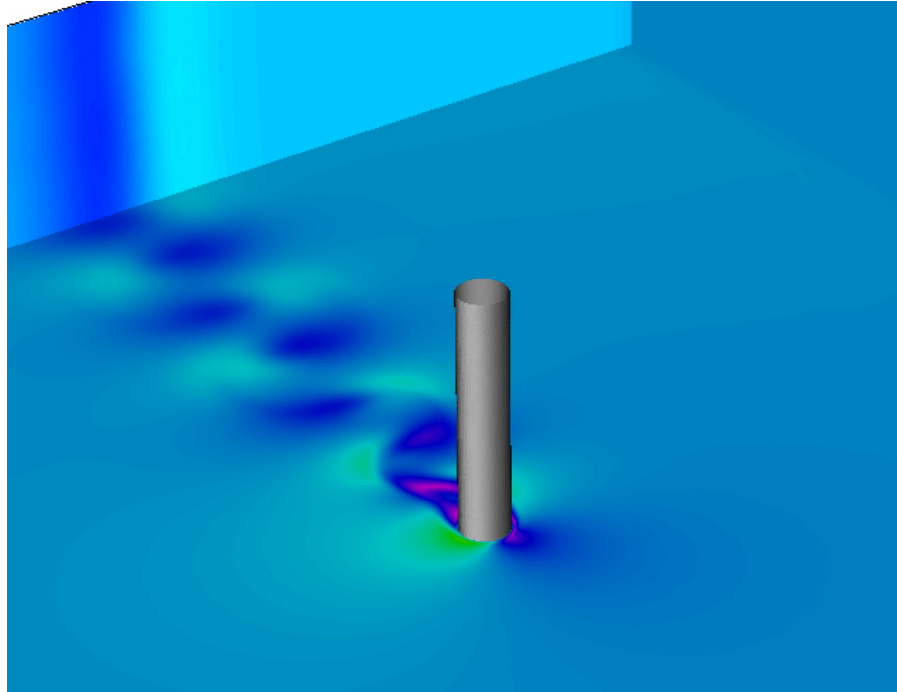
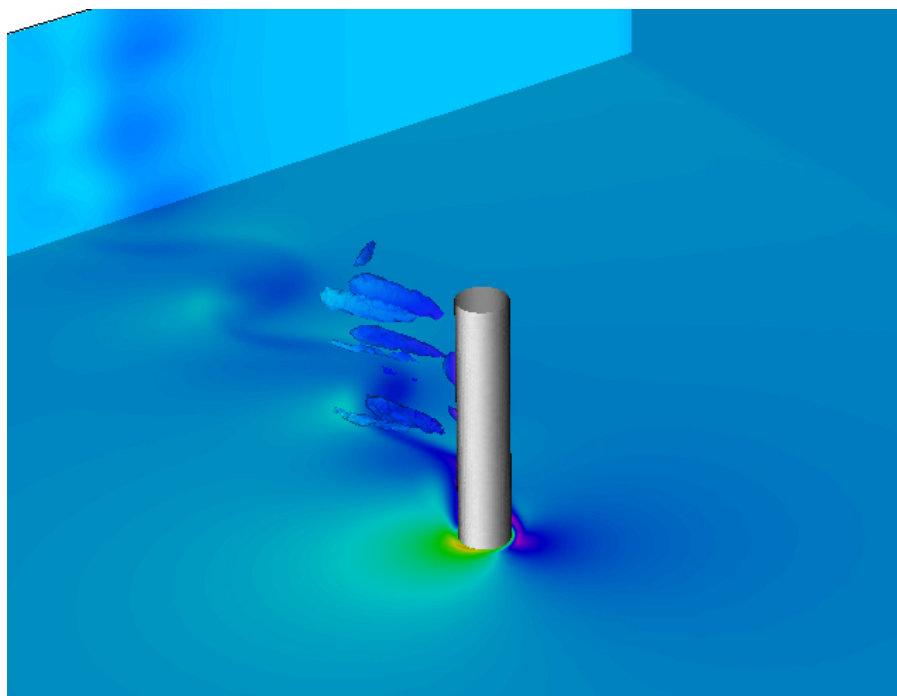


Figure 62: Time evolution at $\alpha = 4.5$ at respectively $t = 140.6s$, $t = 144.1s$ and $t = 149.1s$ from top to bottom.

F

ADDITIONAL VISUALISATIONS IN 3D

F.1 REYNOLDS NUMBER 200, SPIN RATES UP TO 4.0

Figure 63: Visualisation of the flow at $\alpha = 1.0$.Figure 64: Visualisation of the flow at $\alpha = 2.0$.

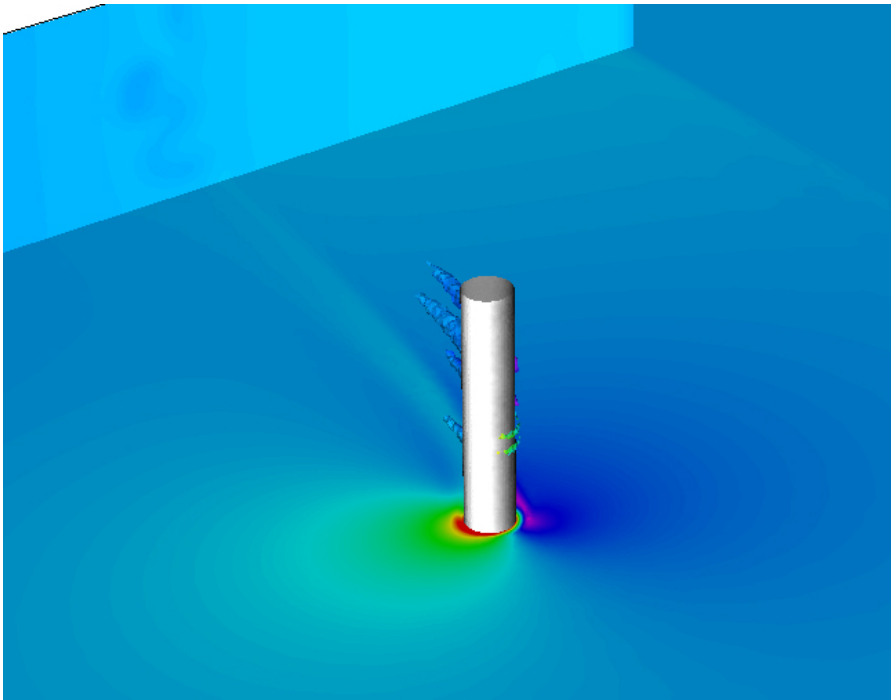


Figure 65: Visualisation of the flow at $\alpha = 3.0$.

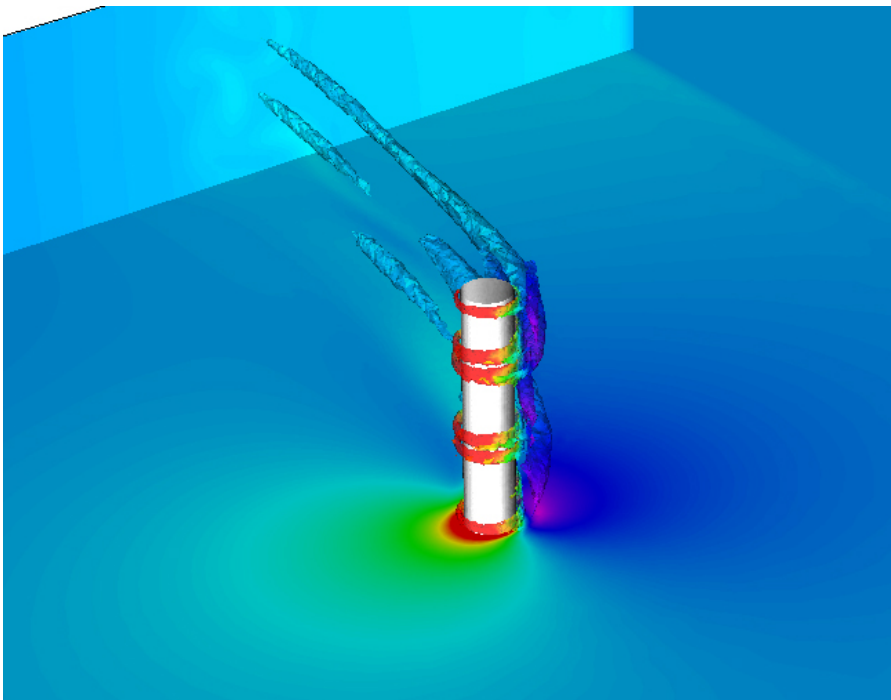


Figure 66: Visualisation of the flow at $\alpha = 4.0$.

F.2 REYNOLDS NUMBER 200, SPIN RATES ABOVE 4.0

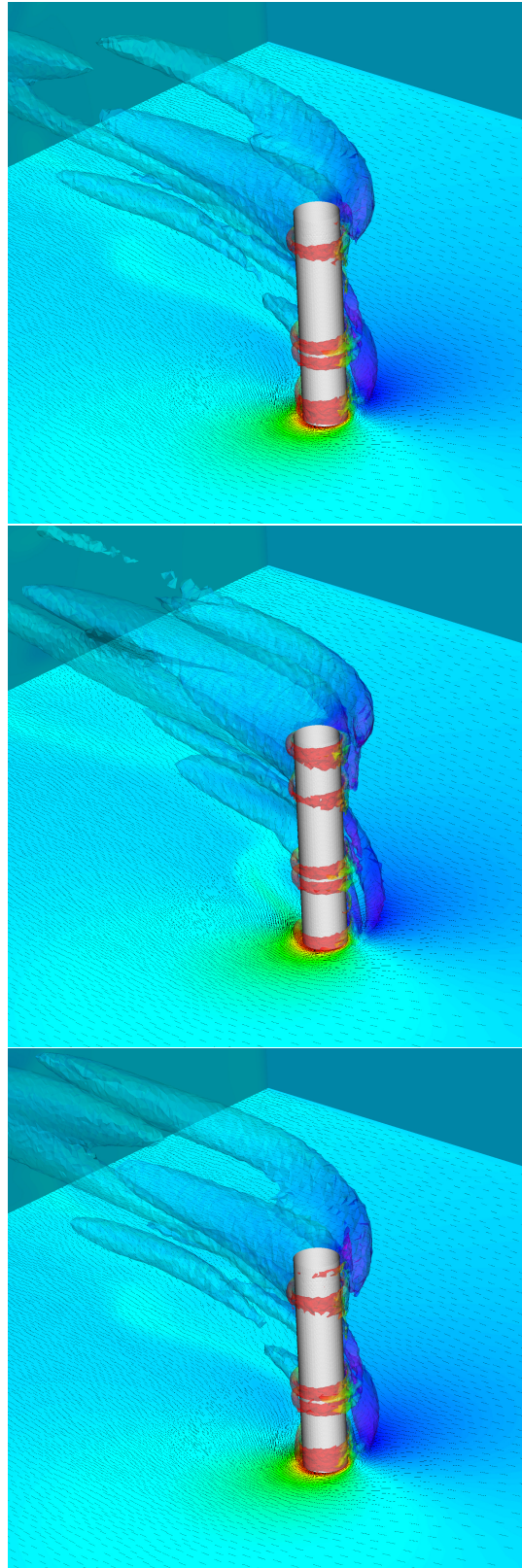


Figure 67: Time evolution at $\alpha = 4.5$ at respectively $t = 50.0s$, $t = 55.0s$ and $t = 60.0s$ from top to bottom.

BIBLIOGRAPHY

- [1] Y. Bazilevs and I. Akkerman. "Large eddy simulation of turbulent Taylor–Couette flow using isogeometric analysis and the residual-based variational multiscale method." In: *Journal of Computational Physics* 229.9 (2010), pp. 3402–3414. DOI: [10.1016/j.jcp.2010.01.008](https://doi.org/10.1016/j.jcp.2010.01.008).
- [2] M. Braza, P. Chassaing, and H. Ha Minh. "Numerical study and physical analysis of the pressure and velocity fields in the near wake of a circular cylinder." In: *Journal of Fluid Mechanics* 165 (1986), 79–130. DOI: [10.1017/S0022112086003014](https://doi.org/10.1017/S0022112086003014).
- [3] M. Breuer. "A challenging test case for large eddy simulation: high Reynolds number circular cylinder flow." In: *International Journal of Heat and Fluid Flow* 21.5 (2000), pp. 648–654. DOI: [10.1016/S0142-727X\(00\)00056-4](https://doi.org/10.1016/S0142-727X(00)00056-4).
- [4] P. Catalano, M. Wang, G. Iaccarino, and P. Moin. "Numerical simulation of the flow around a circular cylinder at high Reynolds numbers." In: *International Journal of Heat and Fluid Flow* 24.4 (2003), pp. 463–469. DOI: [10.1016/S0142-727X\(03\)00061-4](https://doi.org/10.1016/S0142-727X(03)00061-4).
- [5] J. Chung and G. M. Hulbert. "A Time Integration Algorithm for Structural Dynamics With Improved Numerical Dissipation: The Generalized-Alpha Method." In: *Journal of Applied Mechanics* 60.2 (1993), pp. 371–375. DOI: [10.1115/1.2900803](https://doi.org/10.1115/1.2900803).
- [6] J.A. Cottrell, T.J.R. Hughes, and Y. Bazilevs. *Isogeometric Analysis*. Wiley, 2009. ISBN: 978-0-470-74873-2.
- [7] M. Coutanceau and C. Ménéard. "Influence of rotation on the near-wake development behind an impulsively started circular cylinder." In: *Journal of Fluid Mechanics* 158 (1985), 399–446. DOI: [10.1017/S0022112085002713](https://doi.org/10.1017/S0022112085002713).
- [8] S.C.R. Dennis and G. Chang. "Numerical solutions for steady flow past a circular cylinder at Reynolds numbers up to 100." In: *Journal of Fluid Mechanics* 42.3 (1970), 471–489. DOI: [10.1017/S0022112070001428](https://doi.org/10.1017/S0022112070001428).
- [9] *Enercon E-Ship 1 - A Wind-Hybrid Commercial Cargo Ship*. 4th Conference on Ship Efficiency. 2013.
- [10] S. Engelman and M. Jamnia. "Transient flow past a circular cylinder: a benchmark solution." In: *International Journal for Numerical Methods in Fluids* 11 (1990), pp. 985–1000. DOI: [10.1002/flid.1650110706](https://doi.org/10.1002/flid.1650110706).
- [11] J. Fredsoe and M.B. Sumer. *Hydrodynamics around cylindrical structures*. Vol. 26. World scientific, 2006.

- [12] T.J.R. Hughes, V.M. Calo, and G. Scovazzi. "Variational and Multiscale Methods in Turbulence." In: *Mechanics of the 21st Century*. Ed. by W. Gutkowski and T.A. Kowalewski. Springer Netherlands, 2005, pp. 153–163. ISBN: 978-1-4020-3559-3.
- [13] K.E. Jansen, C.H. Whiting, and G.M. Hulbert. "A generalized-alpha method for integrating the filtered Navier–Stokes equations with a stabilized finite element method." In: *Computer Methods in Applied Mechanics and Engineering* 190.3 (2000), pp. 305–319. DOI: [10.1016/S0045-7825\(00\)00203-6](https://doi.org/10.1016/S0045-7825(00)00203-6).
- [14] S.J. Karabelas. "Large Eddy Simulation of high-Reynolds number flow past a rotating cylinder." In: *International Journal of Heat and Fluid Flow* 31.4 (2010), pp. 518–527. DOI: [10.1016/j.ijheatfluidflow.2010.02.010](https://doi.org/10.1016/j.ijheatfluidflow.2010.02.010).
- [15] J. Kim, H. Choi, H. Park, and J. Yoo. "Inverse Magnus effect on a rotating sphere: when and why." In: *Journal of Fluid Mechanics* 754 (2014), R2. DOI: [10.1017/jfm.2014.428](https://doi.org/10.1017/jfm.2014.428).
- [16] S. Mittal. "Three-Dimensional Instabilities in Flow Past a Rotating Cylinder." In: *Journal of Applied Mechanics* 71.1 (2004), pp. 89–95. DOI: [10.1115/1.1631032](https://doi.org/10.1115/1.1631032).
- [17] S. Mittal and B. Kumar. "Flow past a rotating cylinder." In: *Journal of Fluid Mechanics* 476 (2003), 303–334. DOI: [10.1017/S0022112002002938](https://doi.org/10.1017/S0022112002002938).
- [18] "Multiscale phenomena: Green's functions, the Dirichlet to Neumann formulation, subgrid scale models, bubbles and the origins of stabilized methods." In: *Computer Methods in Applied Mechanics and Engineering* 127.1 (1995), pp. 387–401. DOI: [10.1016/0045-7825\(95\)00844-9](https://doi.org/10.1016/0045-7825(95)00844-9).
- [19] C. Norberg. "An experimental investigation of the flow around a circular cylinder: influence of aspect ratio." In: *Journal of Fluid Mechanics* 258 (1994), 287–316. DOI: [10.1017/S0022112094003332](https://doi.org/10.1017/S0022112094003332).
- [20] J. Park, K. Kwon, and H. Choi. "Numerical solutions of flow past a circular cylinder at Reynolds numbers up to 160." In: *KSME International Journal* 12 (1998), pp. 1200–1205. DOI: [10.1007/BF02942594](https://doi.org/10.1007/BF02942594).
- [21] D.R. Pearson. "The use of Flettner rotors in efficient ship design." In: *RINA, Royal Institution of Naval Architects - Influence of EEDI on Ship Design 2014* (Jan. 2014), pp. 162–169.
- [22] *Potential applications for Flettner rotors and Turbosails in tidal stream turbines*. July 2005.
- [23] L. Prandtl. "Applications of the Magnus effect to the wind propulsion of ships." In: *Die Naturwissenschaft* 367 (1925), pp. 99–108.
- [24] S. Singha and K.P. Sinhamahapatra. "Flow past a circular cylinder between parallel walls at low Reynolds numbers." In: *Ocean Engineering* 37.8 (2010), pp. 757–769. DOI: [10.1016/j.oceaneng.2010.02.012](https://doi.org/10.1016/j.oceaneng.2010.02.012).

- [25] D.J. Tritton. "Experiments on the flow past a circular cylinder at low Reynolds numbers." In: *Journal of Fluid Mechanics* 6.4 (1959), 547–567. DOI: [10.1017/S0022112059000829](https://doi.org/10.1017/S0022112059000829).